Master's thesis

NTNU
Norwegian University of Science and Technology
Department of Marine Technology

Sunghun Hong

The Effect of Damping on the Dynamic Responses of a Floating Bridge in Wind and Waves

Master's thesis in Marine Technology
Supervisor: Zhen Gao (NTNU), Yanlin Shao (DTU)
June 2019

NTNU
Norwegian University of Science and Technology

DTU

Sunghun Hong

The Effect of Damping on the Dynamic Responses of a Floating Bridge in Wind and Waves

Master's thesis in Marine Technology
Supervisor: Zhen Gao (NTNU), Yanlin Shao (DTU)
June 2019

Norwegian University of Science and Technology
Department of Marine Technology

NTNU
Norwegian University of
Science and Technology

Preface

This thesis is the final work of the Joint Nordic Master's degree program in Maritime Engineering with the specialization of Ocean Structures. This programme aims to achieve dual degrees of MSc in Marine Technology at the Norwegian University of Science and Technology (NTNU) and MSc in Maritime Engineering at the Technical University of Denmark (DTU). The thesis is written by Sunghun Hong at the Department of Marine Technology at NTNU in spring 2019. The thesis work has been conducted under supervision of Professor Zhen Gao at NTNU as a main supervisor and Associate Professor Yalin Shao at DTU as a co-supervisor.

In this paper, the cable-stayed curved floating bridge design prepared by COWI et al. is considered as a crossing method for Bjørnafjorden and the numerical model of the given bridge provided by Cheng et al. is used. The main object of the thesis is to investigate various damping effects on the global dynamic responses of the floating bridge in wind and waves. The main scope is to establish viscous damping for the heave motion, to understand the various damping effects on the dynamic response, and to analyze the global dynamic response of the given floating bridge.

Trondheim / June 11, 2019

Sunghun Hong

Acknowledgment

I would like to thank the people who helped me while working on this thesis paper. I am grateful to Professor Zhen Gao at NTNU, the main supervisor, for suggesting this interesting topic and for giving guidance and advice during the entire project. I would like to thank Associate Professor Yanlin Shao, a co-supervisor, at DTU and Dr. Xiang Xu at Statens vegvesen for their helpful comments and suggestions during meetings. I would also like to thank Zhengshun Cheng, an Associate Professor at Shanghai Jiao Tong University, for his help in SIMO-RIFLEX simulations while he was working as a postdoctoral researcher at NTNU.

I am grateful to all my family and friends who have always prayed for me in Korea. I would like to express my special gratitude to my beloved wife, Hyunju, who always trusted me, comforted me, encouraged me, and helped me complete my two-year master's degree in Norway and Denmark.

But above all, I thank God for leading our lives and giving us wisdom and strength in every way.

Abstract

The Norwegian Public Roads Administration is working on The E39 Coastal Highway Route project to reduce the travel time of 21 hours between Trondheim and Kristiansand to 11 hours by replacing seven fjord ferry connections with bridges and tunnels. The cable-stayed curved floating design has been proposed to cross Bjørnafjorden. Since the design is a long curved structure of 5 km supported by 19 pontoons without side mooring under wind and waves combined environment, the complex resonance response in different natural periods is a challenge. Damping plays an important role in reducing the resonance response in such a harsh environment. Therefore, the main purpose of this study is to investigate various damping effects on the global dynamic response of floating bridges. The 100-year wave conditions are modeled by the JONSWAP spectrum with directional function and the 100-year wind field is generated by TurbSim with Kaimal spectrum. SIMO-RIFLEX is used in numerical simulations. The heave response without the viscous effect was 0.2-0.5 m. The viscous damping for the heave motion is modeled by the KC dependent drag coefficient, and the obtained value is 23.98, which corresponds to 8.3 for the conventional drag coefficient. After the free decay test, it was found that the linearized viscous damping ratio for the heave motion is 1.49 $\%$, while the total damping is 6.81 $\%$. Since the heave motion is small, the viscous effect is not significant. As a result of analyzing the stresses of the bridges, it was found that the total bridge girder stress is mainly due to the static stress. The static stress is governed by the weak axis bending moment which is mainly induced by the bridge weight and buoyancy. Since the static effect is predominant in the given bridge design, the damping effects are not noticeable. For the horizontal motion of pontoons, a wave drift damping can be investigated for the future study. However, prior to improving damping for the dynamic effect on the bridge, it is necessary to increase the number of pontoons to reduce the bending moment about the weak axis and reduce the overall static effect.

Table of Contents

List of Tables

List of Figures

Nomenclature & Abbreviations

α	Damping coefficient proportional to mass
α	Wind profile factor
β	Damping coefficient proportional to stiffness
β_{nb}	Acceleration weight factors for u_{k+1}
$\ddot{u}$	Acceleration
Δt	Measured time in free decay test
$\dot{u}$	Velocity
$\dot{u}_r$	Relative velocity
ϵ	Random phase angle, uniformly distributed between 0 to 2π
Γ	Gamma function
γ	Non-dimensional peak shape parameter
γ_{nb}	Acceleration weight factors for $\dot{u}_{k+1}$
λ	Damping ratio
λ_i	Modal damping ratio in i'th mode
ω	Angular wave frequency
ω_i	Eigen frequency in i'th mode
ω_n	Natural frequency
ϕ_H	Phase angle between the first order wave force and the relevant transfer function

ρ	Water density
σ	Spectral width parameter
τ	Time interval
θ	Elementary wave train directions
θ	Wave direction
θ_p	Main wave direction
$\zeta(x, y, z)$	Wave elevation
ζ_a	Body oscillation amplitude
$\zeta_a(\omega, \theta)$	Wave amplitude
A	Projected area
A^∞	Added mass at infinite frequency
A_{bottom}	Bottom plate area
A_{flange}	Flange area
$B(\tau)$	Retardation function
b_i	Modal damping
B_{cr}	Critical damping
B_{pot}	Potential damping
B_{str}	Structural damping
B_{tot}	Total damping
B_{vis}	Linearized viscous damping
C	Restoring coefficient
C_d	Drag coefficient
c_i	Modal stiffness
$C_{dz,kc}$	KC dependant drag coefficient in z-axis
D	Characteristic body length
$D(\theta)$	Directional distribution function
F	Flange width

$F^{drag}(t)$	Drag force
$F^{ext}(t)$	Excitation force
h	Time step
$H(\omega, \theta)$	Transfer function
H_s	Significant wave height
i	Degree of freedom, 1 to 6
j	Degree of freedom, 1 to 6
k	Wave number
KC	Keulegan–Carpenter number
M	Mass of the pontoon
M	Number of wave directions
m_i	Modal mass
N	Number of oscillation cycle in free decay test
N	Number of wave frequencies
n	Directional spreading parameter
Q_{damp}	Quadratic damping
Q_{drag}	Quadratic drag
$S_\zeta(\omega, \theta)$	Wave spectrum with directional variation
$S_J(\omega)$	JONSWAP spectrum
T	Relative oscillation period
t	Time
T_n	Natural period
T_p	Spectral peak period
u	Displacement
U_m	Relative oscillatory velocity
U_w	Mean wind speed at height z
$U_{w,ref}$	Mean wind speed at reference height z_{ref}

W	Pontoon width
x	Axis from the south to the north
y	Axis from the east to the west
z	Axis from the water surface to upward
z	Height of mean wind speed U_w
z	Positive maximum displacements in free decay test
z_{ref}	Reference height of mean wind speed $U_{w,ref}$
B	Damping of the system
C	Stiffness of the system
DTU	Technical University of Denmark
E39	European route E39
JONSWAP	JOint North Sea WAve Project
M	Mass of the system
NPRA	Norwegian Public Road Administration
NTNU	Norwegian University of Science and Technology
RIFLEX	A program for hydrodynamic and structural analysis of slender marine structures
SIMA	A workbench which offers a complete solution for simulation and analysis of marine operations and floating systems
SIMO	A time domain simulation program for study of motions and station keeping of multibody systems
TLP	Tension Leg Platform

Chapter 1

Introduction

Background

The Norwegian Public Road Administration (NPRA) has been working on developing "The E39 Coastal Highway Route" project which was called E39 Ferry-Free project. E39 is a coastal highway connecting Trondheim and Kristiansand as presented in *Figure 1.1*. The main purpose of the project is to replace all ferry connections on the E39 highway with bridges and tunnels, reducing the total travel time of 21 hours to 11 hours. The project is also expected to be beneficial to the engineering, construction and transportation industries. Among the 10 fjords on the E39 highway, the main location of this paper is Bjørnafjorden, located between Bergen and Stavanger. The width of Bjørnafjorden is 5 km and the depth is 500 m. Due to these rough geographical conditions in fjords, it is difficult and costly to make traditional bridges. Several alternative crossing methods were proposed for crossing Bjørnafjorden including multi-span suspension bridge supported by TLP (Tension Leg Platform), submerged floating tube tunnel, end-anchored cable-stayed curved floating bridge. In this paper, the end-anchored cable-stayed curved floating bridge prepared by COWI et al. [6] is discussed.

Challenges

The proposed floating bridge is 5 km of curvilinear shape and consists of a cable-stayed high bridge part and a low floating bridge part supported by pontoons. The environmental condition in the fjord is wind and wave combined conditions. Under these environmental loads, the bridge experiences complex resonant responses because the bridge is supported by 19 floating pontoons without side mooring. Damping is important in terms of reducing the resonance response in this harsh environment.

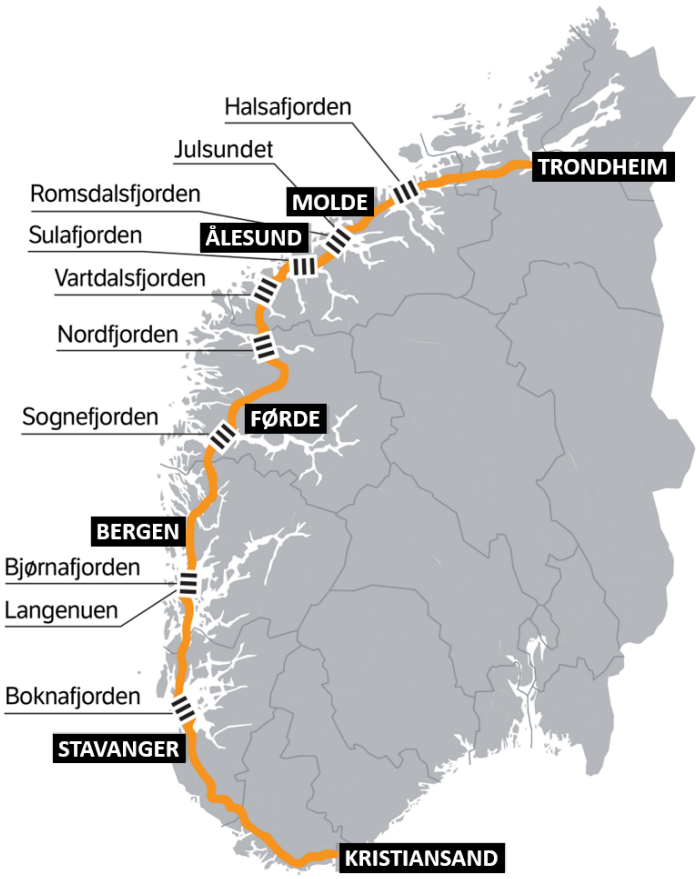

Figure 1.1: Overview of The E39 Coastal Highway Route [18].

Object

Therefore, the main object of this paper is to study how various damping factors affect the global dynamic responses of the floating bridge.

Previous Studies

Cheng et al. have prepared a numerical model of the given curved floating bridge in SIMO-RIFLEX, modeled the hydrodynamic loads and analyzed the bridge responses. In his studies, the global responses of the floating bridge under wave loads were investigated and it was found that the heave motion and the weak axis bending moment is affected by short-crested waves, while the sway motion and the strong axis bending moment are affected by the second order difference frequency wave loads.

Thesis Preparation

During the past semester, the author prepared a project paper entitled ”Dynamic Analysis of Vertical Responses of a Floating Bridge in Waves” in preparation for this paper. The author has learned about the background of the E39 project, the alternative crossing concept of the fjord, the detailed features of Bjørnafjorden and the proposed crossing concept for Bjørnafjorden. Numerical simulations were performed to understand the vertical response of the bridge in the wave conditions. It was found that the heave motion of the bridge under the local wind-generated wave responded with the eigen period of the bridge, while under the swell wave, the response of the same period as the swell period was observed. In addition, the heave response increases as the wavelength increases, while the weak axis bending moment increases as the wave height increases.

Scope

As an extension of previous research, the main scope of this paper can be summarized as follows:

- Defining reasonable environmental conditions for simulations,
- Establishing a proper viscous damping for heave motion of the floating bridge,
- Understanding the contributions of various damping sources, and
- Analyzing the global dynamic responses of the bridge including the bridge girder stress.

1.1 The E39 Coastal Highway Route

On March 25, 2011, the project "Ferry-Free Coastal Route E39" was launched at the national convention held in Stavanger. The Ministry of Transportation and Communications has commissioned NPRA to develop 1100 km long coastal route E39 connecting Trondheim and Kristiansand, *Figure 1.1*. Initially, the project was planned for 10 years, but in the recent National Transport Plan 2018-2029, the planning period is extended to 12 years [12]. The project is now named "The E39 Coastal Highway Route" and the main objective of this project is to replace the seven ferry connections to bridges or tunnels and reduce the travel time of E39 from 21 hours to 11 hours. Besides, the Norwegian government expects to have benefits on the relevant labor markets including engineering and construction [18].

1.1.1 Fjords Conditions

The geographical information of the fjords in E39 are summarized in *Table 1.1*. The width of the fjords is between 1.3 km to 27 km and the depth of the fjord is minimum 300 m. Because of these harsh environment, relevant researches have been conducted for given challenges.

Table 1.1: Width and depth of fjords crossing route E39.

	Width $[m]$	Depth $[m]$
Halsafjorden	2,000	500 - 600
Julsundet	1,600	500 - 600
Romsdalsfjorden	13,000	330
Sulafjorden	3,800	500
Vartdalsfjorden	2,100	600
Nordfjorden	1,700	300 - 500
Sognefjorden	3,700	1,250
Bjørnafjorden	4,000 - 5,000	500 - 600
Langenuen	1,300	500
Boknafjorden (Rogfast Subsea tunnel)	26,700	390

1.1.2 Crossing Methods

As summarized in *Table 1.1*, the geographical conditions are harsh and it is difficult and expensive to install traditional bridge type solutions. Alternative methods have therefore been proposed, such as suspension bridge with fixed or floating towers, side-anchored

straight floating bridge, end-anchored curved floating bridge, submerged floating tube tunnel, and subsea tunnel. Different solutions have been proposed depending on the fjord.

1.2 Bjørnafjorden

1.2.1 Location

Bjørnafjorden is located in Hordaland county about 30 km south of Bergen. The width and the depth of the fjord are approximately 5 km and 600 m respectively. As illustrated in *Figure 1.2*, the proposed curved floating bridge will be installed over Bjørnafjorden and connect Svarvahella at Rekstern and Søre Øyane.

Figure 1.2: Geographical location of the floating bridge on Bjørnafjorden.

1.2.2 Crossing Methods

To cross Bjørnafjorden, three methods have been proposed: end-anchored curved floating bridge, submerged floating tube tunnel, and multi-span suspension bridge supported by TLP. The illustrations and designs of the proposed crossing methods are presented in *1.3*, *1.4*, and *Figure 1.5*. In this paper, the viscous effects and the global dynamic responses of the end-anchored cable-stayed curved floating bridge are discussed.

(a) Illustration

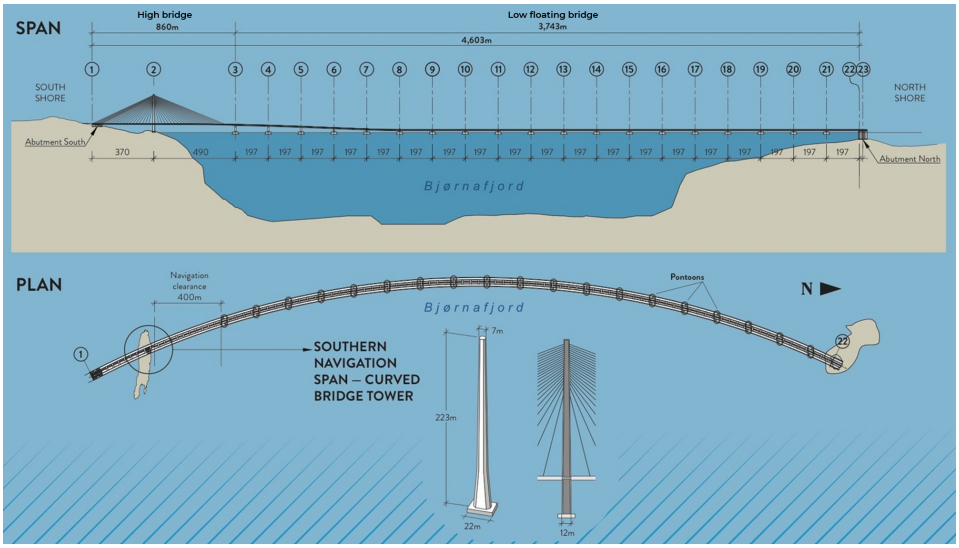

(b) Design

Figure 1.3: End-anchored cable-stayed curved floating bridge: (a) Illustration and (b) Design, images from [17], [20].

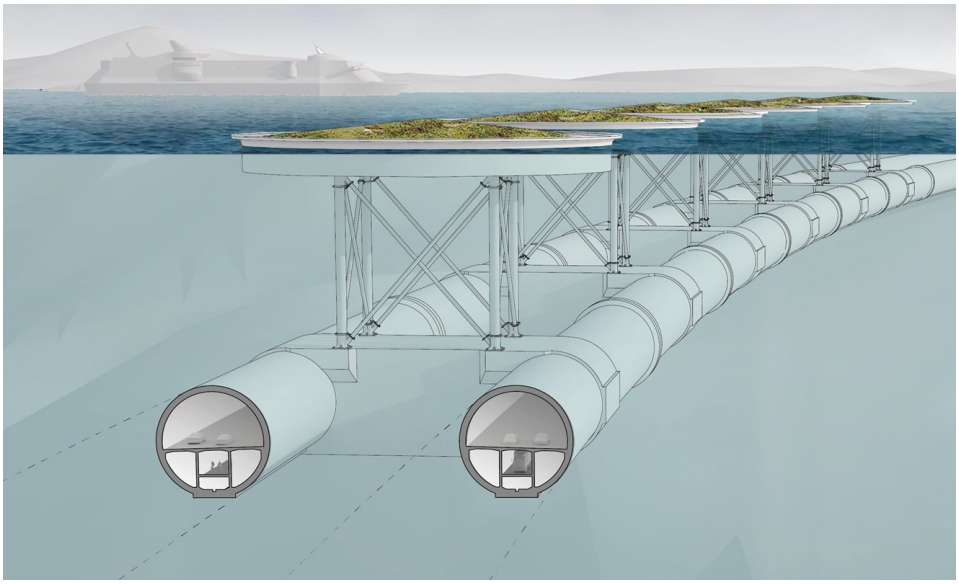

(a) Illustration

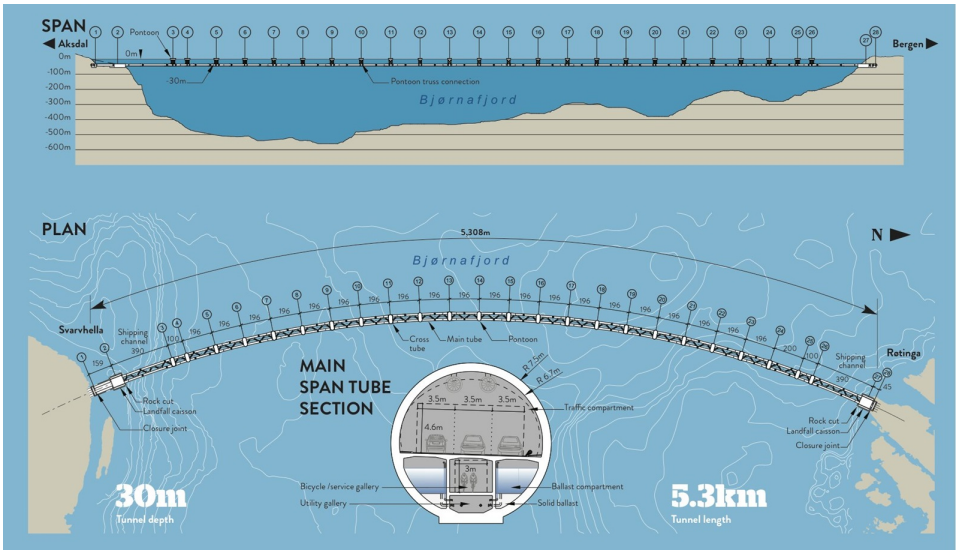

(b) Design

Figure 1.4: Submerged floating tube tunnel: (a) Illustration and (b) Design, images from [17], [20].

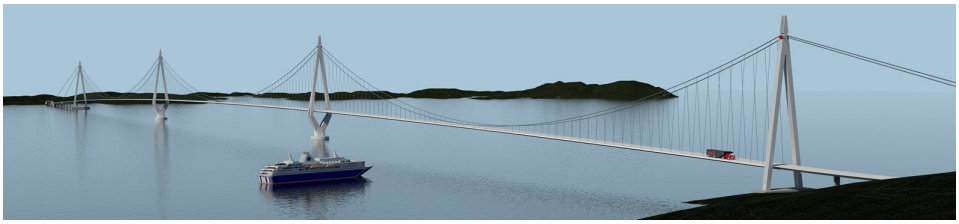

(a) Illustration

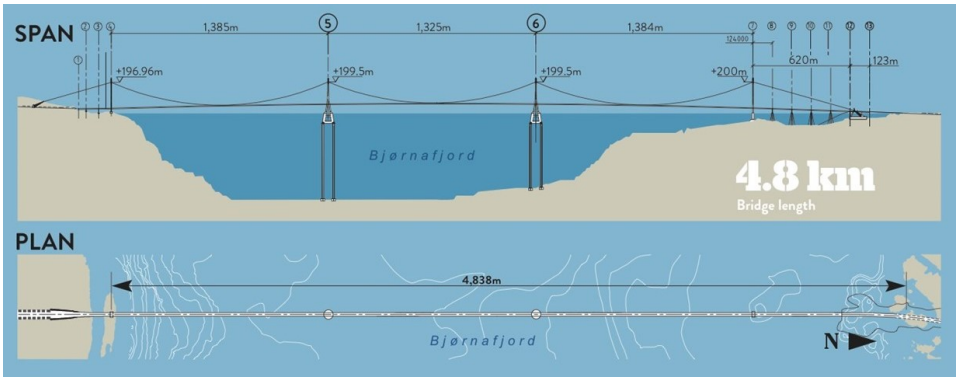

(b) Design

Figure 1.5: Multi-span suspension bridge supported by TLP: (a) Illustration and (b) Design, images from [17], [20].

1.2.3 Environmental Conditions

The environmental condition of the fjord is a combination of waves and wind. Depends on the directions of the wind and wave conditions, the environmental load becomes larger or smaller. When wind and waves come from the same direction, the bridge will experience the most severe environmental load. Therefore, proper modeling of the environmental conditions is necessary for a bridge design phase.

Wind Wave

Cheng et al. analyzed wave data measured at Bjørnafjorden by NPRA [5]. In the fjord, the condition of the sea has been found not to be the same as the open sea, and the condition of the sea is often complicated due to the wave conditions combined with the wind-generated waves and swell. Based on the hindcast wind data in Bjørnafjorden from 1979 to 2015, Norconsult simulated and estimated 100-year waves induced by local wind and 100-year swell conditions.

Table 1.2 summarized the estimated waves due to local wind. The sectors of wave conditions indicate the direction where the wave condition coming from. 360 °and 0 °represent the north, 90 °, 180 °and 270 °represent the east, the south and the west. The global coordinate system of can be found in *Figure 1.11a* in the following section. The largest significant wave height is found as $H_s = 2.8\ m$ with a peak period of $T_p = 6.6\ s$ from the east, the sector between $75°$ and $105°$. Waves induced by local wind from the west and the northwest have relatively higher significant wave height of around 2.5 m with a peak period of around 6 s. Waves from the north, the south and the southeast are smaller than other sectors. The most probable wind-generated waves are coming from 270 °.

Table 1.2: 100-year waves due to local wind in Bjørnafjorden [15].

Sectors	$H_s\ [m]$	$T_p\ [s]$
345° - 75°	1.5	5.0
75° - 105°	2.8	6.6
105° - 165°	1.6	5.3
165° - 225°	1.9	5.3
225° - 315°	2.4	5.9
315° - 335°	2.5	6.2
335° - 345°	2.0	5.6

Swell

100-year swell data is summarized in *Table 1.3*. Two different types of swell conditions were estimated from the same direction in Bjørnafjorden. The swell with the significant wave height of 0.4 m is with a range of peak period between 12-16 s, while the swell with 0.2 m of wave height is with a range of peak period between 17-20 s. Both swell conditions come from 205 °and 320 °sectors. Among two swell conditions, more than 80 $\%$ of the swell energy comes from the sector $320°$. Furthermore, it should be noted that when the local wind blows from 270 °, the swell will be combined with the wind-generated waves [15].

Table 1.3: 100-year swells in Bjørnafjorden [6][15].

Sector	$H_s\ [m]$	$T_p\ [s]$
205°	0.4	12-16
205°	0.2	17-20
320°	0.4	12-16
320°	0.2	17-20

Wind

Based on the measurements, simulations, and analysis performed by Kjeller vindteknikk [8], the wind conditions in Bjørnafjorden were estimated. The 1-hour mean wind speed at 10 m height for the 100-year return period is 29.5 m/s. The wind speed with different return period can be found the design basis [15]. By multiplying the reduction coefficient to the 1-hour mean speed, the extreme wind speed in different wind directions can be obtained. *Table 1.4* shows the 100-year wind data in Bjørnafjorden in different wind direction sectors. The wind profile can be described with the power law given in (2.16).

Table 1.4: 100-year winds in Bjørnafjorden [15].

Sectors	U_w $[m/s]$
0° - 75°	20.65
75° - 225°	25.08
225° - 255°	26.55
255° - 285°	29.50
285° - 345°	26.55
345° - 360°	20.65

1.3 Cable-stayed Curved Floating Bridge

1.3.1 Overview

The cable-stayed curved floating bridge design was prepared by COWI et al. [6]. The given bridge design consists of a high bridge section and a low floating bridge section, as can be seen in *Figure 1.6a*. The total length of the bridge including the high bridge and the low bridge sections is 4600 m. The bridge girder is curved toward the west with a curvature of 5000 m in radius as shown in *Figure 1.6b*. This curvature eliminates the need for a mooring line because the curved bridge works as an arch that can withstand horizontal environmental loads as compressive loads.

High Bridge Section

The high bridge section is located on the south side of the bridge for the ship passage and hangs on 80 cables connected from the tower. The abutment is on axis 1 and the tower is on axis 2. The back span between the abutment and the tower is 370 m and the main span between the tower and the first pontoon is 490 m. The height of the first pontoon on axis 3 is around 40 m due to the ship passage. The total length of the high bridge section is 860 m.

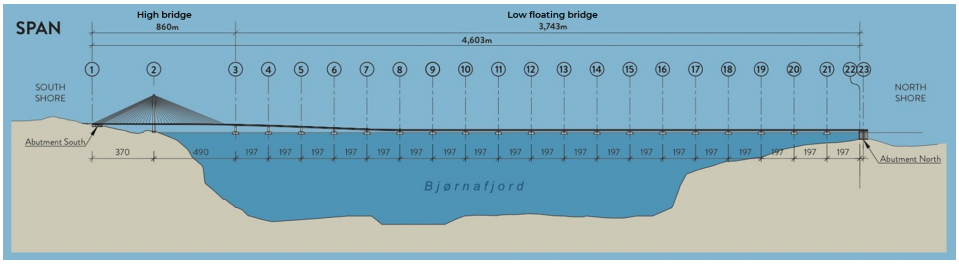

(a) Span

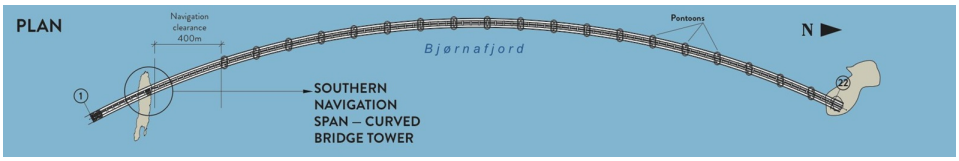

(b) Plan

Figure 1.6: Overview and nomenclature of the cable-stayed curved floating bridge: (a) Span and (b) Plan [6] [20].

Low Floating Bridge Section

The length of the low floating bridge section is 3743 m and it is supported by 19 pontoons located on axes 3 to 21 and ends on the abutment located on north axis 23. The pontoons and the main girder are connected by two columns per axis and the height of the columns are around 7.5 m.

1.3.2 Bridge Girder

The bridge girder consists of two parallel boxes and a center bridge. The main dimensions of the superstructure are different for the high bridge section and the low bridge section, as can be found in *Figure 1.7*. The high bridge section is designed with three cross-sections of H1, H2, and H3, and the low bridge section has two cross-sections, S1 and F1. The arrangement of the cross-sections can be found in *Figure 1.8*. The material for the bridge girder is S460 steel and the detail structural properties of the cross-sections are summarized in *Table 1.5* [6].

1.3.3 Pontoons

The low floating bridge section is supported by 19 pontoons with a length of 28 m, a width of 68 m and height of 14 m. COWI et al. conducted the initial optimization of the pontoon design and attached a flange with a width of 5 m as illustrated in *Figure 1.9*. The flange can provide an increased added mass of the pontoon and shift the eigen period of

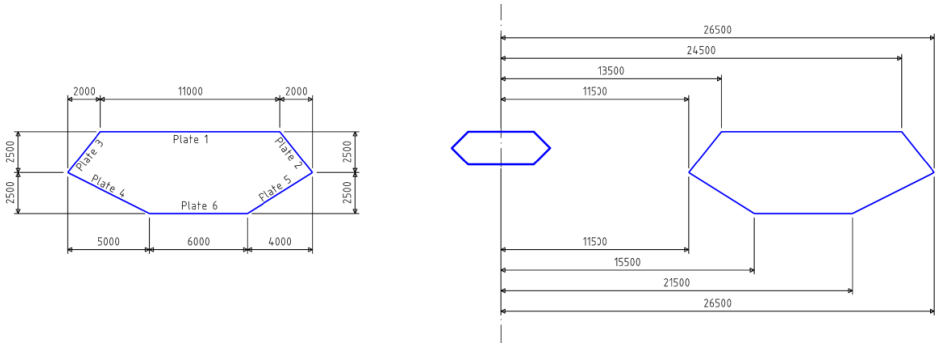

(a) Cross-section dimensions for the high bridge girder

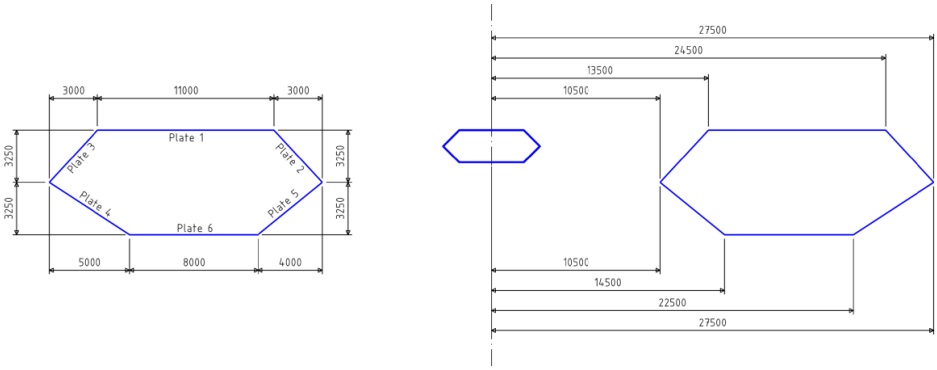

(b) Cross-section dimensions for the low bridge girder

Figure 1.7: Cross-section dimensions for (a) High bridge girder and (b) Low bridge girder [6].

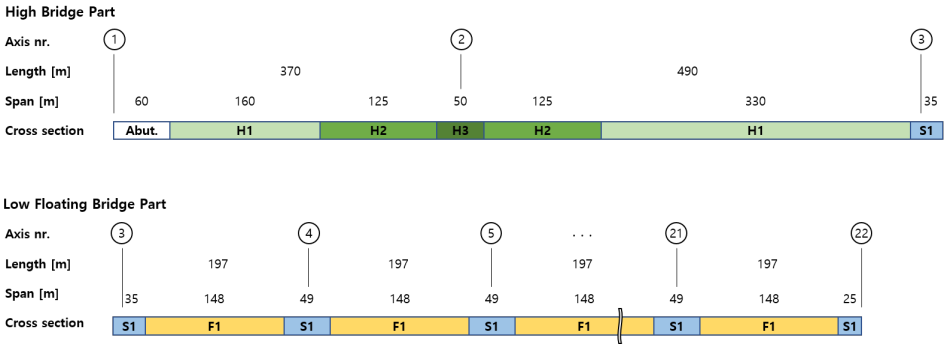

Figure 1.8: Arrangement of the cross-sections of the bridge girder [6].

Table 1.5: Structural properties of the bridge girder [6].

		H1	H2	H3	S1	F1
Area	$[m^2]$	1.46	2.10	2.63	2.50	1.85
I_z	$[m^4]$	554.2	809.1	1011.4	1037.0	737.9
I_y	$[m^4]$	6.10	9.38	11.72	18.34	13.16
I_x	$[m^4]$	17.5	24.5	30.7	45.8	35.9
EA	$[kN]$	3.07 E+08	4.41 E+08	5.52 E+08	5.25 E+08	3.89 E+08
EI_z	$[kNm^2]$	1.16 E+11	1.70 E+11	2.12 E+11	2.18 E+11	1.55 E+11
EI_y	$[kNm^2]$	1.28 E+09	1.97 E+09	2.46 E+09	3.85 E+09	2.76 E+09
GI_x	$[kNm^2]$	1.42 E+09	1.98 E+09	2.49 E+09	3.71 E+09	2.91 E+09
Mass	$[ton/m]$	23.96	29.05	33.13	31.80	26.71
Load	$[kN/m]$	235	285	325	312	262

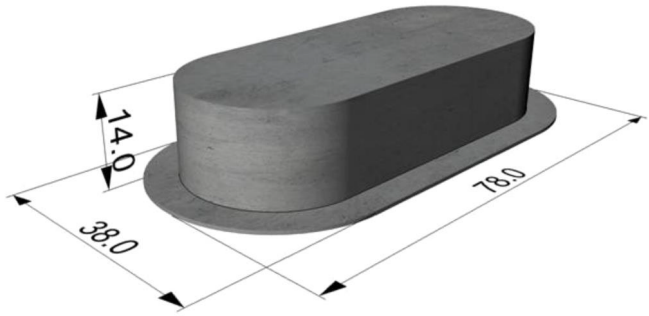

Figure 1.9: Main dimension of the pontoon [6].

the vertical motion of the bridge. The initial eigen periods for the vertical mode shapes were between 6.4 s to 8 s, while the wave conditions are in the range of 3 s to 6 s and 12 s to 20 s for the wind-generated waves and swell respectively. After attached the flange, the range of the eigen periods was shifted between 7.8 s to 10.8 s. The added flange also can generate a viscous effect; thus, it is important to understand the viscous contribution of the given pontoon design. The material of the pontoon is LB55 concrete and the main parameters of the pontoon are summarized in *Table 1.6*.

1.3.4 Columns

Each pontoon is connected to the superstructure by two columns spaced 37 m apart from each other as described in *Figure 1.10*. The height of the column is reduced from about 40 m to 7.5 m along the bridge axis from south to north because the ship passes under the south high bridge. The column height at each axis is summarized in *Table 1.7*. The diameter of the column is 8 m in all cases, but the thickness of the plate depends on the height. The detail properties of the column are summarized in *Table 1.8*. Given parameters

Table 1.6: Parameters of the pontoon [6].

Parameter		
Length	$[m]$	28.0
Width	$[m]$	68.0
Height	$[m]$	14.0
Flange	$[m]$	5.0
Draft	$[m]$	10.5
Freeboard	$[m]$	4.0
Center of Gravity	$[m]$	(0, 0, -4.2)
Displacement	$[ton]$	18,300
Mass	$[ton]$	11,300
Roll inertia	$[ton \cdot m^2]$	4.90 E+06
Pitch inertia	$[ton \cdot m^2]$	1.36 E+06
Yaw inertia	$[ton \cdot m^2]$	5.7 E+06
Roll water plane stiffness	$[MNm/rad]$	5700
Pitch water plane stiffness	$[MNm/rad]$	1000
Heave stiffness	$[MN/m]$	17.5

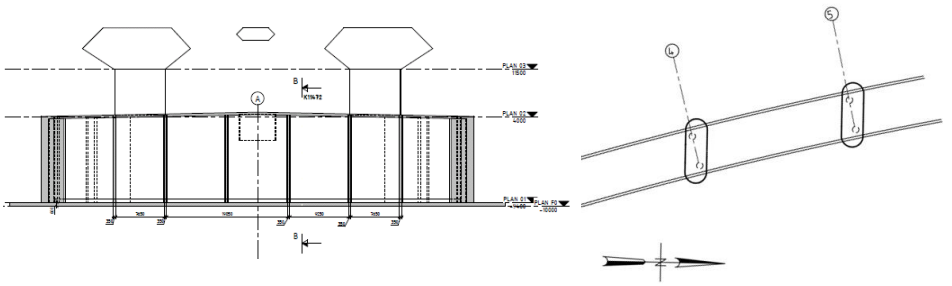

Figure 1.10: Arrangement of pontoons and columns [6].

Table 1.7: Column heights at each axis [6].

Axis	3	4	5	6	7	8	9 - 21
Height $[m]$	39.998	34.773	27.215	19.335	11.455	7.501	7.5

only show one column, one should consider double the value per axis.

1.3.5 Other Parts

Details of other parts of the given bridge design including the abutments, the tower, and the cable stays can be found in [6].

Table 1.8: Parameters of the column [6].

Parameter (two per axis)		Axis 3-6	Axis 7-21
Diameter	$[m]$	8.0	8.0
Plate thickness	$[m]$	0.040	0.030
Effective thickness vertical	$[m]$	0.055	0.035
Effective thickness total	$[m]$	0.060	0.040
Area	$[m^2]$	1.37	0.88
Bending inertia	$[m^4]$	10.83	6.95
Torsion inertia	$[m^4]$	21.66	13.89
Bending modulus	$[m^3]$	2.71	1.74
Torsion modulus	$[m^3]$	5.42	3.47
Mass	$[ton/m]$	12	8

1.3.6 Global Coordinate System

The definitions of the global coordinate system, the orientation, and the 6 degrees of freedom of the bridge are described in *Figure 1.11*. The origin in the global coordinate system is the south end of the bridge. X indicates the axis from the south to the north, Y indicates the axis from the east to the west, and Z indicates the upward axis from the water surface. The main focus of this paper is heave and sway motions. Heave and sway motions represent the vertical and horizontal motion of the bridge.

1.3.7 Eigen Modes

As discussed earlier, the given bridge design is with around 5 km long, supported by 19 floating pontoons without mooring. Although all pontoons are apart from each other and far enough to neglect the hydrodynamic interactions, the pontoons are connected to the continuous and flexible bridge girder. The vertical response of a pontoon is mainly due to waves; thus, complicated vertical mode shapes are expected. The horizontal motion of the bridge is mainly influenced by wind. Therefore, the horizontal mode shapes are expected to have longer eigen periods than the vertical mode shapes. *Figure 1.12* describes two samples of eigen mode shapes of the floating bridge in heave motion. The top figure is the mode shape with the longest eigen period of 10.95 s and the bottom figure is the mode shape with the shortest eigen period of 7.5 s. The samples of the horizontal mode shapes estimated from the numerical simulations are presented in *Figure 1.13*. The first sway mode shape is with the longest eigen period of 56.72 s and the second sway mode shape is with the eigen period of 31.69 s.

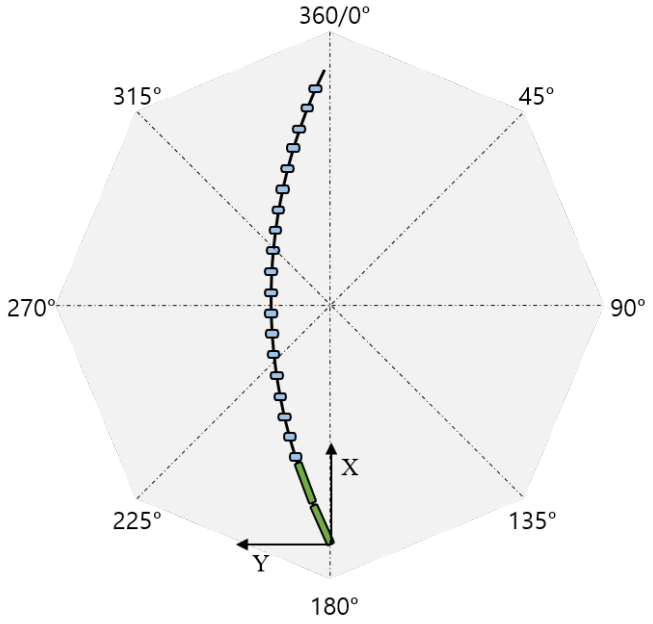

(a) Global coordinate system and orientation

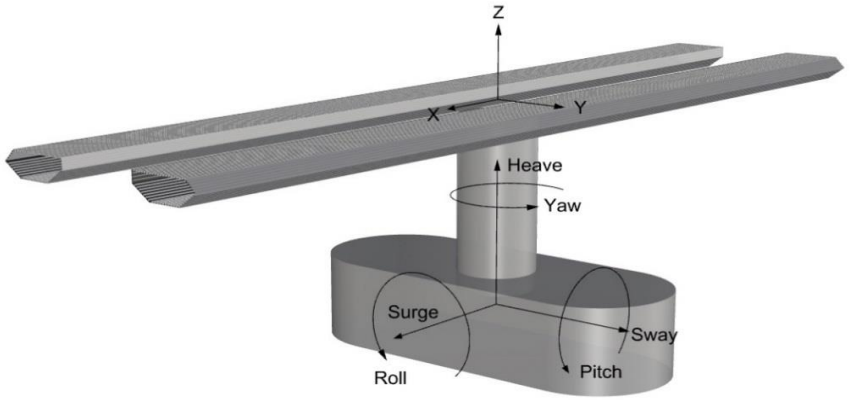

(b) 6 degrees of freedom

Figure 1.11: Definition of (a) Global coordinate system and orientation and (b) 6 degrees of freedom.

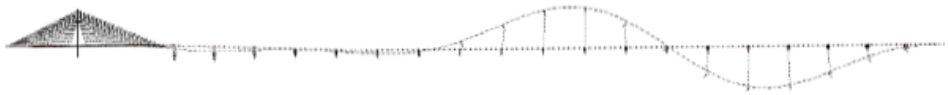

(a) Heave mode shape with the longest eigen period of T_p = 10.95 s

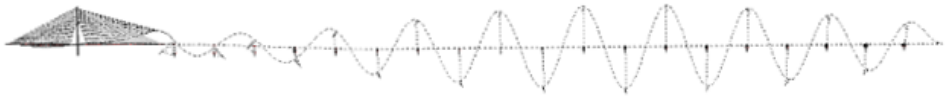

(b) Heave mode shape with the shortest eigen period of T_p = 7.5 s

Figure 1.12: Vertical eigen mode shapes: (a) Heave mode shape with the longest eigen period and (b) Heave mode shape with the shortest eigen period [6].

(a) First sway mode shape with eigen period of T_p = 56.72 s

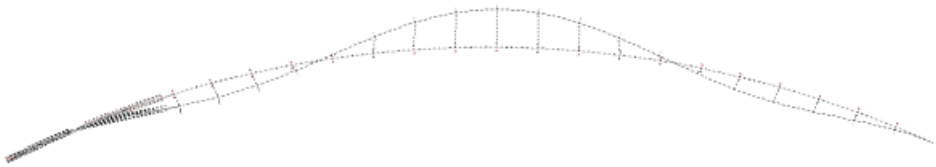

(b) Second sway mode shape with eigen period of T_p = 31.69 s

Figure 1.13: Horizontal eigen mode shapes: (a) First sway mode shape and (b) Second sway mode shape [6].

1.3.8 Hydrodynamic properties from Wadam

Cheng provided the hydrodynamic properties for the pontoons of the given floating bridge design. The added mass and the potential damping for the pontoons were calculated in Wadam and can be illustrated as *Figure 1.14* and *1.15*. The obtained hydrodynamic properties are used in the analysis of various damping sources.

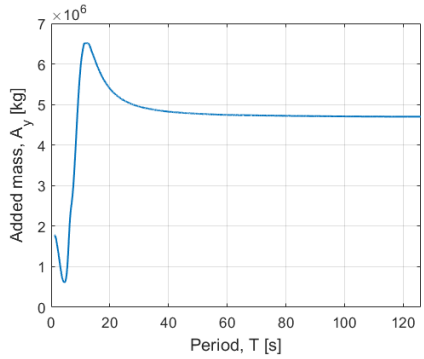

(a) Added mass in y-axis

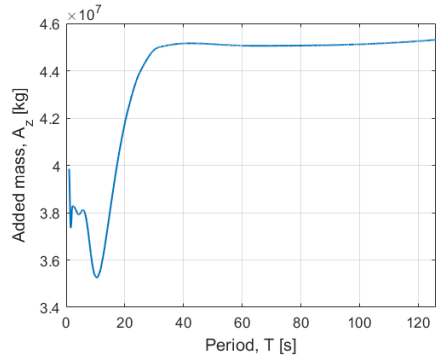

(b) Added mass in z-axis

Figure 1.14: Added mass of the pontoon in (a) y-axis and (b) z-axis obtained from Wadam.

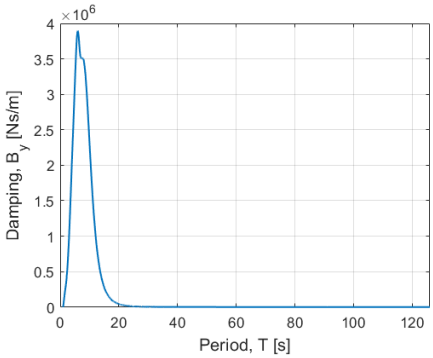

(a) Potential damping in y-axis

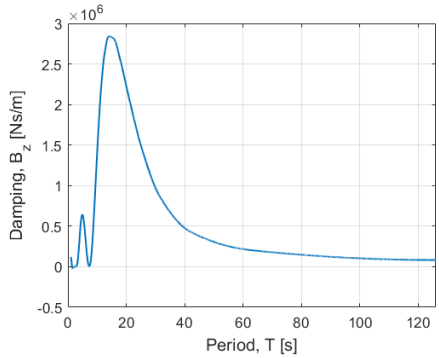

(b) Potential damping in z-axis

Figure 1.15: Potential damping of the pontoon in (a) y-axis and (b) z-axis obtained from Wadam .

Chapter 2

Methods and Theories

The main purpose of this study is to investigate the effect of various damping on the global dynamic responses of the proposed floating bridge design for Bjørnafjorden. This work has been done in several steps using different methods and theories. The procedure of this study, methods, and theories used in each step are summarized in the flowchart, *Figure 2.1*.

First, based on the field measurements, simulations and estimates of the environmental conditions in Bjørnafjorden, the environmental conditions for simulations are defined. Numerical simulations in SIMO-RIFLEX are performed by using the given numerical model provided by Cheng, and dynamic responses of the floating bridge without viscous effect are obtained. The obtained heave response is used in KC number calculation and the viscous damping for the heave response is modeled by the KC number dependent drag coefficient. The viscous damping for surge and sway motions are modeled by the DNV recommendation. After modeling the viscous damping terms, free decay tests are performed to investigate the various damping contributions. For the decay tests, virtual external forces are applied to specific points and then released after a certain period of time to observe the subsequent responses. Finally, the second numerical simulations in SIMO-RIFLEX including viscous effect are performed. Several global dynamic responses are measured including heave and sway motions, axial force, bending moments about the weak axis and the strong axis, and the corresponding stresses. Statistical analysis and spectral analysis are followed by the simulations to understand the phenomena of the floating bridge with or without viscous effects in various environmental conditions.

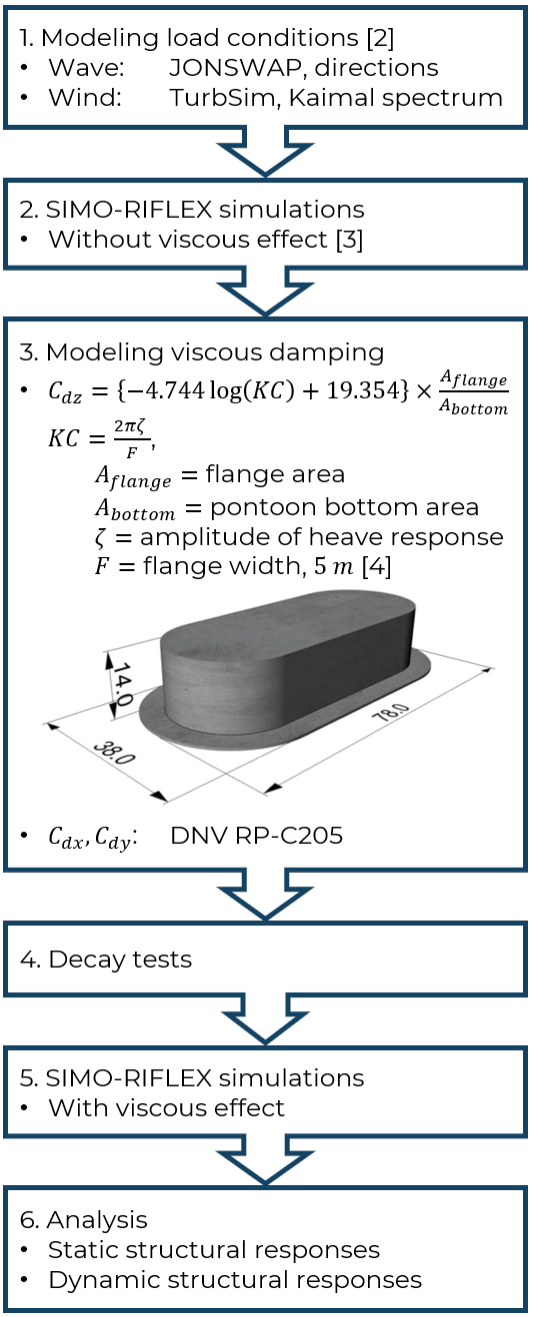

Figure 2.1: Methods and theories flow chart.

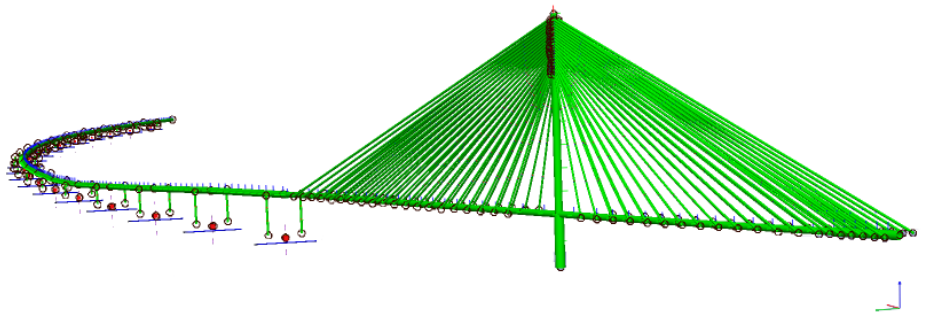

Figure 2.2: Numerical model of the floating bridge in SIMO-RIFLEX provided by Cheng et al. [3].

2.1 Numerical Model of the Floating Bridge

The detail design of the floating bridge was provided by COWI et al. as a part of E39 project. The numerical model of the bridge was prepared by Cheng and used in his studies in hydrodynamic load modeling and analysis of the floating bridge [3]. The numerical model was built that run on the platform named SIMA. The programs are developed by MARINTEK, current SINTEF and have been used in various analysis for offshore platforms including wind turbines. SIMO is used for motion analysis on multi-body systems in the time domain [10], whereas RIFLEX is used for hydrodynamic and structural analysis on a slender body marine structures [9].

Figure 2.2 illustrates the overview of the numerical model built in SIMO-RIFLEX prepared by Cheng. The bridge girder was designed with 3 parallel steel boxes with different dimensions for the high bridge and the low bridge as can be seen in *Figure 1.7*. In the numerical model, however, only the high bridge girder dimension was used and simplified into one equivalent girder and modeled as nonlinear beam elements. The bridge tower and columns were also modeled as nonlinear beam elements. The pontoons were modeled as rigid bodies, while the cables for the high bridge section were pre-tensioned and modeled as nonlinear bar elements. All connections between the cable-ends and the girder, the girder, and the columns, and the pontoons and the columns were connected as rigid master and slave.

Cheng compared the eigen periods obtained from SIMO-RIFLEX simulations to the periods estimated by COWI et al. [3]. The errors related to the vertical and horizontal motions of the bridge are less than 4 % and 10 % respectively. Thus, it is validated that the numerical model can be used for the analysis of the dynamic responses of the floating bridge. The

eigen periods of the bridge with the viscous effect obtained from decay tests are discussed in 3.6.

2.1.1 Structural Damping

The Rayleigh damping is used to model the structural damping of the bridge with the corresponding damping ratio as follows:

$$B = \alpha\, M + \beta\, C \tag{2.1}$$

$$b_i = \alpha\, m_i + \beta\, c_i \tag{2.2}$$

$$\lambda_i = \frac{1}{2}\left(\frac{\alpha}{\omega_i} + \beta\, \omega_i\right) \tag{2.3}$$

(2.1) describes the relation between damping of the system B, mass M and the stiffness of the system C. α and β are the damping coefficients for mass and the stiffness of the system respectively. (2.2) is the expression for the modal damping b_i with the modal mass m_i and the modal stiffness c_i in i'th mode. (2.3) shows the damping ratio λ_i and the relation with the eigen frequency of ω_i in i'th mode.

The damping coefficients of $\alpha = 0.0005$ and $\beta = 0.03$ were applied in the simulations. Cheng et al. approximated the first and second damping ratio as $\lambda_1 = 0.0142$ and $\lambda_2 = 0.084$ [3].

2.1.2 Numerical Time Integration

The Newmark β-family iteration method is used to solve the dynamic equilibrium equations in RIFLEX [9]. Newmark β-family method is a step-by-step implicit method which is widely used to solve differential equations. In order to obtain the displacement u_{k+1} and the velocity $\dot{u}_{k+1}$ at the next time step $t = k + 1$, the displacement u_k, velocity $\dot{u}_k$ and the acceleration $\ddot{u}_k$ at the current time step $t = k$ and the acceleration $\ddot{u}_{k+1}$ at the next time step $t = k + 1$ are required [11]. The velocity and the displacement at $t = k + 1$ are given by:

$$\dot{u}_{k+1} = \dot{u}_k + (1 - \gamma_{nb})\, h\, \ddot{u}_k + \gamma_{nb}\, h\, \ddot{u}_{k+1} \tag{2.4}$$

$$u_{k+1} = u_k + h\, \dot{u}_k + (0.5 - \beta_{nb})\, h^2\, \ddot{u}_k + \beta_{nb}\, h^2\, \ddot{u}_{k+1} \tag{2.5}$$

where γ_{nb} and β_{nb} are acceleration weight factors for the velocity and the displacement at $t = k + 1$ respectively. h is the constant time step. In the simulations, $h = 0.01\ s$, $\gamma_{nb} = 0.505$ and $\beta_{nb} = 0.256$ were used [3].

2.2 Environmental Condition Model

2.2.1 Wave Conditions

Norconsult AS conducted the numerical simulations to estimate 100-year wind-generated wave conditions in Bjørnafjorden [1]. The simulation was based on the hindcast wind data measured from 1979 to 2015. The 100-year local wind generated wave conditions in Bjørnafjorden are summarized in *Table 1.2* in the previous chapter.

2.2.2 Wave Elevation

The numerical simulation performed by Norcunsult represents that the wave conditions in Bjørnafjorden can be considered as short-crested irregular waves. Since the 3-hour sea state can be regarded as a stationary and Gaussian distributed, the elevation of the short-crested irregular waves at points (x, y) can be expressed as the sum of the wave components in all directions [13]:

$$\begin{aligned}\zeta(x,y,t) = \mathfrak{Re}\Bigg\{ &\sum_{n=1}^{N}\sum_{m=1}^{M} \zeta_a(\omega_n,\theta_m) \\ &\exp\Big(i\big(\omega_n t - k_n x\cos\theta_m - k_n y\sin\theta_m + \epsilon_{nm}\big)\Big)\Bigg\} \qquad (2.6)\end{aligned}$$

$$= \sum_{n=1}^{N}\sum_{m=1}^{M} \zeta_a(\omega_n,\theta_m)\sin\big(\omega_n t - k_n x\cos\theta_m - k_n y\sin\theta_m + \epsilon_{nm}\big) \qquad (2.7)$$

where,

$$\zeta_a(\omega_n,\theta_m) = \sqrt{2\,S_\zeta(\omega_n,\theta_m)\,\Delta\omega_n\,\Delta\theta_m} \qquad (2.8)$$

where x and y indicate the location of a pontoon in the global coordinate system and t is time. $\zeta_a(\omega,\theta)$ is the wave amplitude as a function of wave frequency ω and wave direction θ. $S_\zeta(\omega,\theta)$ denotes the wave spectrum including directional variations expressed in (2.9). N and M are the total number of wave frequencies and wave directions, and k is the related wave number. ϵ represents arbitrary phase angles uniformly distributed between 0 to 2π.

2.2.3 Wave Spectrum

The short-crest wave can be described by the JONSWAP spectrum with the constant significant wave height and the peak wave period. The theoretical wave spectrum for describing

swell conditions are not currently available. However, NPRA suggests that the JONSWAP spectrum can be used with specific peak shape parameter γ to describe the wave conditions for both wind-generated wave and swell in Bjørnafjorden [15]. Since the JONSWAP spectrum is a non-directional spectrum, directional distribution can be applied to generate waves with different directions. The wave spectrum generated by the JONSWAP spectrum with the directional distribution can be expressed as:

$$S_\zeta(\omega, \theta) = S_J(\omega)\, D(\theta) \tag{2.9}$$

where $S_J(\omega)$ is the JONSWAP spectrum as a function of angular wave frequency ω given in (2.10), while $D(\theta)$ is the directional distribution function with the wave direction θ described in (2.15).

JONSWAP Spectrum

The JONSWAP spectrum is given by [7]:

$$S_J(\omega) = A_\gamma \frac{5}{16} H_s^2\, \omega_p^4\, \omega^{-5} \exp\left(-\frac{5}{4}\left(\frac{\omega}{\omega_p}\right)^{-4}\right) \gamma^{\exp\left(-0.5\left(\frac{\omega-\omega_p}{\sigma\ \omega_p}\right)^2\right)} \tag{2.10}$$

where,

$$A_\gamma = 1 - 0.287\ \ln(\gamma) \tag{2.11}$$

$$\omega_p = \frac{2\pi}{T_p} \tag{2.12}$$

$$\sigma = \begin{cases} 0.07 & \text{for} \quad \omega < \omega_p \\ 0.09 & \text{for} \quad \omega \geq \omega_p \end{cases} \tag{2.13}$$

H_s is the significant wave height and T_p is the spectral peak period of the wave condition. A_γ is the normalizing factor as a function of γ. γ the non-dimensional peak shape parameter and σ the spectral width parameter. The peak shape parameter γ for the local wind-generated waves is recommended with the range between 1.8 - 2.3, while the range between 3 - 5 is recommended for the swell condition. If no specific peak shape parameter γ is given, it can be calculated as follows:

$$\gamma = \begin{cases} 5 & \text{for} \quad \frac{T_p}{\sqrt{H_s}} \leq 3.6 \\ \exp\left(5.75 - 1.15\frac{T_p}{\sqrt{H_s}}\right) & \text{for} \quad 3.6 < \frac{T_p}{\sqrt{H_s}} < 5 \\ 1 & \text{for} \quad 5 \leq \frac{T_p}{\sqrt{H_s}} \end{cases} \tag{2.14}$$

Directional Distribution Function

The directional distribution function is given by [7]:

$$D(\theta) = \frac{\Gamma(1+n/2)}{\sqrt{\pi}\,\Gamma(1/2+n/2)} \cos^n(\theta - \theta_p), \qquad |\theta - \theta_p| \leq \frac{\pi}{2} \tag{2.15}$$

where Γ is the Gamma function, θ_p is the main wave direction and n is the directional spreading parameter. The directional spreading parameter of 4 is recommended for the local wind-generated wave, while the range of 10-20 is recommended for the swell condition.

2.2.4 Wind Condition

Based on the numerical estimates for wind condition in Bjørnafjorden, the wind profile can be described with the power law and the wind field can be generated by TurbSim.

Wind Profile

The wind profile is given by the power law relation as follows:

$$U_w(z) = U_{w,ref}\left(\frac{z}{z_r}\right)^{\alpha} \tag{2.16}$$

where U_w is the mean wind speed at height z, $U_{w,ref}$ is the mean wind speed at the reference height z_{ref} of 10 m and α is the profile factor. NPRA suggests $\alpha = 0.127$ for the wind profile [15].

Wind Field

For the numerical simulation, the wind field is generated by TurbSim [2] with the given wind speed, wind profile factor, the turbulence intensity of 14 $\%$, and the Kaimal spectrum defined in N400 handbook [16]. N400 handbook is prepared by NPRA and recommended to be used in the design of the floating bridge for Bjørnafjorden [15]. The details of the wind field generated by TurbSim with N400 Kaimal spectrum can be found in Cheng et al. [4].

2.3 Hydrodynamic Loads

The hydrodynamic loads modeling for the given floating bridge was conducted by Cheng et al. [3]. Since the pontoons in the numerical model are considered as large volume

structures, the hydrodynamic coefficients including added mass and radiation damping for the pontoons are estimated with the potential flow theory [13]. The fjord wall effect on hydrodynamic coefficients was not considered in this study. Since the distance between pontoons of 197 m is approximately 4 times larger than the local wind-generated waves, the hydrodynamic interaction between adjacent pontoons was also neglected.

2.3.1 Equation of Motion in Time Domain

The general equation of the motion of the pontoon in time domain can be expressed by using the Cummins Equation as follows [19]:

$$\sum_{j=1}^{6} \left\{ \left(M_{ij} + A_{ij}^{\infty} \right) \ddot{u}_j(t) + \int_0^{\infty} B_{ij}(\tau)\, \dot{u}_j(t-\tau)\, d\tau + C_{ij}\, u_j(t) \right\} = F_i^{ext}(t) \tag{2.17}$$

where i and j are degrees of freedom, the excitation force $F^{ext}(t)$ in the right hand side is balanced with the inertia, damping and the restoring force terms in the left hand side. The inertia force is described with the mass of the pontoon M, the added mass at infinite frequency A^{∞} and the acceleration of the pontoon $\ddot{u}(t)$. The damping force is expressed with the retardation function $B(\tau)$ and the velocity of the pontoon $\dot{u}(t)$. The retardation function is a result of the memory effect of the fluid in the time interval of τ. The restoring force is described with the restoring coefficient C and the displacement of the pontoon $u(t)$. The restoring force includes the nonlinear restoring force due to the bridge girder stiffness and the hydrostatic restoring force due to buoyancy. The excitation force $F^{ext}(t)$ includes the first order wave force $F^{1st}(t)$ and the the drag force $F^{drag}(t)$. The second order wave force is not considered in this study.

$$F^{ext}(t) = F^{1st}(t) + F^{drag}(t) \tag{2.18}$$

2.3.2 First Order Wave Force

With the given wave elevation ζ in (2.6) and the wave amplitude ζ_a in (2.8), the first order wave force in time domain can be obtained with the corresponding transfer function

$H(\omega, \theta)$:

$$F^{1st}(t) = \mathfrak{Re}\Bigg\{ \sum_{n=1}^{N} \sum_{m=1}^{M} \big|H(\omega_n, \theta_m)\big|\zeta_a(\omega_n, \theta_m) \exp\Big(i\big(\omega_n t - k_n x \cos\theta_m - k_n y \sin\theta_m + \epsilon_{nm} + \phi_{H,nm}\big)\Big)\Bigg\} \tag{2.19}$$

ϕ_H represents the phase angle between the first order wave force and the relevant transfer function.

2.3.3 Drag Force

Viscous drag force is estimated by Morison's equation:

$$F^{drag}(t) = \frac{1}{2}\,\rho\, C_d\, A\, \dot{u}_r(t)\,|\dot{u}_r(t)| \tag{2.20}$$

where ρ is the water density, C_d is the quadratic drag coefficient, A is projected area, and $\dot{u}_r$ is the relative velocity between the wave velocity and the body response velocity. Since drag coefficient is an essential parameter for estimating viscous drag, it is important to model appropriate coefficients.

2.3.4 KC Dependent Drag Coefficient

Shao et el. conducted a model test and suggested the Keulegan–Carpenter (KC) number dependent drag coefficient in z-axis for a pontoon with a flange of a floating bridge [14]:

$$C_{dz,kc,flange} = -3.597\,\log(KC) + 15.733 \tag{2.21}$$

$$C_{dz,kc,bottom} = -4.744\,\log(KC) + 19.354 \tag{2.22}$$

KC dependant drag coefficient from (2.21) can be used for estimating the drag force induced by the flange itself, while the coefficient from (2.22) can be used for estimating the total drag force due to the total bottom plate of the pontoon including the flange.

KC number can be defined as the ratio between the distance with the relative oscillatory velocity U_m during the oscillation period T and the characteristic body length D [13]:

$$KC = \frac{U_m T}{D} \tag{2.23}$$

In a linear sinusoidal wave, the oscillatory flow velocity U_m can be defined as:

$$U_m = \omega\zeta_a = \frac{2\pi\zeta_a}{T} \tag{2.24}$$

where ζ_a is the incident wave amplitude, but it also can represent the amplitude of the body oscillation. Thus, KC number can be rewritten with the flange width F as the characteristic length as follows:

$$KC = \frac{2\pi\zeta_a}{F} \tag{2.25}$$

The suggested KC number above (2.25) is tuned with the flange width as the characteristic length and the drag coefficient described in (2.21) and (2.22) can be used with the flange area A_{flange} as the projected area to calculate the relevant drag force in z-axis. Therefore, the conventional drag coefficient in z-axis corresponding to the bottom plate area A_{bottom} as the projected area can be obtained as:

$$C_{dz} = C_{dz,kc}\,\frac{A_{flange}}{A_{bottom}} \tag{2.26}$$

2.3.5 Quadratic Drag and Damping

In the numerical model in SIMA, the viscous term is applied as quadratic damping or quadratic drag expressed in (2.27) and (2.28). Viscous terms for x-, y-, and z-axis are applied as quadratic damping for all simulations. Quadratic drag only for z-axis is applied for comparison. In the given model, quadratic damping acts on the rigid body points of the pontoons, while quadratic drag is applied on slender elements in a straight line along the y-axis and acts on divided several elements automatically. Therefore, the applied value should be divided by the length of the straight line. The length of the straight line is the same as the width of the pontoon of $W = 78\ m$ as described in Figure 1.9.

$$Q_{damp} = \frac{1}{2}\,\rho\,C_d\,A \tag{2.27}$$

$$Q_{drag,z} = \frac{1}{2}\,\rho\,C_d\,\frac{A}{W} \tag{2.28}$$

2.4 Free Decay Tests

After modeling the viscous terms for the given floating bridge design, free decay tests were performed to understand the contributions from different damping terms. Natural periods

and damping ratio in different modes were retrieved and compared. Since the bridge is supported by 19 pontoons, the mode shapes of the bridge are complex and combined with responses of different pontoons. Therefore, the response of the one part of the bridge containing bridge girder, column and pontoon as described in *Figure 1.11b* was taken into account in the free decay tests.

2.4.1 Natural Period

The natural period of the system can be obtained by the mass and the hydrodynamic properties of the pontoon as follows:

$$T_n = 2\pi\sqrt{\frac{M+A}{C}} \tag{2.29}$$

Mass M includes the mass of one pontoon, two columns and the part of the bridge girder. Since the main interest is the response of the low floating part of the bridge, the structural properties for the low bridge, including the cross-section of the bridge girder and the column length are applied. Through the measured time and the number of oscillation in the free decay test, the natural period of the system can be obtained as the mean of the oscillation cycle:

$$T_n = T_{mean} = \frac{\Delta t}{N} \tag{2.30}$$

where Δt is the measured time and N is the number of oscillation cycle in free decay test.

2.4.2 Damping Ratio

The damping ratio λ can be obtained from the free decay test with the measured number of oscillation cycle N and the positive maximum displacements z:

$$\lambda = \frac{1}{2\pi N}\ln\left(\frac{z_0}{z_N}\right) \tag{2.31}$$

where z_0 is the initial displacement before the decay test begin and z_N is the maximum positive displacement at N'th cycle of the oscillation. The damping ratio is also the ratio between total damping to the critical damping:

$$\lambda = \frac{B_{tot}}{B_{cr}} \tag{2.32}$$

The critical damping can be obtained with mass, added mass and natural frequency of the system:

$$B_{cr} = 2\left(M + A(\omega_n)\right)\omega_n \tag{2.33}$$

With the obtained damping ratio and the critical damping, the total damping of the system can be calculated as follows:

$$B_{tot} = \lambda\, B_{cr} \tag{2.34}$$

As described previously, the structural damping is modeled as Rayleigh damping with damping coefficients of $\alpha = 0.0005$ and $\beta = 0.03$. The structural damping ratio and the structural damping is given by:

$$\lambda_{str} = \frac{1}{2}\left(\frac{\alpha}{\omega_n} + \beta\,\omega_n\right) \tag{2.35}$$

$$B_{str} = \lambda_{str}\, B_{cr} \tag{2.36}$$

The total damping of the given design consists of the potential damping and the structural damping. The potential damping is obtained from Wadam as described in *Figure 1.15*. When the viscous term is included in the system, the total damping can be expressed as:

$$B_{tot} = B_{pot} + B_{str} + B_{vis} \tag{2.37}$$

The contribution of the viscous effect is obtained as linearized viscous damping by subtracting the potential and structural damping terms from the total damping. Since the bridge girder is continuous and flexible structure, the theoretically calculated structural damping can differ from the damping in simulations in different responses. Therefore, it should be noted that the exact viscous damping effect can differ in different responses. However, from the linearized viscous damping, the general idea of the contribution of viscous effect can still be captured.

2.5 Analysis

After the modeling of the viscous drag coefficients for the bridge, SIMO-RIFLEX simulations were conducted to obtain the global dynamic responses of the bridge inclusive of the viscous effect. The heave and sway motions, the bending moments about the week axis and the strong axis, the axial force and etc. were retrieved for post-processing. The statistical and the spectral characteristics of the responses were investigated to understand the

phenomena of the floating bridge under static and dynamic conditions, including 100-year local wind-generated wave, swell, wind and the combination of both the wind and wave conditions.

2.5.1 Bridge Girder Normal Stress

Since the given bridge design is curved, external forces on the bridge are delivered as compressive forces thus, the bridge girder normal stress was analyzed. The analyzed bridge girder stresses are stresses due to axial force, week axis bending moment and strong axis bending moment. The bridge girder normal stress is given by:

$$\sigma_{tot} = \sigma_{F_a} + \sigma_{M_y} + \sigma_{M_z} = \frac{F_a}{A} + \frac{M_y\, z}{I_y} - \frac{M_z\, y}{I_z} \tag{2.38}$$

where σ_{tot}, σ_{F_a}, σ_{M_y} and σ_{M_z} are the stresses due to total stress, axial force, weak axis bending moment, and strong axis bending moment respectively. The stress due to axial force is a function of axial force F_a and the area of the cross-section of the bridge A. The stresses due to weak and strong axis bending moments are functions of weak and strong axis bending moments M_y or M_z, distances from the origin z or y, and the stiffness of the bridge girder cross section I_y and I_z. The arrangement of the cross-sections of the bridge girder can be found in *Figure 1.8* and the structural properties of the bridge girder can be found in *Table 1.5*.

Chapter 3

Results and Discussion

In this chapter, the results of the study are presented including: the environmental conditions modeling, dynamic analysis of vertical response of the floating bridge without viscous effects, wave condition sensitivity study regarding the peak parameter, modeling of viscous damping for a floating bridge, decay tests and the various damping contributions, and finally analysis of global dynamic responses of the floating bridge with viscous effects.

3.1 Environmental Conditions for Simulations

In order to evaluate and analyze the global dynamic responses of the floating bridge, defining the most probable and severe environmental conditions is important. Based on the field measurements, numerical simulations and estimates for the environmental conditions in Bjørnafjorden, 100-year wave due to the local wind, 100-year swell and 100-year wind conditions are defined and summarized in *Table 1.2, 1.3*, and 1.4.

3.1.1 Wave Condition

The most probable 100-year wave condition due to the local wind is with the significant wave height of 2.4 m and the wave period of 5.9 s coming from 270 °, from the west to the east. The most severe wave height is estimated as 2.8 m with the period of 6.6 s. By considering the most probable and the most severe wave conditions, two wave conditions are defined for the simulations. The first wave condition is with the significant wave height of 3 m and the period of 6 s, while the second wave condition is with 2.4 m of the wave height and 5 s of the period. For modeling wind-generated wave spectra, NPRA suggested

the directional spreading of $n = 4$ and the non-dimensional peak parameter in the range of $\gamma = 1.8 - 2.3$. In the simulations, $n = 4$ and $\gamma = 2.3$ are applied.

3.1.2 Swell Condition

The most probable 100-year swell condition is estimated with 0.4 m of the significant wave height and 14 s of the wave period. The most swell is predicted to come from the northwest, however, the waves from the west are expected to be combined with the wind-generated wave and swell [15]. Therefore, in order to have the most severe conditions, the direction of the swell is selected as 270 °, which is the same as the direction of the most probable wind waves. For modeling wave spectra for swell condition, the range of directional spreading $n = 10 - 20$ and the range of non-dimensional peak parameters $\gamma = 3 - 5$ are proposed. $n = 15$ and $\gamma = 5$ are applied in the simulations.

3.1.3 Wind Condition

According to the numerical simulation, the strongest 1-hour mean wind speed with 100 years of return period is estimated as 29.5 m/s at 10 m height from the sea surface. The direction of the wind is also set as 270 °in simulations.

3.1.4 Simulation Conditions

For SIMO-RIFLEX simulations, two sets of environmental conditions are prepared. The first set of conditions summarized in *Table 3.1* is used in conjunction with the numerical model without viscous effect to analyze the influence of the wave conditions on the vertical motion of the floating bridge. The observed heave responses are applied to the modeling of the viscous drag coefficient for heave motion. When large storms with the wind coming from the west, 270 °, it will generate both large wind waves and swell at the bridge location [15]. Therefore, to have realistically severe wave conditions, the combined conditions with both wind-generated wave and swell are included in the first set of conditions.

The second set of conditions in *Table 3.2* is used in simulations with the numerical model including the viscous effect. The simulation is performed to investigate the global dynamic responses of the given floating bridge with viscous effect under the wave, swell, wind and combined conditions.

3.1.5 Wave Spectrum

The wave conditions are generated by using the JONSWAP spectrum with directional function in the SIMO-RIFLEX simulations. *Figure 3.1* illustrates the comparison between

Table 3.1: Environmental conditions for simulations without viscous effect.

		H_s $[m]$	T_p $[s]$	γ [-]	θ_p [°]	n [-]
1	Wave 1	3.0	6.0	2.3	270	4
2	Wave 2	2.4	5.0	2.3	270	4
3	Swell	0.4	14.0	5	270	15
4	Wave 1 + Swell					
5	Wave 2 + Swell					

Table 3.2: Environmental conditions for simulations with viscous effect.

		H_s $[m]$	T_p $[s]$	γ [-]	θ_p [°]	n [-]	U_w [m/s]
1	Wave 1	3.0	6.0	2.3	270	4	
2	Wave 2	2.4	5.0	2.3	270	4	
3	Swell	0.4	14.0	5	270	15	
4	Wind						29.5
5	Still water						
6	Wave 1 + Wind						
7	Wave 2 + Wind						
8	Swell + Wind						

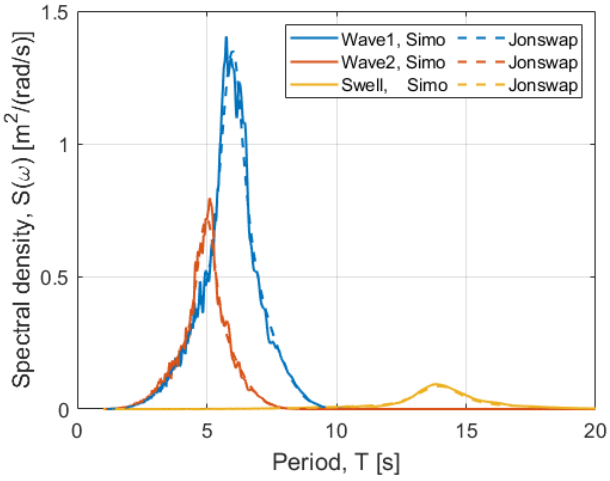

Figure 3.1: Wave spectra comparison between theoretical JONSWAP spectra and simulated spectra in SIMO-RIFELX.

the wave spectra converted from the time series of the wave height measured at pontoons in the simulation, bold line, and the wave spectra theoretically generated, dashed line. It can be clearly seen that the wave conditions are well generated in simulations as intended.

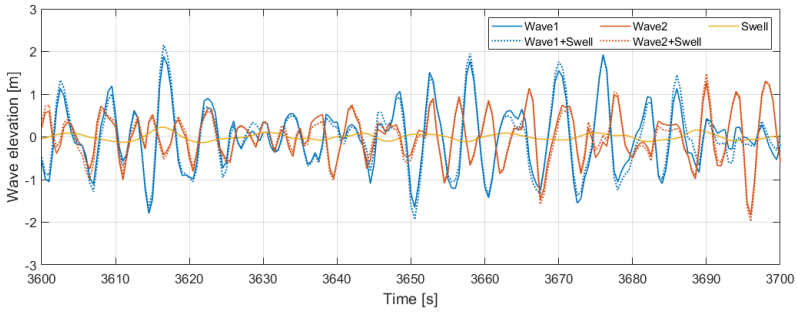

Figure 3.2: Comparison of wave elevations under different wave conditions.

3.1.6 Wave Time Series

The time series of the wave elevations under five different wave conditions are measured at pontoon 10 for comparison. *Figure 3.2* shows the time series of the wave elevations in different wave conditions. As expected the first wave condition has a larger amplitude compared to the second wave and the swell conditions. When the wind-generated waves are combined with the swell, the amplitudes are both slightly increased and decreased depends on the phase angle difference.

Figure 3.3 shows the time series of the wave amplitude in the entire simulation time. Since the simulation runs for 4200 s and the first 600 s is considered a transient time, the results after 600 s are used for the analysis.

3.2 Dynamic Vertical Responses without Viscous Effect

The first numerical simulations in SIMO-RIFELX are performed with the numerical model described in 2.1 without the viscous effects under the selected environmental condition summarized in *Table 3.1*.

The main purpose of this part is to understand the vertical response of the floating bridge without the viscous effect. The obtained heave response is used in modeling of viscous damping on heave motion in the following section. Under the given conditions, the responses in time domain are extracted for analysis. The extracted responses are heave and sway motions, the bending moments about the weak axis and the strong axis however, in this section only the heave motion and the weak axis bending moment are presented. The results of the sway motion and the strong axis bending moment under different wave conditions, and with and without viscous effect can be found in *Appendix A*.

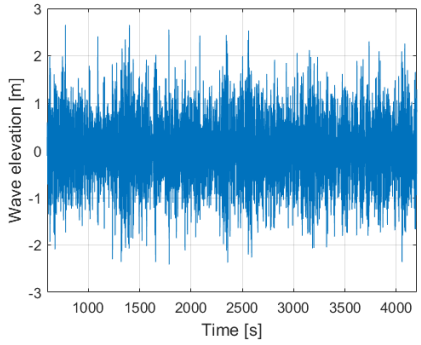

(a) Wave 1: $H_s = 3.0, T_p = 6.0$

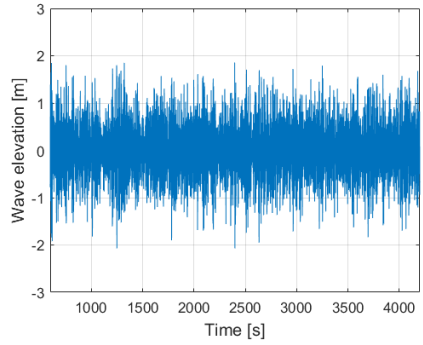

(b) Wave 2: $H_s = 2.4, T_p = 5.0$

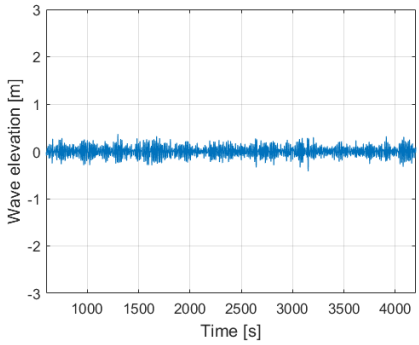

(c) Swell: $H_s = 0.4, T_p = 14$

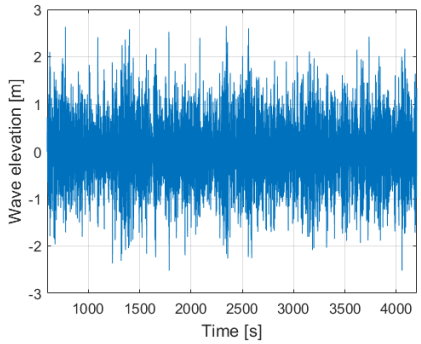

(d) Wave 1 + Swell

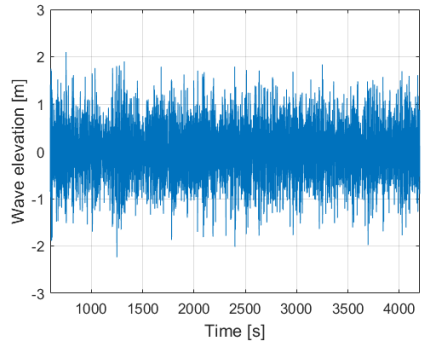

(e) Wave 2 + Swell

Figure 3.3: Time series of wave elevations under different wave conditions.

With the obtained results in time series, the statistical properties of the responses including the standard deviation, maximum, min and mean values are calculated. Spectral density is also obtained to investigate the eigen periods of the responses.

3.2.1 Heave Motion

Statistical Properties

Figure 3.4 shows the statistical properties of the heave motions under different wave conditions. Comparing the results of wave 1 and wave 2, the higher responses are observed in wave 1 condition as expected. Although the significant wave height of the first wave condition is 3 m, the standard deviation of the response is around 0.05 m and the maximum response is only around 0.2 m. The heave response is relatively smaller than expected and this is because of the large structural stiffness about the weak axis.

Since the significant wave height of the swell condition is 0.4 m, the heave response was expected to be the smallest among other wave conditions. However as can be seen in the figures, it shows around the two times larger amplitude compared to the other two wind wave conditions. This can be explained by the wavelength of the given conditions. The wavelengths of wave 1, wave 2, and swell conditions are 56 m, 39 m, and 225 m, respectively. Hence, when wind-generated waves approach the pontoons of the bridge, the pontoons respond rather individually, while several pontoons respond together when the swell comes to the bridge. As a consequence, the largest responses can be observed under the swell or the swell combined conditions.

Spectral Density

In order to investigate the responding period of heave motion under different wave conditions, the spectral density of the heave responses is obtained and compared with the given wave spectra. *Figure 3.5* shows the comparison between wave spectra and heave response spectra of 19 pontoons. The amplitude of the wave spectra is tuned to the maximum amplitude of the response to compare the peaks of spectra. The original scale of comparison can be found in *Figure 3.6*.

As can be seen in *Figure 3.5a* and *3.5b*, the responses are around 8 s which is one of the first vertical eigen periods of the floating bridge. On the other hand, in the swell and the swell combined conditions, *Figure 3.5c*, *3.5d*, and *3.5e*, the pontoons responded at around the swell period of 14 s. The spectra comparisons in original scale in *Figure 3.6* clearly

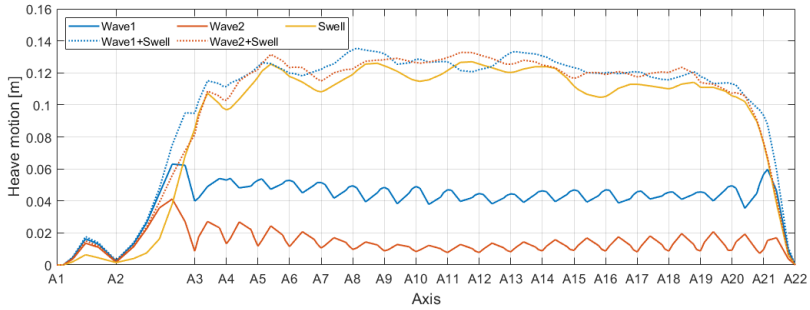

(a) Standard deviation

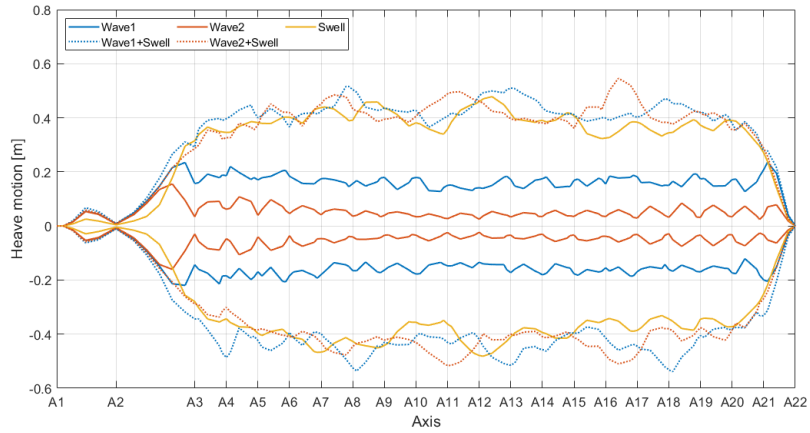

(b) Maximum and minimum

Figure 3.4: Statistical properties of heave motion: (a) Standard deviation and (b) Maximum and minimum under different wave conditions.

shows that the spectra for the heave responses under the wind-generated wave conditions are extremely smaller than the given wave conditions, while the spectra of the responses under the swell and the swell combined conditions are with the almost the same amplitude of the given conditions.

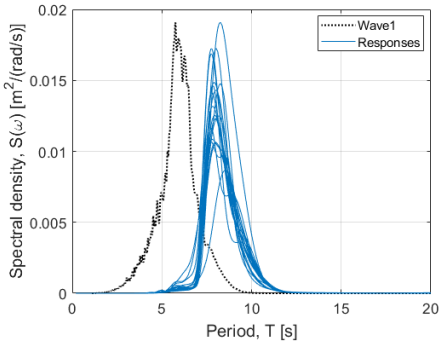

(a) Wave 1: $H_s = 3.0, T_p = 6.0$

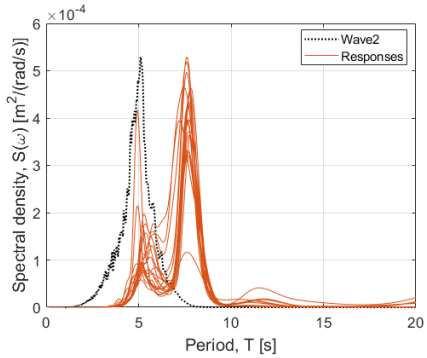

(b) Wave 2: $H_s = 2.4, T_p = 5.0$

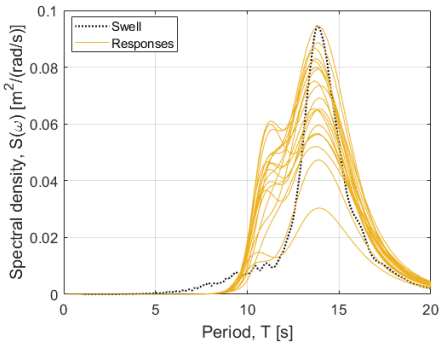

(c) Swell: $H_s = 0.4, T_p = 14$

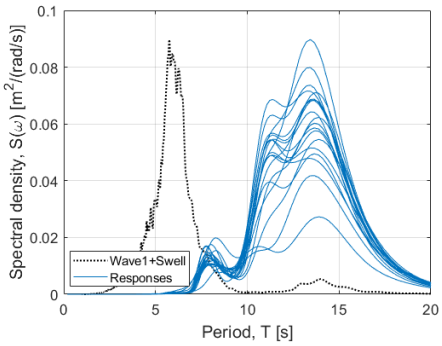

(d) Wave 1 + Swell

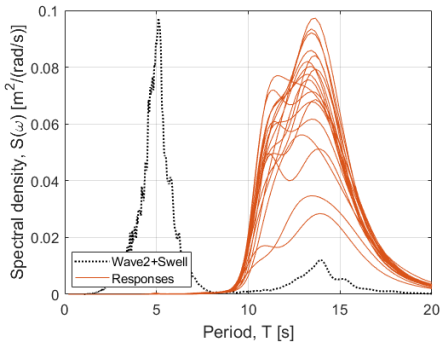

(e) Wave 2 + Swell

Figure 3.5: Comparison of spectral density of wave and heave responses under different wave conditions, the adjusted scale: (a) Wave 1, (b) Wave 2, (c) Swell, (d) Wave 1 + Swell, and (e) Wave 2 + Swell.

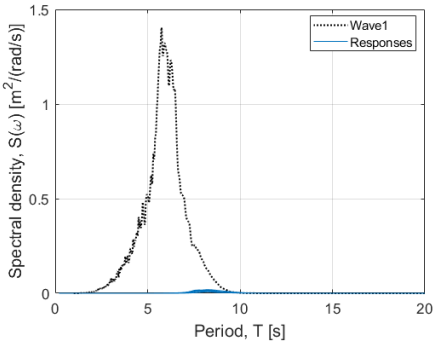

(a) Wave 1: $H_s = 3.0, T_p = 6.0$

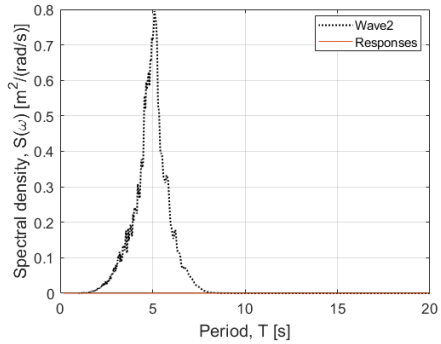

(b) Wave 2: $H_s = 2.4, T_p = 5.0$

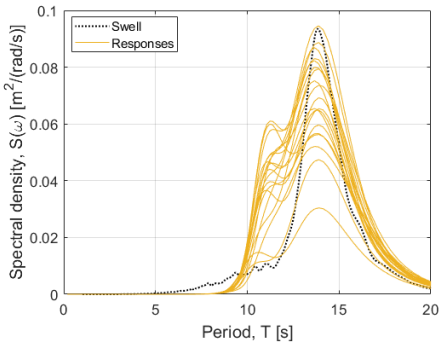

(c) Swell: $H_s = 0.4, T_p = 14$

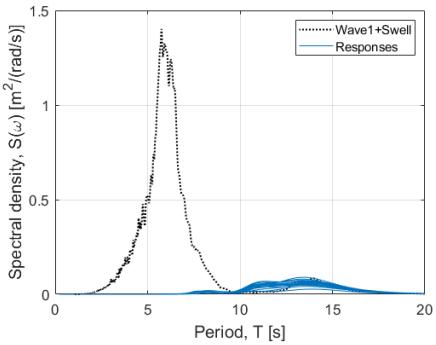

(d) Wave 1 + Swell

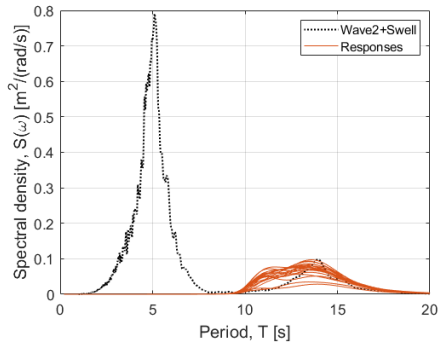

(e) Wave 2 + Swell

Figure 3.6: Comparison of spectral density of wave and heave responses under different wave conditions, the original scale: (a) Wave 1, (b) Wave 2, (c) Swell, (d) Wave 1 + Swell, and (e) Wave 2 + Swell.

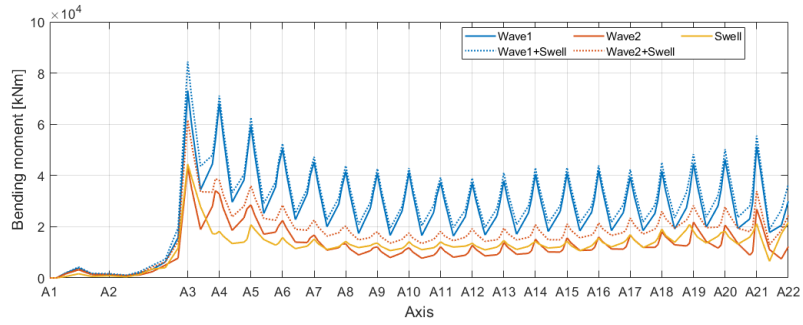

(a) Standard deviation

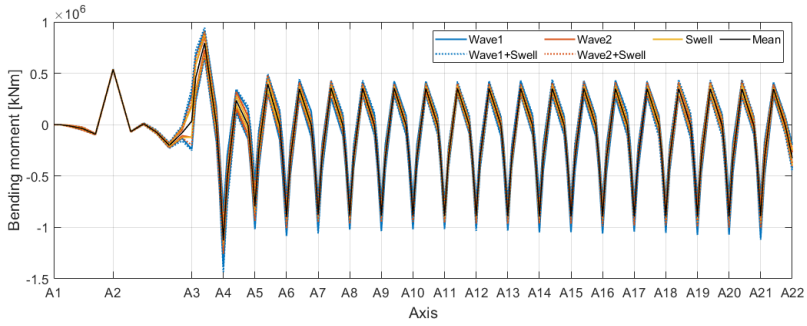

(b) Maximum, minimum and mean

Figure 3.7: Statistical properties of weak axis bending moment: (a) Standard deviation and (b) Maximum, minimum and mean under different wave conditions.

3.2.2 Weak Axis Bending Moment

Figure 3.7 describes the standard deviation and maximum, minimum and mean of the bridge girder bending moment about the weak axis under the different conditions. As can be found in *Figure 3.7a*, large peaks are observed at each pontoon location because of the individual pontoon responses due to waves, e.g. A7 and A9 go up while A8 goes down. However, at the connecting parts, the middle of every adjacent pontoon are only exposed to the bridge weight; therefore, the relatively smaller variations are observed.

Comparing the results with the given wave conditions, the first wave and the first wave combined conditions indicate bigger influence to the weak axis bending moment than the second wave and swell related conditions. High bending moments occur at pontoon locations because wind-generated waves can affect the pontoons in different phases and the pontoons respond in different vertical directions. Therefore, the higher the significant wave height, the bigger the weak axis bending moment.

On the other hand, the swell conditions appeared to be most effective in the heave response, but its effect is weak at the weak axis bending moment. However, it can be seen that the swell still causes a higher standard deviation in the middle of the low bridge section compared to the second wave condition. This is because when the swell is acting on several pontoons at the same time, the whole bridge is raised higher than the wind-generated wave conditions. Therefore, the more global bending moment about the weak axis can be concentrated in the center of the bridge under the swell conditions.

Regarding the maximum, minimum and mean responses as can be seen in *Figure 3.7b*, the positive peaks of the weak axis bending moments are between each pontoon locations, while the negative peaks are at each axis where the pontoons are located. The positive bending moments in the middle of the adjacent pontoons are induced by the bridge weight and the negative moments are induced by buoyancy at the pontoon locations.

Although it can be found that the first wave related conditions show the largest amplitude, the variation is relatively smaller compared to the mean weak axis bending moment. The static and dynamic contributions will be discussed in a further section.

Overall, the bending moment about the weak axis includes the local bending moment and the global bending moment. The local bending moments are mainly influenced by the wind-generated wave and the significant wave height, while the global bending moment is rather related to the wavelength.

3.3 Wave Condition Sensitivity Study on Peak Parameter

During the thesis preparation work in the previous semester, the vertical response of the floating bridge was investigated by using SIMO-RIFLEX simulations. However, the environmental conditions including 100-year wind-generated waves and 100-year swell were defined with different non-dimensional peak parameter of γ. The peak parameters used in the JONSWAP spectrum for generating wave conditions are calculated by using (2.14). The calculated peak parameters are $\gamma = 5$ for wind waves and $\gamma = 1$ for swell conditions, while $\gamma = 2.3$ and $\gamma = 5$ are given for wind waves and swell respectively.

Since the applied environmental conditions in this study used a given peak parameter, it is necessary to study the sensitivity of the wave condition in relation to the peak parameter of γ. In order to understand the influence of the peak parameter on the dynamic responses of the floating bridge, the simulation results with the given peak parameter are compared to the results with the calculated peak parameter. The results with the heave motion and the

weak axis bending moment are presented in this part. The results related to the horizontal responses can be found in *Appendix A*.

3.3.1 Wave Spectra

Figure 3.8 shows wave spectra with different peak parameters. The wave spectra in bold lines are with the given peak parameters, while the spectra in dotted lines are generated by the calculated peak parameters. The peak parameter for wind-generated waves reduced from 5 to 2.3 thus, the height of the spectrum is reduced as well and the width of the spectrum becomes wider. Since the wind-generated wave condition is based on the measurement and the numerical estimates and can be considered as a developing sea state, applying a wider wave spectrum is more realistic. On the other hand, the peak parameter for the swell condition is increased from 1 to 5. This is because the swell condition can be considered as a fully developed sea state; thus, the wave height can be kept stable and the period range can be narrower.

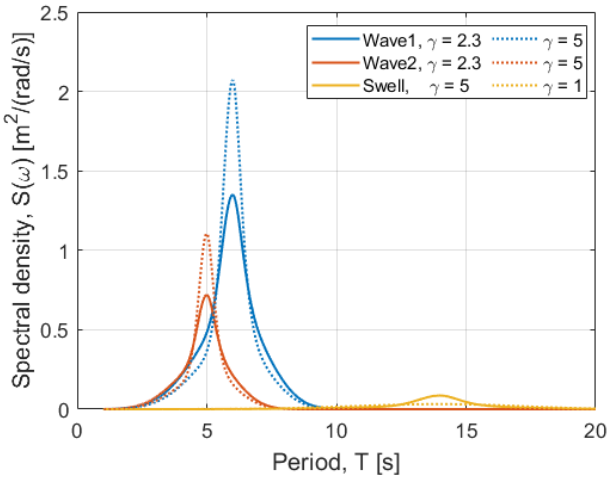

Figure 3.8: Comparison of wave spectra with different peak parameter.

3.3.2 Heave Motion

Figure 3.9 presents the heave responses under waves with different peak parameters. Although the peaks of the spectra for wind-generated wave conditions reduced, the heave response is increased. Since the range of the vertical eigen period is 7.5-10.95 s, when the wave period is widened the number of waves close to the natural period of the bridge increases, thereby increasing the magnitude of the vertical response. On the other hand,

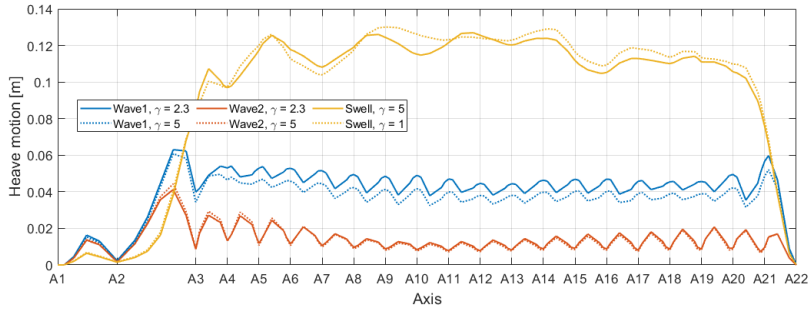

(a) Standard deviation

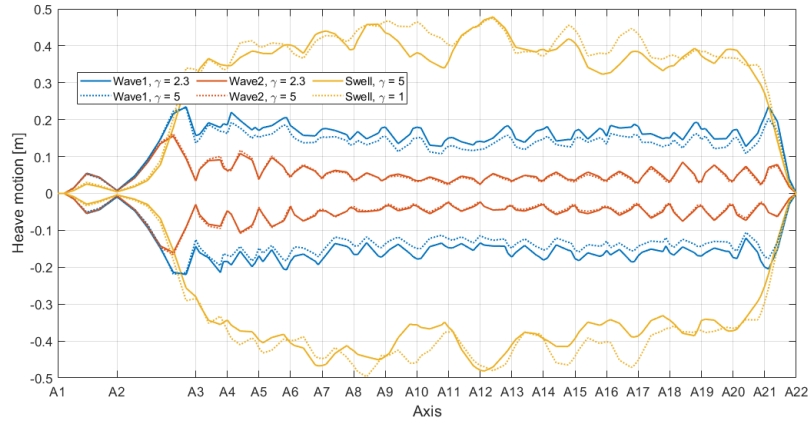

(b) Maximum and minimum

Figure 3.9: Statistical properties of heave motion: (a) Standard deviation and (b) Maximum and minimum under waves with different peak parameters.

in the swell condition, since the wave spectrum becomes narrower, the number of waves close to the natural period decreases; thus, the amplitude of the heave response decreases.

3.3.3 Weak Axis Bending Moment

Regarding the peak parameter effect on the weak axis bending moment illustrated in *Figure 3.10*, the differences are the same as the heave responses. Since the peak parameter for the wind-generated wave conditions are given as $\gamma = 2.3$, while the calculated value is $\gamma = 5$, the more wave energy cause the vertical responses with the smaller peak parameter conditions. Thus, the wave conditions with $\gamma = 2.3$ show a larger weak axis bending moment than the conditions with $\gamma = 5$. On the other hand in swell conditions, the given parameter is $\gamma = 5$, hence the response is smaller than the swell with the calculated $\gamma = 1$.

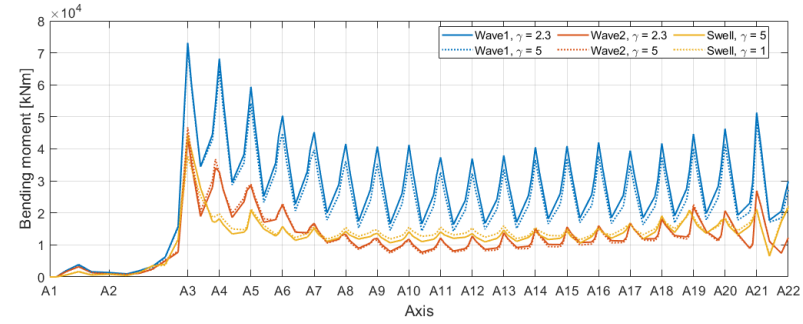

(a) Standard deviation

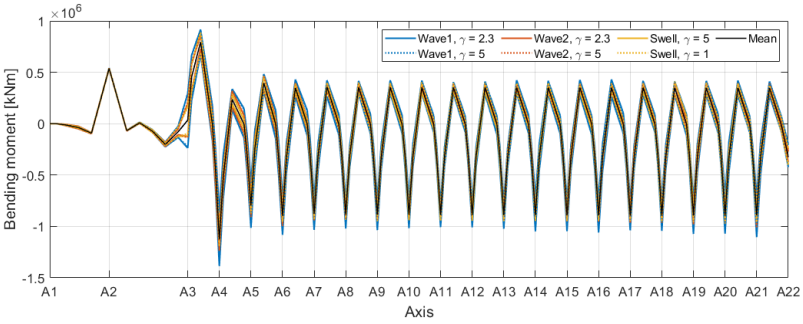

(b) Maximum, minimum and mean

Figure 3.10: Statistical properties of weak axis bending moment: (a) Standard deviation and (b) Maximum, minimum and mean under waves with different peak parameters.

3.4 Viscous Damping Modeling

The viscous drag force for the numerical model is estimated by using the Morison's equation (2.20) as described in 2.3.3. The drag coefficient is the key parameter for estimating the viscous effect, however, when empirical suggestions for a floating pontoon with a flange in fjord were not available, the conventional drag coefficient was applied. Cheng et al. used $C_{dz} = 2$ [3] for estimating drag force in z-axis for a floating bridge. With the help of the experiment and analysis performed by Shao et el. [14], KC dependent drag coefficient is suggested for modeling the viscous drag force of heave motion for a pontoon in a floating bridge.

3.4.1 KC Number

KC number can be defined with the relative heave amplitude and the flange width as the characteristic length. The considered design of the pontoon as described in *Figure 1.9* has a flange with a width of $F = 5m$. From the previous numerical simulations, the heave responses are observed between 0.2 to 0.5 m. Shao et el. [14] used 0.3 and 0.6 as the relative heave amplitude. In this study, the relative heave amplitudes of 0.2, 0.3 and 0.5 are applied for KC number calculation. The obtained KC numbers are 0.2513, 0.3770 and 0.6283.

3.4.2 Drag Coefficient

KC number dependent drag coefficient can be obtained by using (2.22). *Figure 3.11* describes the relationship between the KC number and the corresponding drag coefficient for the give floating pontoon with the flange in heave motion. The blue line represents the drag coefficient considering the total contribution from the entire bottom plate area including the flange area, while the red line corresponds to the contribution from the flange area only. KC dependant drag coefficients $C_{dz,kc}$ are calculated as 25.91, 23.98 and 21.56 for heave amplitudes of 0.2 m, 0.3 m and 0.5 m respectively.

As can be seen in *Figure 3.11*, the drag coefficient varies between 21 to 26. These numbers seem much bigger than the values used in other studies, however, in drag force calculation the drag coefficient $C_{dz,kc}$ suggested above should be considered with the area of the flange that is of 918.36 m^2 in the given design. Since the obtained drag coefficient can be used with the area of the flange, an appropriate adjustment (2.26) can be applied to have a conventional drag coefficient C_{dz} that can be used for drag force calculation (2.20) with the area of the entire bottom plate. The total bottom plate area is 2654.11 m^2 for the given design. After the modification, the adjusted equivalent drag coefficients which can

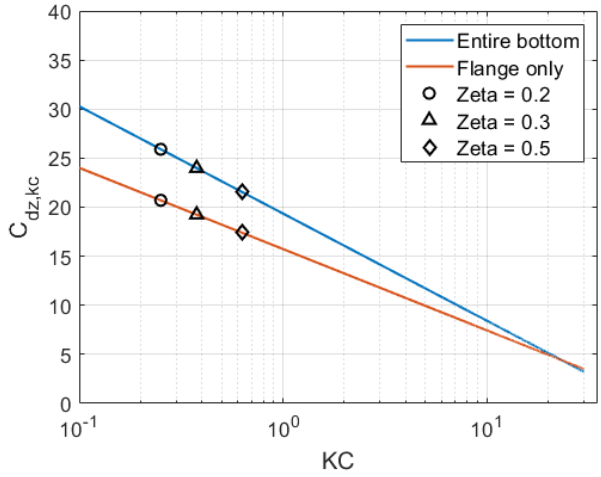

Figure 3.11: KC dependent drag coefficients for contributions of the flange area only and the entire bottom plate area of the pontoon, can be used with the flange area.

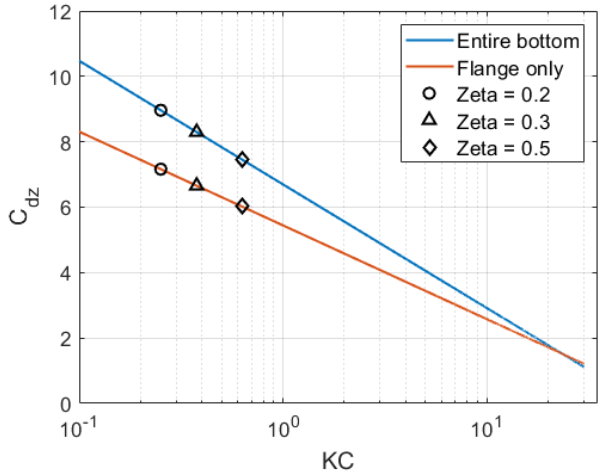

Figure 3.12: Adjusted KC dependent drag coefficients for contributions of the flange area only and the entire bottom plate area of the pontoon, can be used with the bottom plate area.

be used with the entire bottom area are obtained as 8.96, 8.30 and 7.46. *Figure 3.12* shows the equivalent drag coefficient as a function of KC number and *Table 3.3* summarizes the drag coefficient modeling results.

In this paper, the KC dependent drag coefficient is used. Since KC number varies in time,

Table 3.3: KC dependant and equivalent drag coefficients in z-axis as function of relative heave amplitude and corresponding hydrodynamic properties.

Heave amplitude, ζ_a $[m]$	0.2	0.3	0.5
KC number	0.2513	0.3770	0.6283
$C_{dz,kc,flange}$	20.70	19.24	17.40
$C_{dz,kc,bottom}$	25.91	23.98	21.56
$C_{dz,flange}$	7.16	6.66	6.02
$C_{dz,bottom}$	8.96	8.30	7.46
Quadratic drag $[Ns^2/m^3]$	1.5632 E+05	1.4471 E+05	1.3009 E+05
Quadratic damping $[Ns^2/m^2]$	1.2193 E+07	1.1287 E+07	1.0147 E+07

the drag coefficient also varies in time. However, for the further simulations including viscous effect in this study, the constant heave amplitude of $\zeta_a = 0.3\ m$ is considered and the corresponding drag coefficient for heave response of $C_{dz,kc} = 23.98$ that is equivalent to $C_{dz} = 8.3$ is applied as a constant drag coefficient. Regarding drag coefficients for surge and sway responses, $C_{dx} = 1.7$ and $C_{dy} = 0.7$ are applied as per the DNV recommendation [7].

During this study, Robert Read, a senior researcher at DTU obtained the numerically calculated constant drag coefficient that is independent to time for the given pontoon design with the flange. Additional SIMO-RIFLEX simulations were performed by the author with the same environmental conditions prepared in *Table 3.1*, but without directional features in wave generation by the JONSWAP spectrum. Based on the wave conditions and heave responses, KC number in time series was obtained and the total energy dissipated due to viscous damping throughout the time series is calculated. An equivalent constant drag coefficient for each combination of the pontoon and the wave condition, that would have the same energy dissipation over the entire time series is derived. *Table 3.4* summarized the mean and the standard deviation of the equivalent drag coefficients in different conditions obtained from the first and second iterations.

In wind-generated wave conditions, the mean values of the equivalent constant drag coefficients from the time series are close to the calculated KC dependent drag coefficient summarized in *Table 3.3*. Therefore, the applied KC dependent drag coefficient of 23.98 in this study can be considered as a reasonable value.

3.4.3 Quadratic Drag and Damping

In SIMO, the viscous effect can be applied as quadratic damping, (2.27) or quadratic drag, (2.28). *Table 3.5* summarized the drag coefficient and the corresponding quadratic damp-

Table 3.4: Mean and standard deviation of equivalent constant drag coefficient $C_{dz,kc}$ obtained by time series numerical iterations.

		1st iteration		2nd iteration	
		Mean	Std.	Mean	Std.
1	Wave 1	23.55	0.198	23.51	0.189
2	Wave 2	26.17	0.232	26.16	0.234
3	Swell	27.05	1.638	27.66	1.739
4	Wave 1 + Swell	23.54	0.201	23.68	0.093
5	Wave 2 + Swell	25.89	0.584	26.29	0.331

Table 3.5: Drag coefficient, quadratic drag and quadratic damping for x-, y-, and z-axis.

	x	y	z
C_d	1.7	0.7	8.3
Q_{damp} $[Ns^2/m^2]$	5.9245 E+05	1.0045 E+05	1.1287 E+07
Q_{drag} $[Ns^2/m^3]$			1.4471 E+05

ing for x-, y-, and z-axis applied in further simulations. The quadratic drag is only applied to z-axis to compare the difference between effects due to the quadratic drag and quadratic damping.

3.5 Viscous Effect on Vertical Response

After modeling the viscous terms, SIMO-RIFLEX simulations were performed to investigate the viscous effects on the vertical responses. The spectral density of heave responses under the different wave conditions with and without viscous effects are compared. The standard deviation and the maximum magnitude of the responses including heave and weak axis bending moment are discussed. Maximum magnitude is chosen as the largest absolute amplitude among the minimum and the maximum values. The viscous effect on the horizontal responses can be found in *Appendix A*.

3.5.1 Spectral Density Comparison

Figure 3.13 shows the comparison of the spectral density of heave motion of pontoon 10 at A12 with different viscous effects. The bold line indicates the response without viscous effect, the dashed line indicates the response with the quadratic drag, and the dotted line represents the response with the quadratic damping. Depends on the phase angle difference, the response with the quadratic drag can be both larger and smaller than the response without viscous effect. However, the response with the quadratic damping is clearly smaller than response without viscous terms.

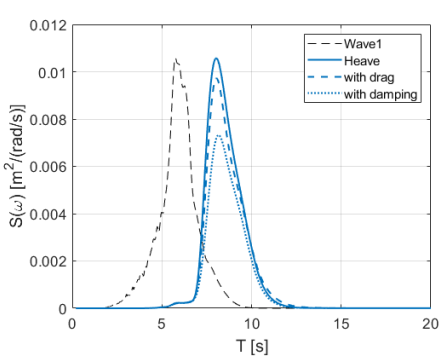

(a) Wave 1

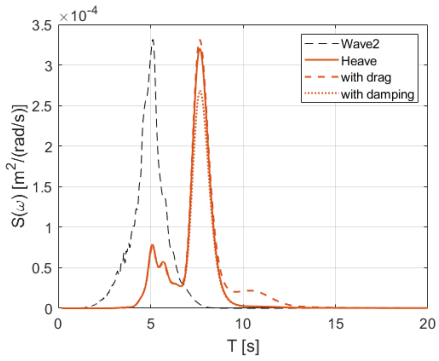

(b) Wave 2

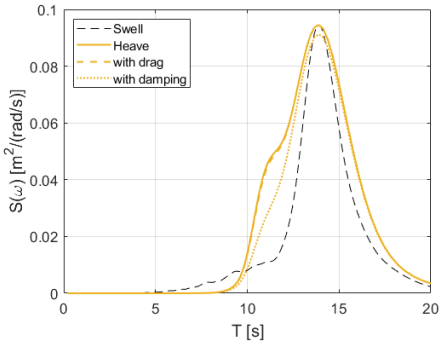

(c) Swell

Figure 3.13: Comparison of spectral density for heave motion of pontoon 10 at A12 in different wave conditions with and without viscous effect.

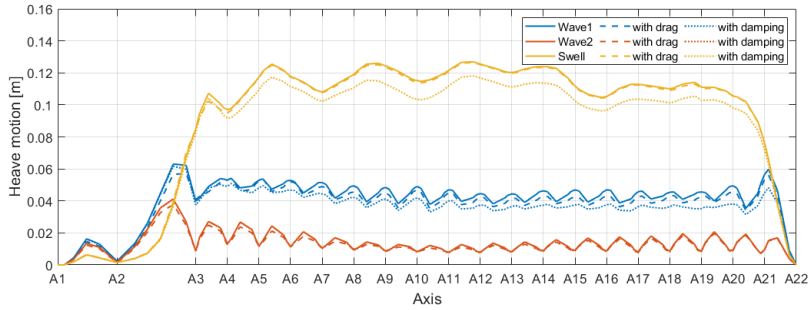

(a) Standard deviation

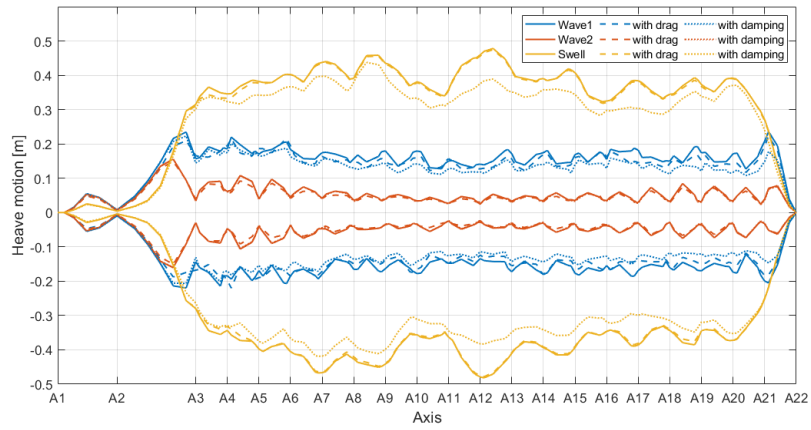

(b) Maximum and minimum

Figure 3.14: (a) Standard deviation, and (b) Maximum and minimum of heave motion with and without viscous effect.

3.5.2 Heave Motion Comparison

As can be seen in *Figure 3.14*, the standard deviation, maximum and the minimum heave motions have the largest values when there is no viscosity effect and the smallest values when the quadratic viscosity damping is applied. The responses with the quadratic drag are generally smaller than the response without viscous effect and the response with the quadratic damping is always smaller than the response without viscous effect. After applying the viscous term, as can be found in *Figure 3.14a*, the standard deviation of the heave response decreased by only 0.01 m in the swell condition and decreased to less than 0.01 m in the other wave conditions. In the maximum and minimum heave response, *Figure 3.14b*, the response reduced maximum 0.1 m under the swell condition and decreased less than 0.1 m in the other conditions.

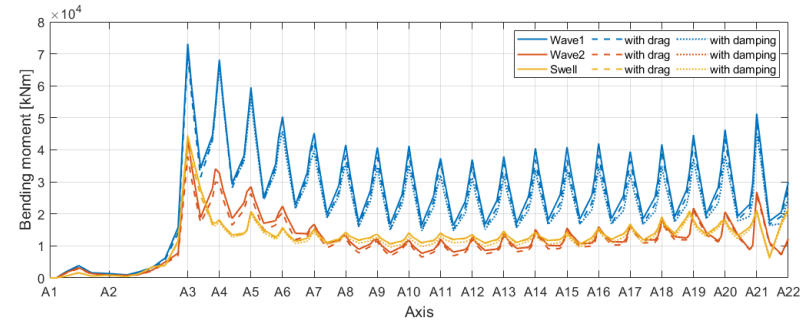

(a) Standard deviation

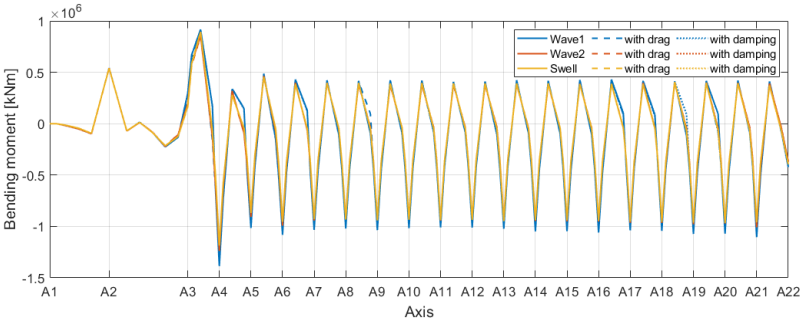

(b) Maximum magnitude

Figure 3.15: (a) Standard deviation, and (b) Maximum magnitude of the weak axis bending moment with and without viscous effect.

3.5.3 Weak Axis Bending Moment Comparison

The standard deviation of the weak axis bending moment illustrated in *Figure 3.15a* is slightly reduced at the low floating bridge area after applying the viscous terms. At A16, the standard deviation of the weak axis bending moment is around 42 MPa without viscous effect, around 38 MPa with the quadratic drag, and around 35 MPa with the quadratic damping. Although the viscous terms influence to reduce the weak axis bending moment variation, the effects are relatively small compared to the overall values.

Regarding the maximum magnitude of the weak axis bending moment depicted in *Figure 3.15b*, it is difficult to distinguish the difference between wave conditions and viscous effect. The viscous effect reduced the amplitude of the response at A16 from 1060 MPa without viscous to 1055 MPa with the quadratic drag, and to 1045 MPa with the quadratic damping. However, only 15 MPa reduced from 1060 MPa thus, the viscous effect is not noticeable.

3.6 Free Decay Test

In order to understand the contribution of different sources of the damping, free decay tests were performed. Since the given floating bridge has complex resonant responses due to 19 pontoons and long length without mooring, generating only one mode shape in free decay test is difficult. 3 different loading conditions for each vertical and horizontal decay tests were prepared to generate responses close to the identified mode shapes. First, the force derivative of 100 kN is loaded on selected pontoons with a designated direction for 100 s, then the constant force of 10 MN is loaded for another 100 s to reduce transient responses. Each decay test was performed with two simulations with and without quadratic viscous damping. From each decay test, natural period and damping ratio of the flexible bridge girder were retrieved for analysis.

3.6.1 Vertical Decay Test 1

The first vertical decay test was performed to create the vertical mode shape with the longest eigen period described in *Figure 1.12a*. The artificial load was applied on A12 at the +z direction and released as depicted in *Figure 3.16a*. After released the load, the force is transmitted from A12 to each side, reflected at the ends, and returned back as can be seen in *Figure 3.16b*. Since the bridge girder is a flexible structure, it is limited to generate the same mode shape by an artificial load.

As can be seen in *Figure 3.17*, several responding periods can be observed in both time history and the spectral density, however, by focusing on the peaks on time history between 200 s to 300 s, the dominant eigen period can be obtained by using (2.30). The damping ratio is obtained by (2.31) and the critical damping and total damping are obtained with (2.33) and (2.34). The potential damping is obtained from the hydrodynamic properties from Wadam described in *Figure 1.15*. The structural damping can be theoretically calculated by using (2.35) and (2.36). However, since the structural damping depends on the bridge girder response, the structural damping is obtained by subtracting the potential damping from the total damping. The contribution of the viscous effect is obtained as linearized viscous damping by subtracting potential and structural damping from the total damping.

Table 3.6 summarizes the findings of the first vertical free decay test. In a vertical decay test, it is expected to capture the eigen period between 7.5 s to 10.95 s that observed in the numerical simulations. The eigen period of with and without quadratic viscous damping are 10.91 s and 10.93 s thus, it can be considered that the first free decay test well reflected one of the vertical mode shapes.

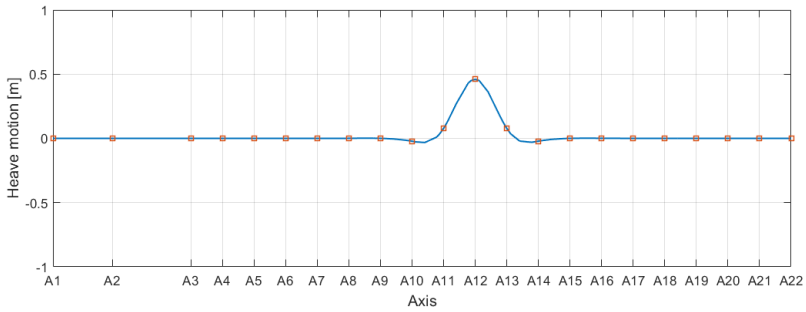

(a) Vertical decay test1, t = 200 s

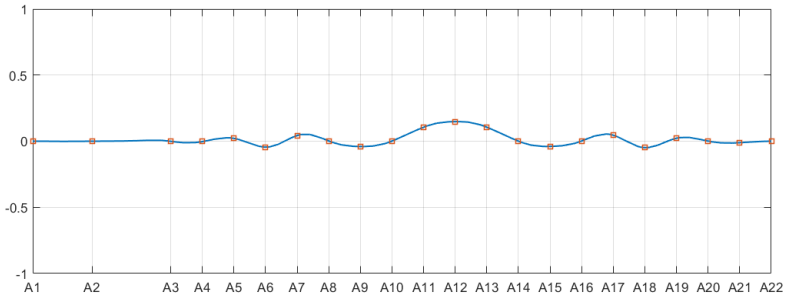

(b) Vertical decay test 1, t = 232.6 s

Figure 3.16: Vertical decay test 1: (+z) forces on A12.

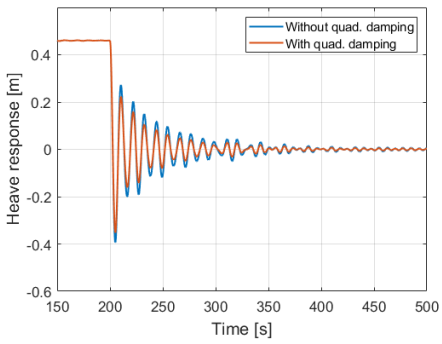

(a) Time history of vertical decay test 1

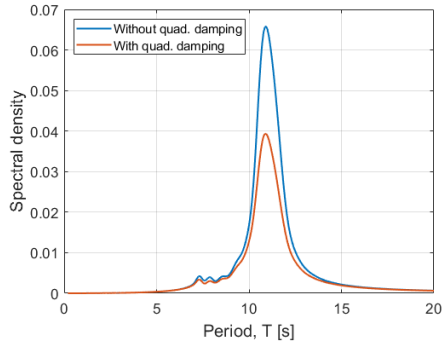

(b) Spectral density of vertical decay test 1

Figure 3.17: Time history and spectral density of vertical decay test 1, (+z) force on A12.

Table 3.6: Result of vertical decay test 1 for A12.

			without quad. damp	with quad. damp
Natural period	T_n	$[s]$	10.93	10.91
Natural frequency	ω_n	$[rad/s]$	0.575	0.576
Damping ratio	λ	$[\%]$	5.35	6.81
Critical damping	B_{cr}	$[Ns/m]$	6.261 E+07	6.273 E+07
Total damping	B_{tot}	$[Ns/m]$	3.352 E+06	4.273 E+06
Potential damping	B_{pot}	$[Ns/m]$	1.975 E+06	1.964 E+06
Structural damping	B_{str}	$[Ns/m]$	1.377 E+06	1.377 E+06
Lin. viscous damping	B_{vis}	$[Ns/m]$		9.327 E+05
Potential damping ratio	B_{pot}/B_{cr}	$[\%]$	3.15	3.13
Structural damping ratio	B_{pot}/B_{cr}	$[\%]$	2.20	2.19
Lin. viscous damping ratio	B_{pot}/B_{cr}	$[\%]$		1.49

The total, potential and structural damping ratio without viscous damping are 5.35 %, 3.15 %, and 2.20 % respectively. When the quadratic damping is applied to the numerical model, the total damping is increased to 6.81 %. The potential, structural and the linearized viscous damping ratio are observed as 3.13 %, 2.19 % and 1.49 % respectively. Compared to previous studies, a larger drag coefficient of $C_{dz} = 8.3$ is used for the heave motion, and the corresponding quadratic damping is applied to the simulation. However, the contribution of the viscous damping is found as the smallest due to the small heave response of the bridge girder.

3.6.2 Vertical Decay Test 2

The second vertical decay test was performed to generate the vertical mode shape with the shortest eigen period described in *Figure 1.12b*. The positive artificial forces are loaded on A10, A12, and A14, and negative forces are loaded on A11 and A13 as presented in *Figure 3.18a*. After released the loads, the bridge reacted in a mode shape as can be seen in *Figure 3.18b*.

Figure 3.19 presents the time history of vertical motions of the selected pontoons and *Figure 3.20* illustrates the spectral density of the vertical responses in period. From the peaks of the spectra, eigen periods in other vertical mode shapes are captured as summarized in *Table 3.7*. Due to the complexity of the mixed mode shapes in the time history, the natural periods of 7.55 s, 7.59 s, 7.62 s and 10.85 s are extracted.

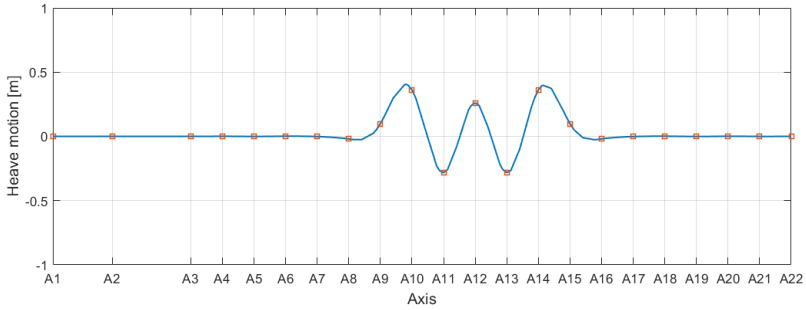

(a) Vertical decay test 2, t = 200 s

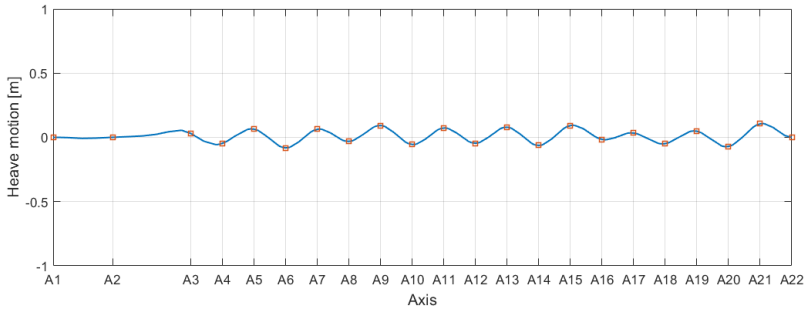

(b) Vertical decay test 2, t = 256.8 s

Figure 3.18: Vertical decay test 2: (+z) forces on A10, A12 and A14, and (-z) forces on A11 and A13.

Table 3.7: Result of Vertical decay test 2.

	T_n $[s]$	ω_n $[rad/s]$
A10	7.55, 10.85	0.579, 0.832
A11	7.62	0.824
A12	7.62	0.824
A13	7.62	0.824
A14	7.59, 10.85	0.579, 0.828

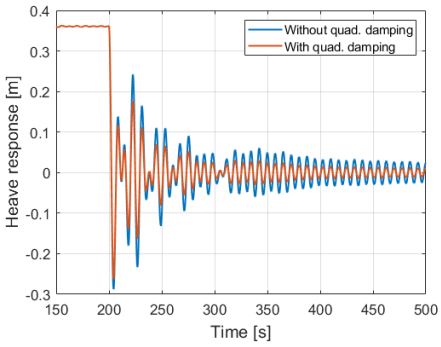

(a) A10

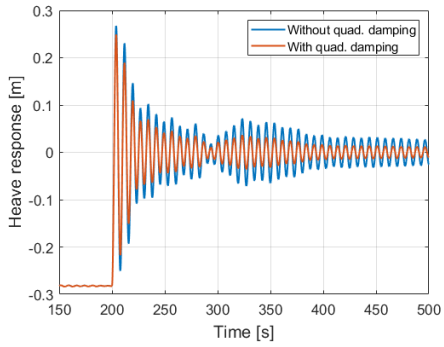

(b) A11

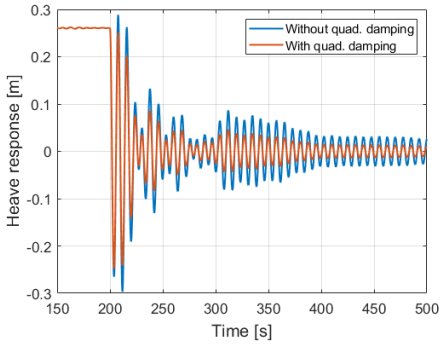

(c) A12

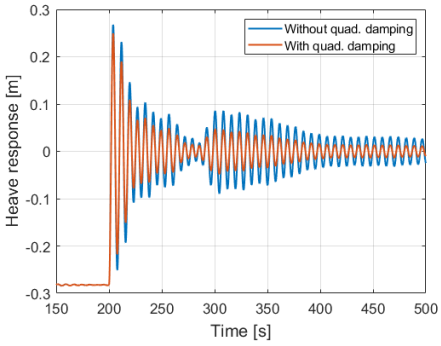

(d) A13

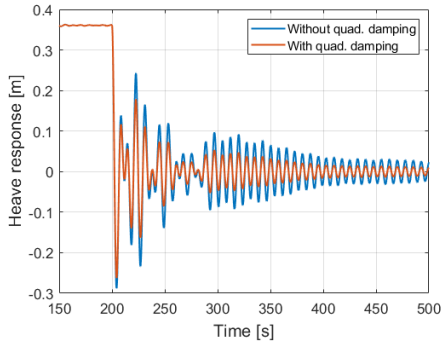

(e) A14

Figure 3.19: Time history of vertical decay test 2.

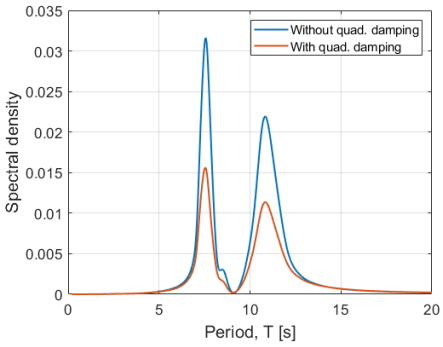

(a) A10

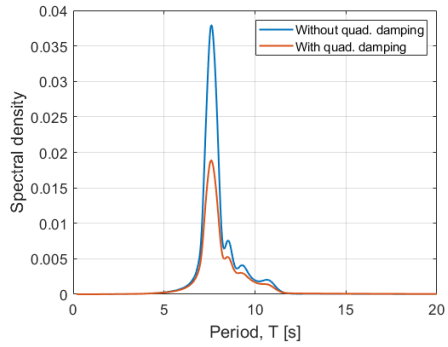

(b) A11

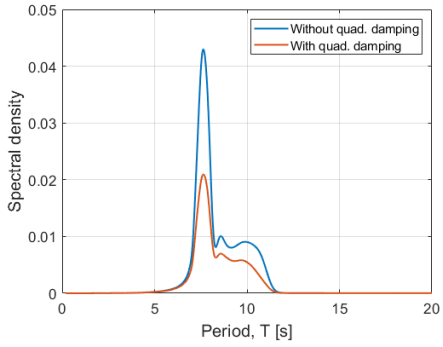

(c) A12

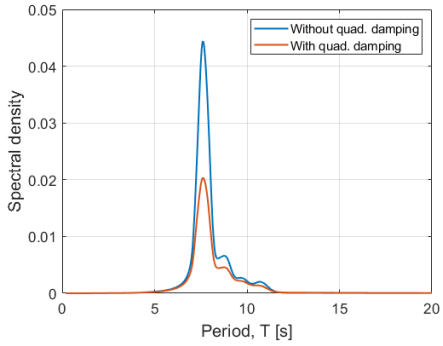

(d) A13

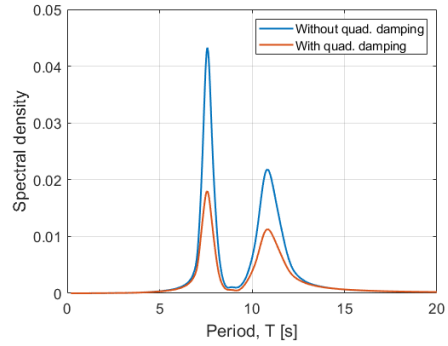

(e) A14

Figure 3.20: Spectral density of vertical decay test 2.

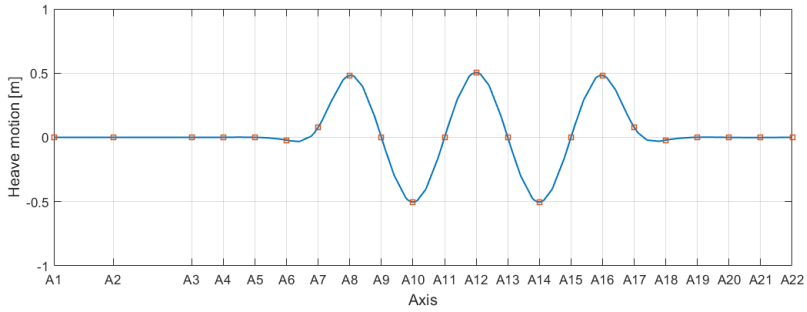

(a) Vertical decay test 3, t = 200 s

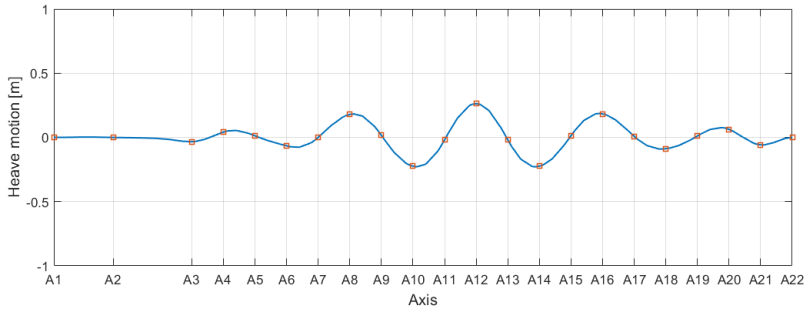

(b) Vertical decay test 3, t = 231.0 s

Figure 3.21: Vertical decay test 3: (+z) forces on A8, A12 and A16, and (-z) forces on A10 and A14.

3.6.3 Vertical Decay Test 3

In the last vertical decay test, the positive forces are loaded on A8, A12 and A16, while the negative forces are loaded on A10 and A14, *Figure 3.21a*. After released the loads, the shape of the bridge response remains as the same as the initial loading conditions in some time as can be found in *Figure 3.21b*, however the shape of response changes later over time.

As can be seen in *Figure 3.22* and *3.23*, various types of vertical responses are observed in different pontoons. The pontoons with initial loads responded mainly with one period, but the pontoons between them showed mixed responding periods. Therefore, there are multiple peaks in the spectra of the responses. Various eigen periods are captured as summarized in *Table 3.8*. By looking at the time history and the observed eigen periods, it can be easily identified that the complexity of the vertical mode shapes of the floating bridge.

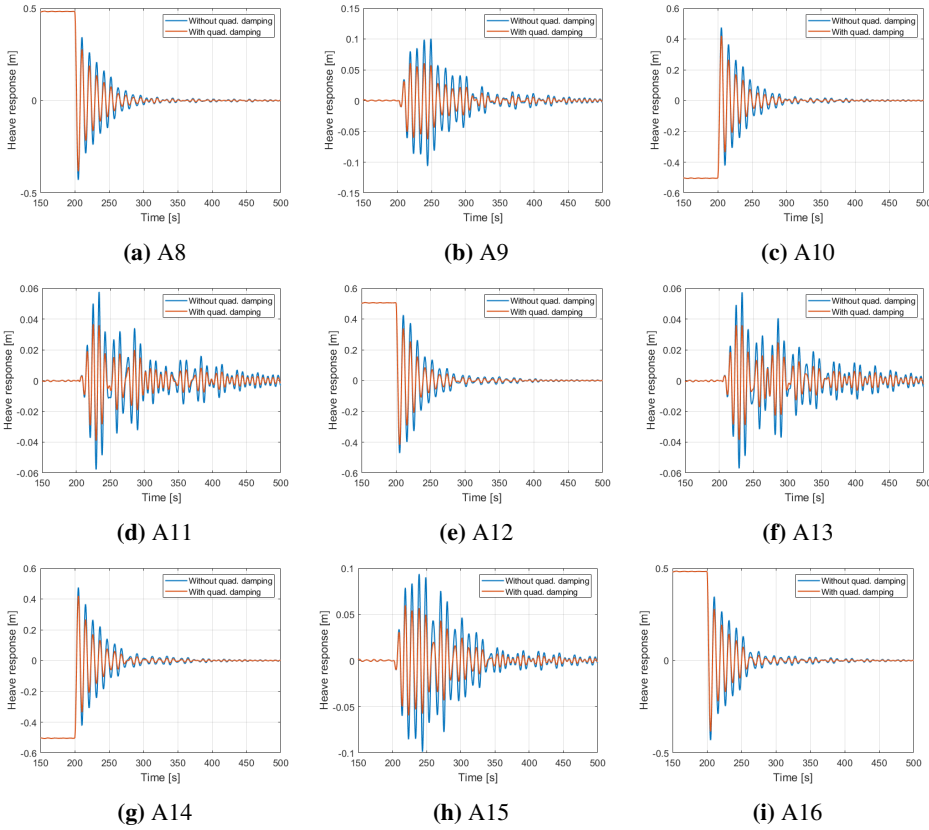

(a) A8 **(b)** A9 **(c)** A10

(d) A11 **(e)** A12 **(f)** A13

(g) A14 **(h)** A15 **(i)** A16

Figure 3.22: Time history of vertical decay test 3.

Table 3.8: Result of vertical decay test 3.

	$T_n\ [s]$	$\omega_n\ [rad/s]$
A8	10.64	0.591
A9	10.44	0.602
A10	10.64	0.591
A11	7.59, 8.58, 9.81, 10.64	0.591, 0.640, 0.732, 0.828
A12	10.71	0.587
A13	7.62, 9.05, 10.24	0.614, 0.694, 0.824
A14	10.71	0.587
A15	10.31	0.610
A16	10.71	0.587

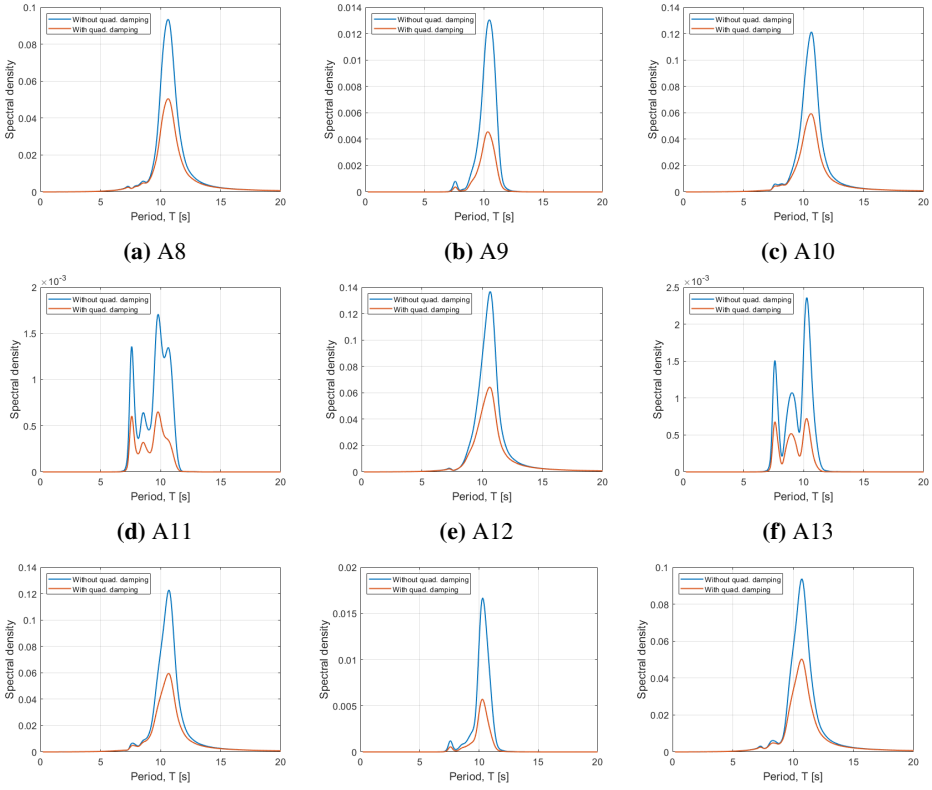

(a) A8 **(b)** A9 **(c)** A10

(d) A11 **(e)** A12 **(f)** A13

(g) A14 **(h)** A15 **(i)** A16

Figure 3.23: Spectral density of vertical decay test 3.

Table 3.9: Result of horizontal decay test 1 at A6.

			without quad. damp	with quad. damp
Natural period	T_n	$[s]$	62.16	62.16
Natural frequency	ω_n	$[rad/s]$	0.101	0.101
Damping ratio	λ	$[\%]$	0.50	0.97
Critical damping	B_{cr}	$[Ns/m]$	4.829 E+06	4.829 E+06
Total damping	B_{tot}	$[Ns/m]$	2.415 E+04	4.273 E+06
Potential damping	B_{pot}	$[Ns/m]$	48.97	48.97
Structural damping	B_{str}	$[Ns/m]$	2.410 E+04	2.41 E+04
Lin. viscous damping	B_{vis}	$[Ns/m]$		9.327 E+05
Potential damping ratio	B_{pot}/B_{cr}	$[\%]$	0.00	0.00
Structural damping ratio	B_{pot}/B_{cr}	$[\%]$	0.50	0.50
Lin. viscous damping ratio	B_{pot}/B_{cr}	$[\%]$		0.47

3.6.4 Horizontal Decay Test 1

3 different horizontal free decay tests were performed to investigate horizontal mode shapes, the eigen periods as well as various damping contributions. The first horizontal decay test was performed to create the first horizontal eigen mode shape described in *Figure 1.13a*. The initial loading condition is presented in *Figure 3.24*. The positive force is applied on A7 in the y-direction, while the minus force is applied on A16 and released. Compared to the vertical decay test, the mode shape is well generated by the initial loading conditions and kept the same shape over time as can be seen in *Figure 3.24b*.

Figure 3.25 and *3.26* present the time history and the spectral density of the sway responses at the selected pontoons. *Table 3.9* summarized the result of the first horizontal free decay test for the pontoon at A6. The natural periods of the sway responses of the bridge with and without viscous effect are both 62.16 s. The obtained natural period is slightly larger than the natural period of 56.72 s captured in the numerical simulation and the error is approximately 9.6 %.

The total damping without viscous effect contains the potential and the structural damping however, the potential damping is close to zero. Therefore, the structural damping ratio is almost the same as the total damping of 0.5 %. Since there is no mooring system in the given design and the pontoons move with a smaller phase angle difference, the structural damping in the y-direction is much smaller than z-direction. After including the quadratic viscous damping, the total damping ratio becomes 0.97 % and the linearized viscous damping ratio is 0.47 %. Because of the smaller damping effect on the sway motion, it takes much longer time than the heave decay until the response dies out.

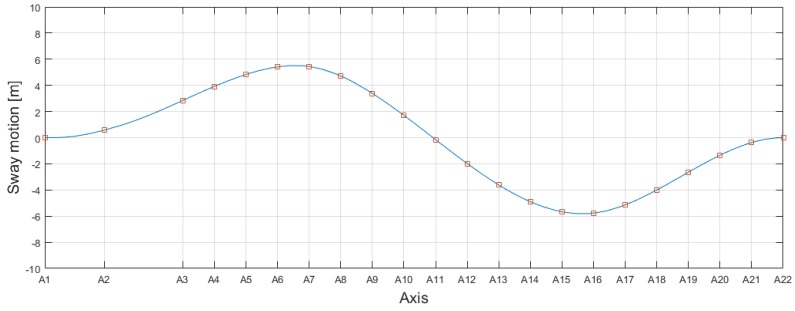

(a) Horizontal decay test 1, t = 200 s

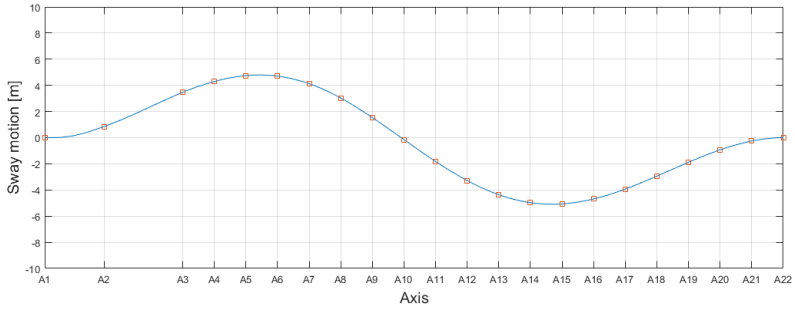

(b) Horizontal decay test 1, t = 322.8 s

Figure 3.24: Horizontal decay test 1: (+y) force on A7, and (-y) force on A16.

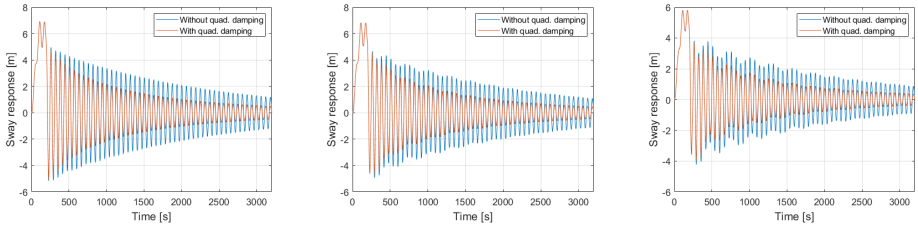

(a) A6 **(b)** A7 **(c)** A8

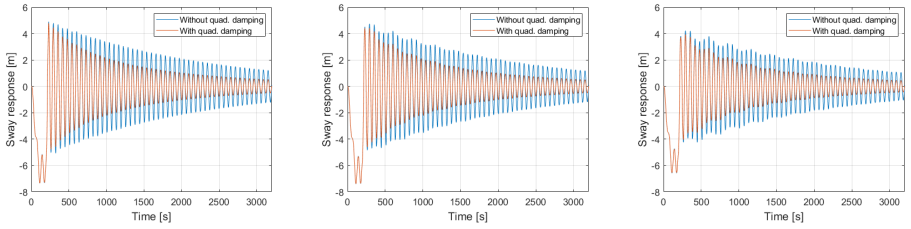

(d) A15 **(e)** A16 **(f)** A17

Figure 3.25: Time history of horizontal decay test 1.

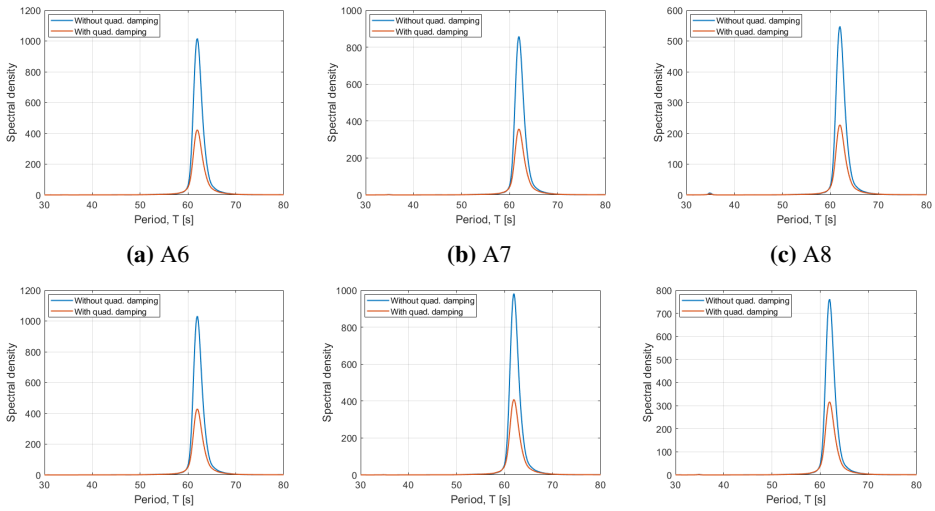

(a) A6 **(b)** A7 **(c)** A8

(d) A15 **(e)** A16 **(f)** A17

Figure 3.26: Spectral density of horizontal decay test 1.

3.6.5 Horizontal Decay Test 2

In the second horizontal decay test, the positive force in y-direction is applied to A11 as presented in *Figure 3.27a* to create the second sway mode shape as shown in *Figure 1.13b*. After released the loading condition, the peak of the responding bridge shape slightly moves to A10 but remains in the same mode shape. As can be seen in *Figure 3.28* and *3.29* for the time history and the spectra, two different mode shapes are mixed in the responses. The data measured at A11 is used for eigen period and damping ratio calculation and summarized in *Table 3.10*.

The observed natural periods are 34.91 s and 61.98 s in both cases with and without viscous effect. The damping ratio is calculated with the dominant eigen period of 34.91 s which is close to the second eigen period of 31.69 s from the numerical simulation. The error is approximately 10 %. The eigen period of 61.98 s is close to the first eigen period captured during the first horizontal decay test. As discussed before, due to the flexible bridge girder, generating only one mode shape is difficult. The total damping without the viscous effect is 0.85 % mainly due to the structural damping of 0.84 %. The viscous contribution is found as 0.13 % thus, the viscous effect is very small in the second mode shape as well.

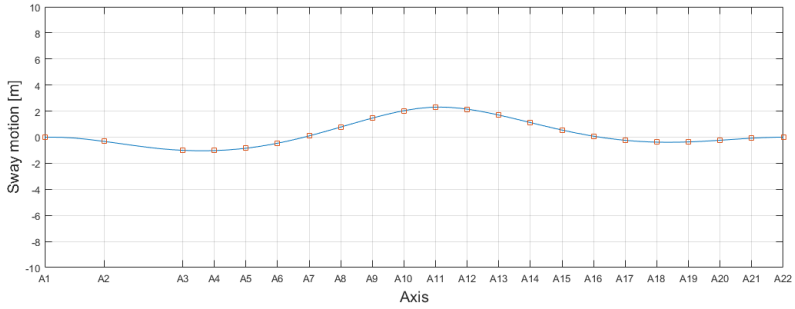

(a) Horizontal decay test 2, t = 200 s

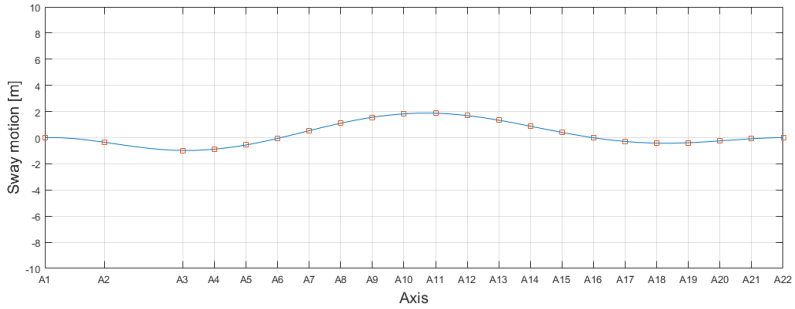

(b) Horizontal decay test 2, t = 270.5 s

Figure 3.27: Horizontal decay test 2: (+y) force on A11.

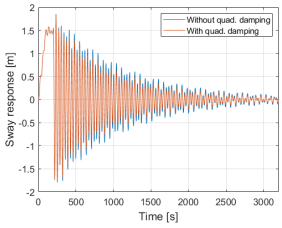

(a) A9

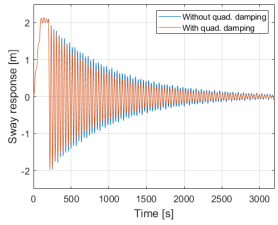

(b) A10

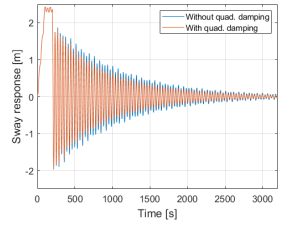

(c) A11

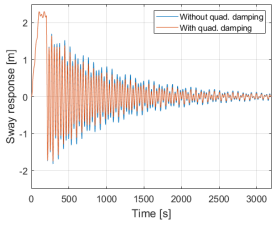

(d) A12

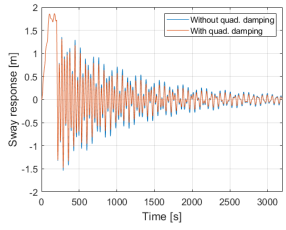

(e) A13

Figure 3.28: Time history of horizontal decay test 2.

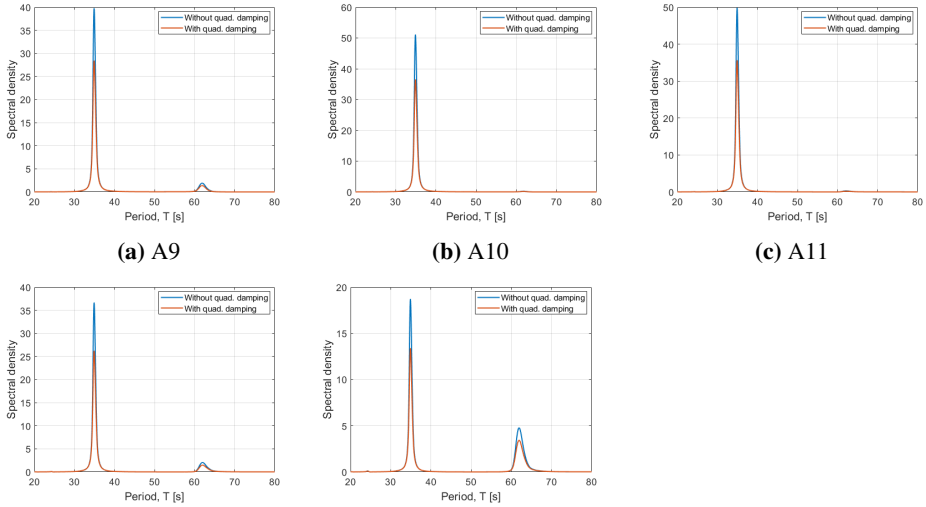

(a) A9 **(b)** A10 **(c)** A11

(d) A12 **(e)** A13

Figure 3.29: Spectral density of horizontal decay test 2.

Table 3.10: Result of horizontal decay test 2 at A11.

			without quad. damp	with quad. damp
Natural period	T_n	$[s]$	34.91	34.91
Natural frequency	ω_n	$[rad/s]$	0.180	0.180
Damping ratio	λ	[%]	0.85	0.98
Critical damping	B_{cr}	$[Ns/m]$	8.629 E+06	8.629 E+06
Total damping	B_{tot}	$[Ns/m]$	7.312 E+04	8.433 E+04
Potential damping	B_{pot}	$[Ns/m]$	1031	1031
Structural damping	B_{str}	$[Ns/m]$	7.209 E+04	7.209 E+04
Lin. viscous damping	B_{vis}	$[Ns/m]$		1.121 E+04
Potential damping ratio	B_{pot}/B_{cr}	[%]	0.01	0.01
Structural damping ratio	B_{pot}/B_{cr}	[%]	0.84	0.84
Lin. viscous damping ratio	B_{pot}/B_{cr}	[%]		0.13

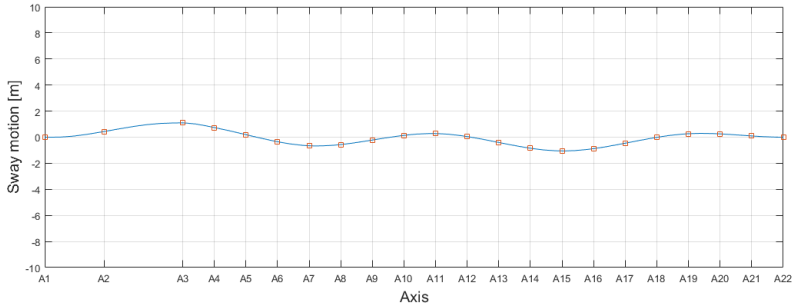

(a) Horizontal decay test 3, t = 200 s

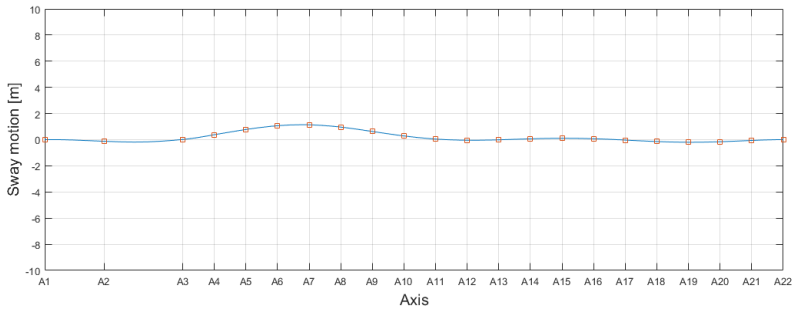

(b) Horizontal decay test 3, t = 251.5 s

Figure 3.30: Horizontal decay test 3: (+y) force on A3, A11 and A19, and (-y) force on A7 and A15.

3.6.6 Horizontal Decay Test 3

The last horizontal decay test was performed as the positive loads are applied on A3, A11, and A19, while the negative forces are applied on A7 and A15, *Figure 3.30a*. After released the loading, the bridge responded in complex combined shapes as described in *Figure 3.30b*.

As can be found from the time history and the spectra in *Figure 3.31* and *3.32*, more than 3 mode shapes are mixed in the response. *Table 3.11* summarized the captured eigen periods at each pontoon. From this decay test, the third horizontal eigen period of around 20.3 s was captured, however, the contribution is much smaller than the first and the second mode shapes.

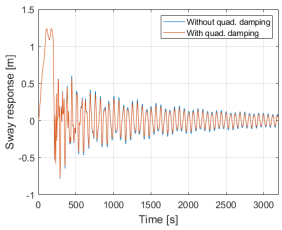

(a) A3

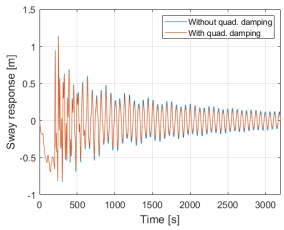

(b) A7

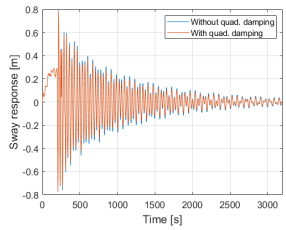

(c) A11

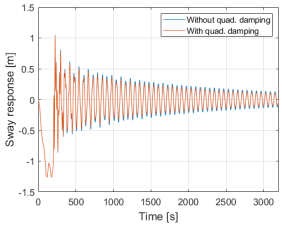

(d) A15

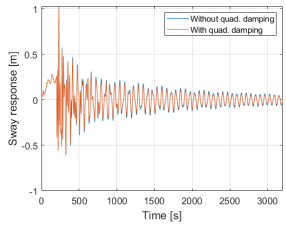

(e) A19

Figure 3.31: Time history of horizontal decay test 3.

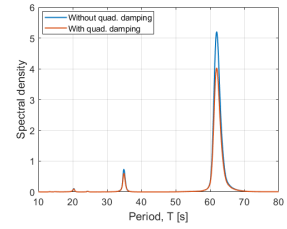

(a) A3

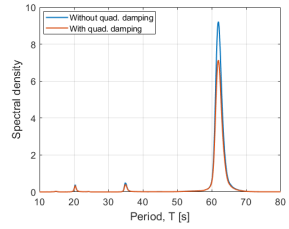

(b) A7

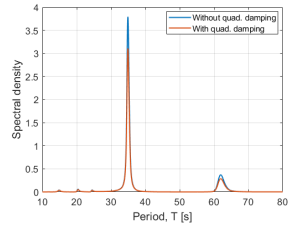

(c) A11

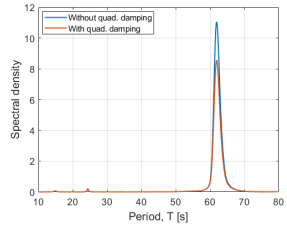

(d) A15

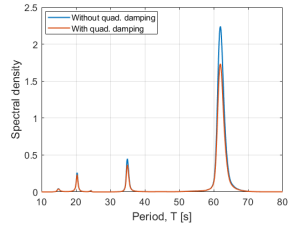

(e) A19

Figure 3.32: Spectral density of horizontal decay test 3.

Table 3.11: Result of horizontal decay test 3.

	T_n $[s]$	ω_n $[rad/s]$
A3	20.31, 34.91, 61.98	0.309, 0.180, 0.101
A7	20.35, 34.95, 61.98	0.309, 0.180, 0.101
A11	34.91, 61.98	0.180, 0.101
A15	61.98	0.101
A19	20.35, 34.91, 61.98	0.309, 0.180, 0.101

3.7 Global Dynamic Responses

In this part of the section, the global dynamic responses of the floating bridge under different environmental conditions were analyzed. The environmental condition contains local wind-generated waves, swell, wind, and wave and wind combined conditions as predefined in *Table 3.2*. The simulations were performed with viscous effect and the global dynamic responses were obtained including heave and sway motion, axial force, weak axis and strong axis bending moments. Statistical properties of the standard deviation, maximum and minimum values are discussed for heave and sway responses analysis. The structural responses of the axial force, the weak axis bending moment and the strong bending moment are analyzed with the static mean in still water condition and the dynamic mean, maximum, minimum, absolute maximum magnitude and the standard deviation under different environmental conditions. Absolute maximum magnitude is the largest absolute values obtained from the maximum or minimum values. Finally, the static and dynamic contributions to the responses of the bridge are investigated. The results related to shear force and torsional bending moment can be found in *Appendix B*.

After all simulations, it is confirmed that wave 1 and wind combination condition generates the maximum dynamic responses of the bridge, and the result of this condition is selected for further analysis. In order to reduce the uncertainty of the collected data, four additional simulations were performed with different seed numbers for wave 1 and wave condition. All data related to wave 1 and wind condition in this paper are based on five simulation results using different seed numbers.

3.7.1 Heave Motion

Figure 3.33 presents the standard deviation and the maximum and the minimum of heave responses under different conditions. As discussed earlier, the largest response can be found in the swell condition compared to the wind-generated wave conditions. Compared to wind and wave responses, the heave response under the wind condition is slightly smaller than that of the wave 1 but larger than the wave 2. In general, the heave response

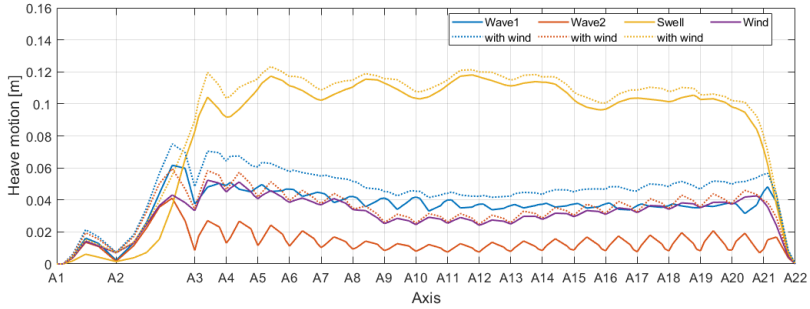

(a) Standard deviation

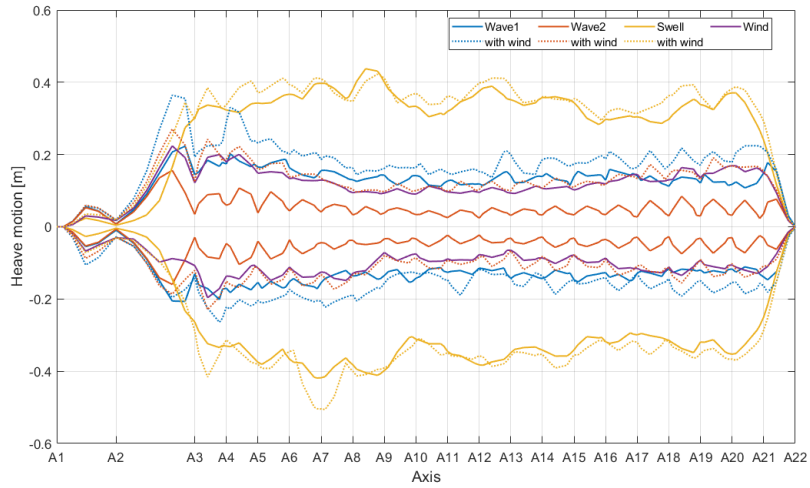

(b) Maximum and minimum

Figure 3.33: Statistical properties of the heave motion: (a) Standard deviation, and (b) Maximum and minimum values under different conditions.

under wave condition is larger than the wind condition. Under the wave and wind combined condition, the heave response increases. The largest heave response is around 0.4 m under the swell and wind combined condition.

3.7.2 Sway Motion

Following *Figure 3.34* illustrates the standard deviation, maximum and minimum of the sway response under different conditions. As can be clearly seen that wind is more effective than waves in terms of sway motion. Among wave conditions, the first wind wave condition shows the largest response, while the swell condition is with the least response.

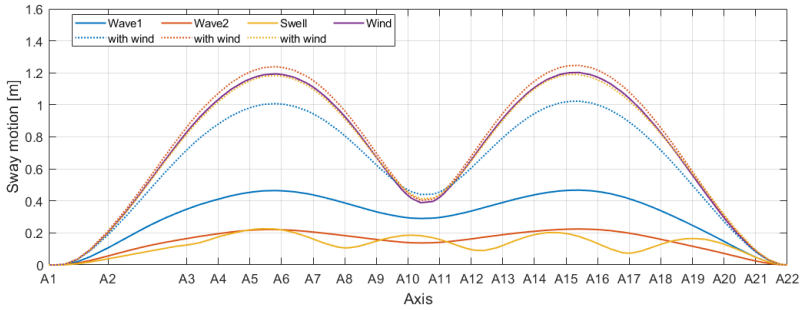

(a) Standard deviation

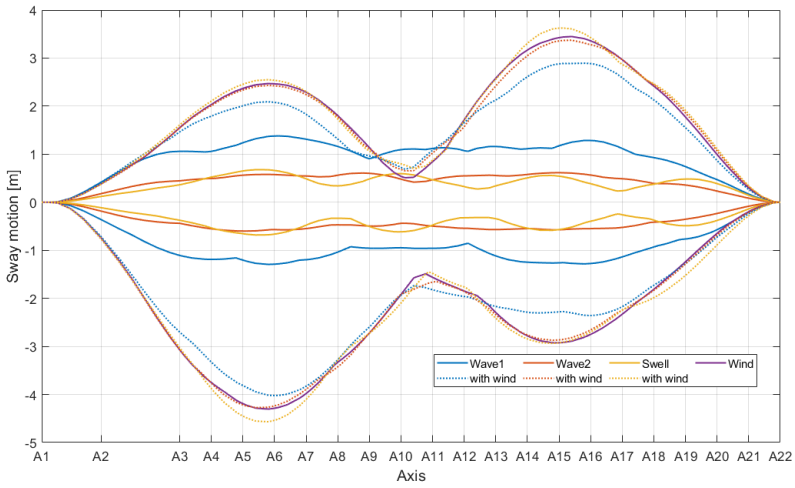

(b) Maximum and minimum

Figure 3.34: Statistical properties of the sway motion: (a) Standard deviation, and (b) Maximum and minimum values under different conditions.

When wind and wave combined, the sway response increases and the largest response is the swell and wind combined condition. The large sway responses are around 4.5 m in (-) y-direction under the wind and wind combined conditions. From the given figures, the sway mode shapes of the bridge, especially the first mode shape can be observed. Pontoons at A5, A6, A15, and A16 experience the greatest displacements, while pontoons at A10, A11, and pontoons at the ends experience the least displacements.

3.7.3 Axial Force

In the structural responses, static mean obtained from still water condition, dynamic mean, maximum, minimum, absolute maximum magnitude and standard deviation are presented. The axial force is largest at A2, but nearly zero at low floating bridge section. As can be seen in *Figure 3.35b*, the dynamic mean under wave conditions are very close to the static mean under still water condition. Dynamic mean changes only under wind condition due to mean wind force. The maximum and minimum values under wind-related conditions are smaller than wave conditions. This is because of the initial design of the floating bridge. The bridge is the curved shape that is convex to the west and the wind and waves come from the west, 270 °. Thus, when environmental load applies to the bridge, the bridge experiences compression which is a negative force in axial force. Thus, it is better to compare responses in absolute values as described in *Figure 3.35d*. This figure shows the absolute value of the largest amplitude among the minimum and maximum values. As also can be seen in *Figure 3.35e*, it is clear that wind and wind-related conditions have a greater effect on the axial force than the wave conditions.

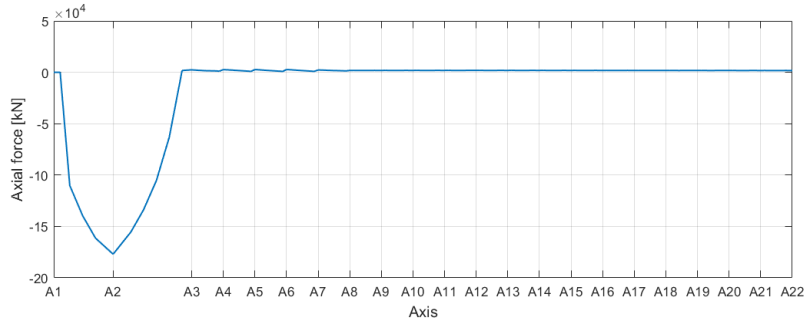

(a) Static mean

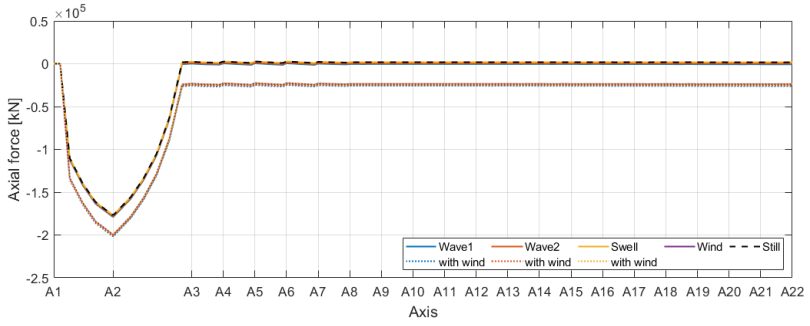

(b) Dynamic mean

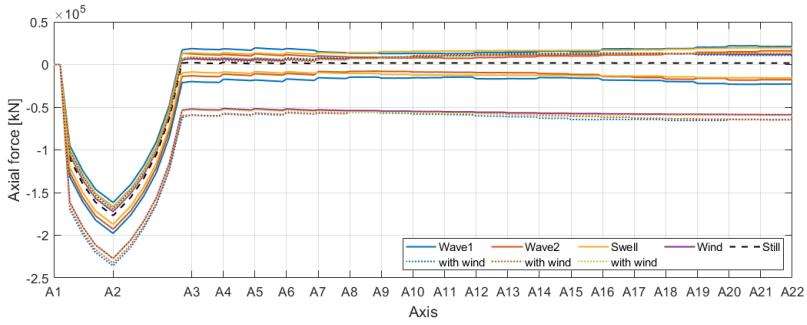

(c) Maximum and minimum

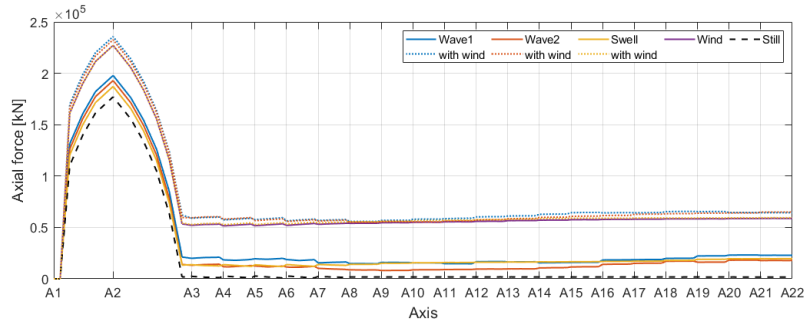

(d) Absolute maximum magnitude

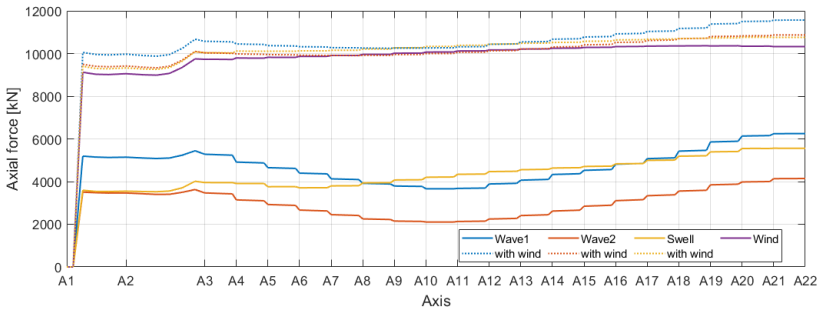

(e) Standard deviation

Figure 3.35: Statistical properties of axial force: (a) Static mean, (b) Dynamic mean, (c) Maximum and minimum, (d) Absolute maximum magnitude, and (e) Standard deviation under different conditions.

3.7.4 Weak Axis Bending Moment about the Local Y-axis

Following *Figure 3.36* presents the statistical properties of the weak axis bending moment. The weak axis bending moment varies significantly at the low floating bridge part along the bridge girder because the static weak axis bending moment is due to the weight of

the bridge and the buoyancy. Compared to the static mean and dynamic mean bending moments about the weak axis, no significant changes are found. The vertical response and the weak axis bending moment are mainly influenced by wave conditions. Therefore, a large variation can be observed at each floating pontoon location. The largest variations can be found under the first wave condition and the smallest variations are observed under wind condition. Although the most probable and severe conditions were applied in simulations, the dynamic effect on the weak axis bending moment is relatively small and the static mean is dominant in the response.

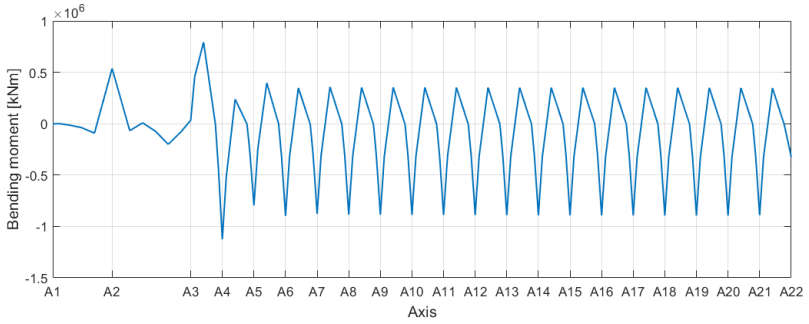

(a) Static mean

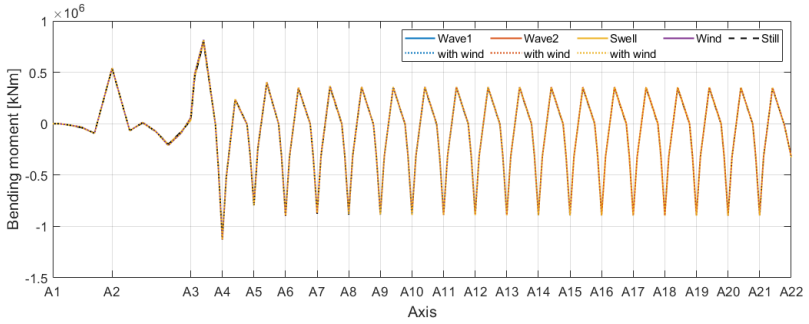

(b) Dynamic mean

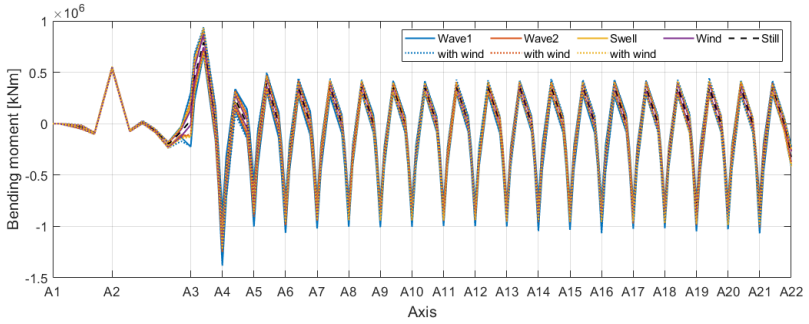

(c) Maximum and minimum

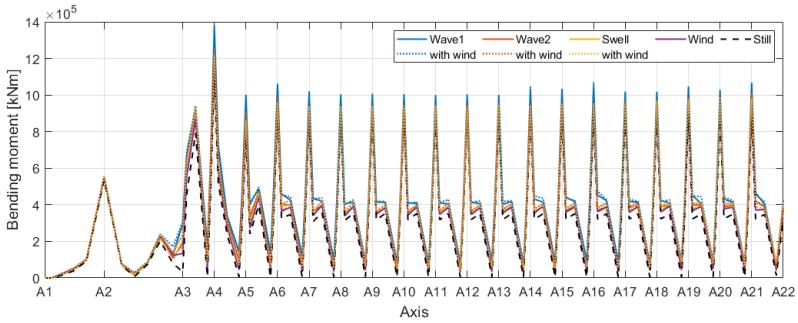

(d) Absolute maximum magnitude

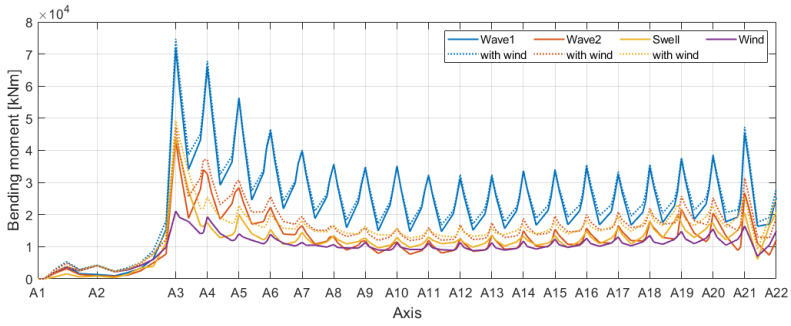

(e) Standard deviation

Figure 3.36: Statistical properties of bending moment about the local weak axis: (a) Static mean, (b) Dynamic mean, (c) Maximum and minimum, (d) Absolute maximum magnitude, and (e) Standard deviation under different conditions.

3.7.5 Strong Axis Bending Moment about the Local Z-axis

The statistical properties for the bending moment about the local z-axis are depicted in *Figure 3.37*. As can be seen in *Figure 3.37b*, the mean bending moment about the strong axis is not affected by wave conditions and seem almost the same as the static mean bending moment. However, due to the mean wind load, the mean strong axis bending moment changes under wind condition. As also can be found in *Figure 3.37c* and *3.37e*, the largest responses of the maximum, minimum and standard deviation are observed under the wind and wind-related conditions.

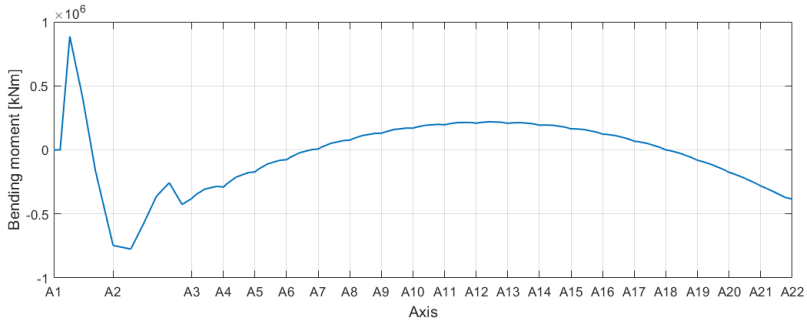

(a) Static mean

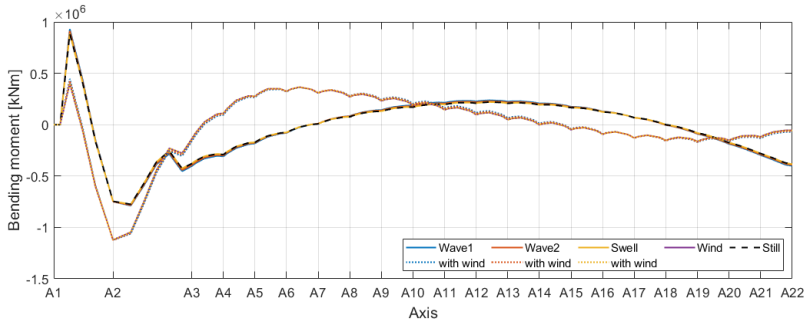

(b) Dynamic mean

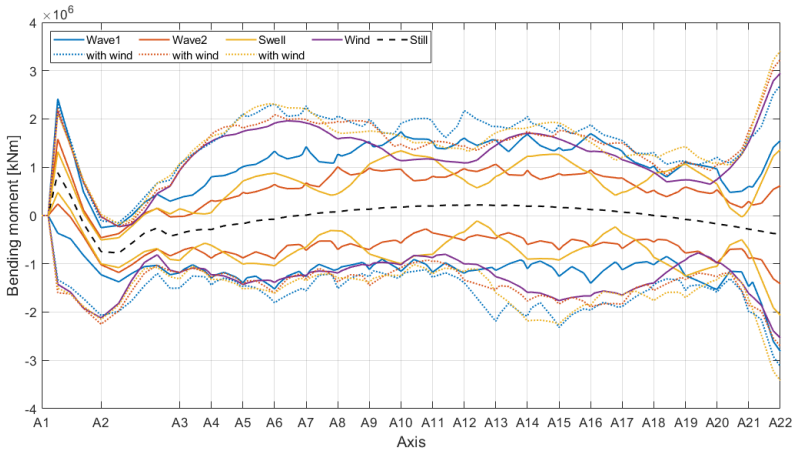

(c) Maximum and minimum

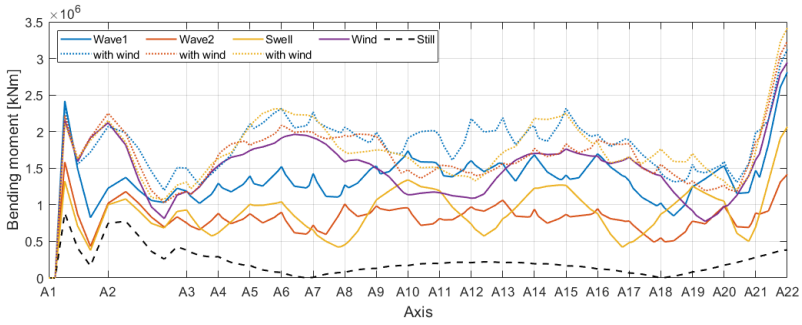

(d) Absolute maximum magnitude

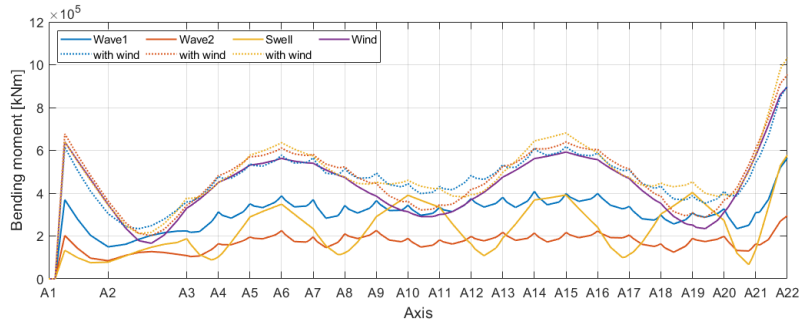

(e) Standard deviation

Figure 3.37: Statistical properties of bending moment about the local strong axis: (a) Static mean, (b) Dynamic mean, (c) Maximum and minimum, (d) Absolute maximum magnitude, and (e) Standard deviation under different conditions.

3.7.6 Static and Dynamic Contributions

The static and dynamic contributions are analyzed by comparing the static responses and dynamic responses. Most of the structural responses are found to be the largest values in wave 1 and wind combined condition; thus, the responses obtained from this condition are used in the analysis. The following *Figure 3.38* presents the total, static and pure dynamic contributions on the axial force, the weak axis bending moment and the strong axis bending moment. The black bold line indicates the dynamic total contribution obtained under the wave 1 and wind combined condition, while the red dashed line indicates the results obtained under the still water condition. By subtracting the static contribution from the total dynamic contribution, the pure dynamic contribution is obtained and presented in the blue dashed line.

As discussed earlier, it can be seen in *Figure 3.38a* and *3.38c* that the dynamic contribution is dominant in the axial force and the strong axis bending moment. The dynamic

contribution for the axial force and the strong axis bending moment is mainly due to wind condition. On the other hand, the weak axis bending moment is governed by the static condition as described in *Figure 3.38b*. The dynamic contribution for the weak axis bending moment is mainly induced by wave conditions, however the contribution is much smaller than the static contribution. The static weak axis bending moment is due to the bridge weight and the buoyancy.

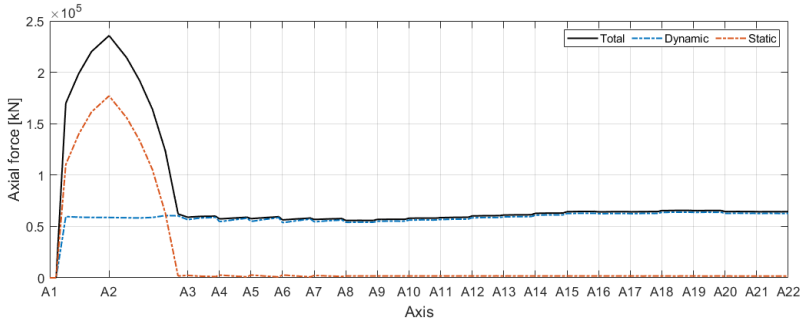

(a) Axial force

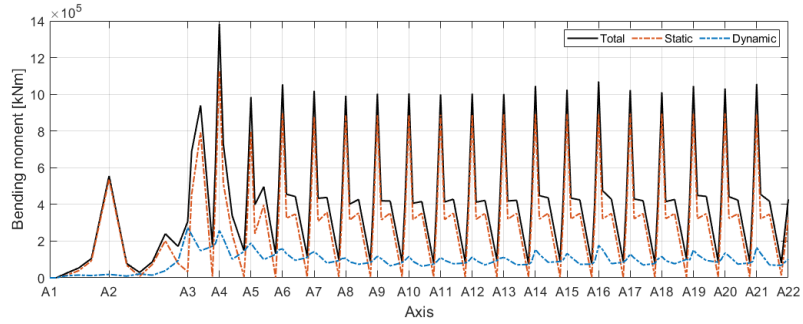

(b) Weak axis bending moment

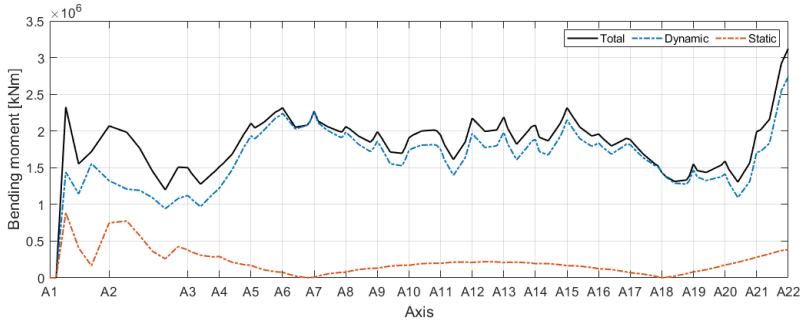

(c) Strong axis bending moment

Figure 3.38: Static and dynamic contributions for structural responses: (a) Axial force, (b) Weak axis bending moment, and (c) Strong axis bending moment.

3.8 Stress of the Bridge Girder

In this section, the stress of the bridge girder under different environmental conditions is analyzed. The stresses in the bridge girder include three stress components induced by the axial force, the weak axis bending moment and the strong axis bending moment, as given in (2.38). Each stress component can be calculated using the structural response, the structural characteristics of the bridge girder cross-section, and the points specified by (y, z) coordinates. The structural responses were obtained in the previous part and the structural properties of the bridge girder are summarized in *Table 1.5*. There are five types of cross-sections for the given bridge girder design and depends on the bridge girder cross-section, the area and the stiffness of the cross-section are different. The arrangement of the bridge girder cross section can be referred *Figure 1.8*.

In stress analysis, static bridge girder stress under still water condition and dynamic stresses under different environmental conditions are obtained and compared. The bridge girder stress at 10 different points, contribution of stress components, static and dynamic effects on stresses, and stresses under different environmental conditions are discussed.

3.8.1 Stress Observation Points

Figure 3.39 indicates points of interest in stress analysis. The coordinates of the points are as below. Point 2 and 7 are the furthest spots from the origin on the y-axis where the largest stress due to the strong axis bending moment is expected. Point 3 and 8 are the furthest spots from the origin on z-axis where the largest stress induced by the weak axis bending moment occurs. Point 4 and 9 are on the y-axis thus, only the stresses due to the axial force and the strong axis bending moment contribute. Point 5 and 10 are on the z-axis, therefore, the axial force and the weak axis bending moment contribute to the stress.

- $P_1\,(y\ ,\ z) = (24.5\ ,\ 1.5)$
- $P_2\,(y\ ,\ z) = (26.5\ ,\ -1.0)$
- $P_3\,(y\ ,\ z) = (21.5\ ,\ -3.5)$
- $P_4\,(y\ ,\ z) = (25.7\ ,\ 0)$
- $P_5\,(y\ ,\ z) = (0\ ,\ 1.5)$
- $P_6\,(y\ ,\ z) = (-24.5\ ,\ 1.5)$
- $P_7\,(y\ ,\ z) = (-26.5\ ,\ -1.0)$
- $P_8\,(y\ ,\ z) = (-21.5\ ,\ -3.5)$
- $P_9\,(y\ ,\ z) = (-25.7\ ,\ 0)$
- $P_{10}\,(y\ ,\ z) = (0\ ,\ -0.5)$

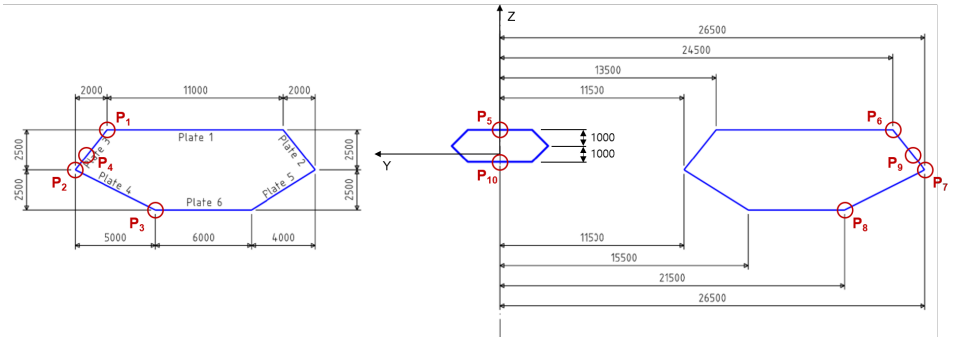

Figure 3.39: Stress points on the cross-section of the high bridge girder.

3.8.2 Static Bridge Girder Stress

The static bridge girder mean stress is calculated with the responses obtained from the still water condition and illustrated as *Figure 3.40*. The stress components and the total stress of the bridge girder under still water condition are presented.

Since the stress due to axial force described in *Figure 3.40a* is related to the area of the cross-section, it is the same in all points. Regarding the stress due to the weak axis bending moment in *Figure 3.40b*, the largest stress is found at point 3 and 8 as expected which is the farthest distance of 3.5 m from the origin on the z-axis. At point 1 and 5 with a distance of 1.5 m, the second largest stress is found and point 2 and 7, and point 10 are following. At point 4 and 9 are on z-axis; thus, no stress due to the weak axis bending moment is found. With respect to the stress induced by the strong axis bending moment illustrated in *Figure 3.40c*, the largest stress can be found at point 2 and 7 as predicted. However, the static mean stresses at different points are similar, although the distance from the origin on the y-axis is farther than the distance on the z-axis. At point 5 and 10 which are on the z-axis, no stress due to the strong axis bending moment exists.

As can be seen in *Figure 3.40d*, the total mean stress is governed by the stress component of the weak axis bending moment. This is because the stiffness on the z-axis is more than 5 times larger than the stiffness on the y-axis; thus, the stress due to the weak axis bending moment is expected to be larger than other contributions.

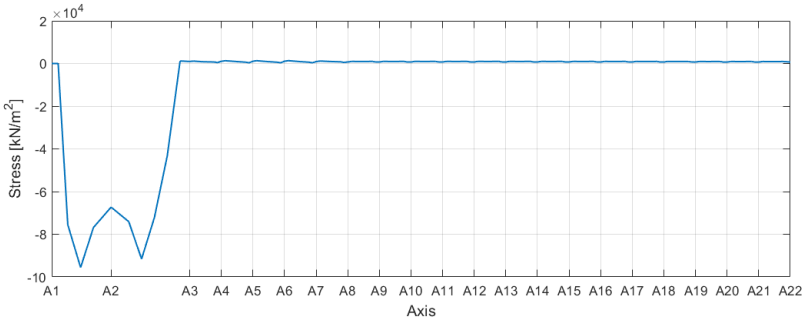

(a) Mean stress due to axial force

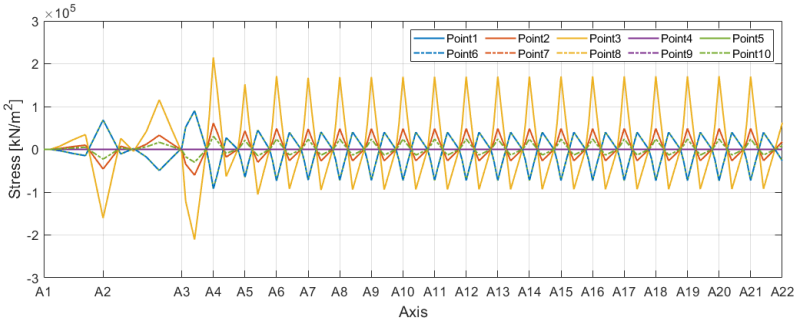

(b) Mean stress due to weak axis bending moment

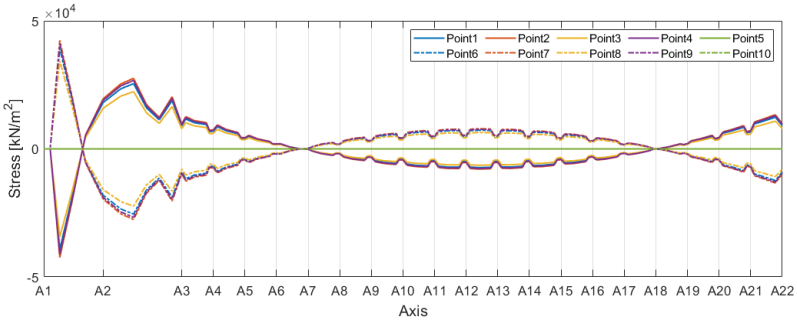

(c) Mean stress due to strong axis bending moment

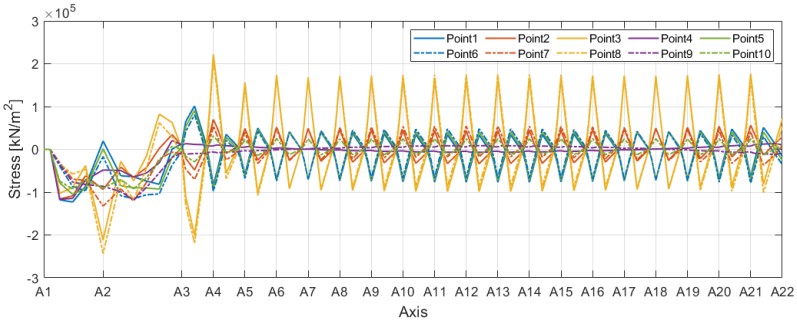

(d) Total mean stress

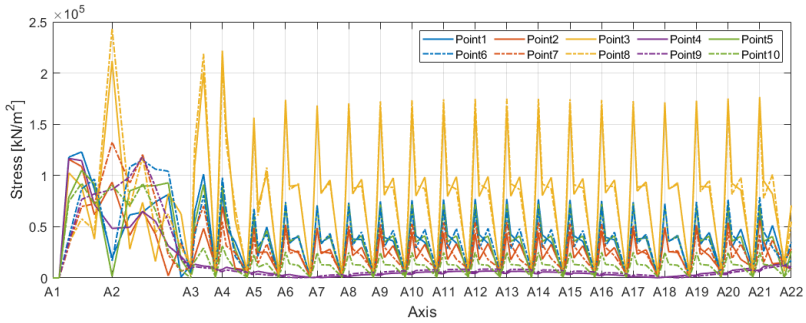

(e) Absolute total mean stress

Figure 3.40: The components and total of the bridge girder mean stress at different points under the still water condition: (a) Mean stress due to axial force, (b) Mean stress due to weak axis bending moment, (c) Mean stress due to strong axis bending moment, (d) Total mean stress, and (e) Absolute total mean stress.

3.8.3 Dynamic Bridge Girder Stress

Mean Stress

The dynamic bridge girder stress presented here is with the results simulated under wave 1 with wind condition. The other dynamic stress results in different conditions can be found in *Appendix C*. In this section, the mean of the stress component and the total stress, and the corresponding standard deviation are discussed.

Figure 3.41 presents the mean stresses due to the axial force, the weak axis bending moment and the strong axis bending moment, and the total mean stress under the wave 1 and wind combined condition. The largest mean stress can be found at point 3 and 8, while the smallest mean stress can be observed at point 4 and 9 where there is no stress due to weak axis bending moments. Overall the dynamic mean stress seems similar to the static mean stress. The comparison between the static and dynamic mean stress is discussed in 3.8.4.

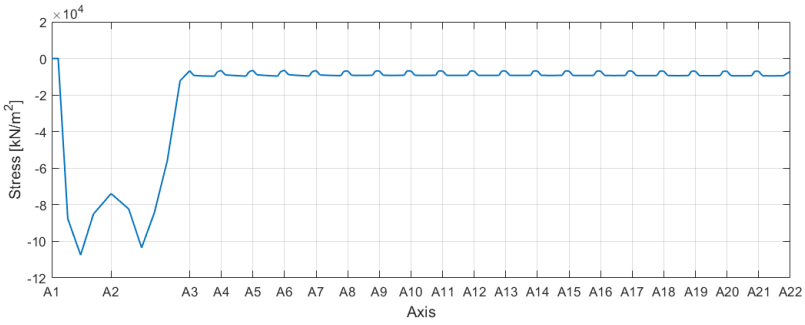

(a) Mean stress due to axial force

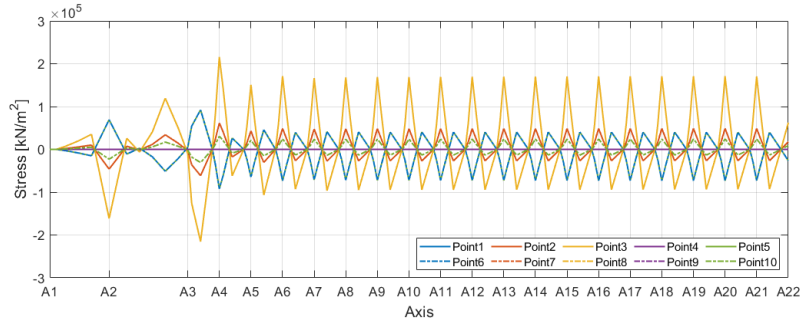

(b) Mean stress due to weak axis bending moment

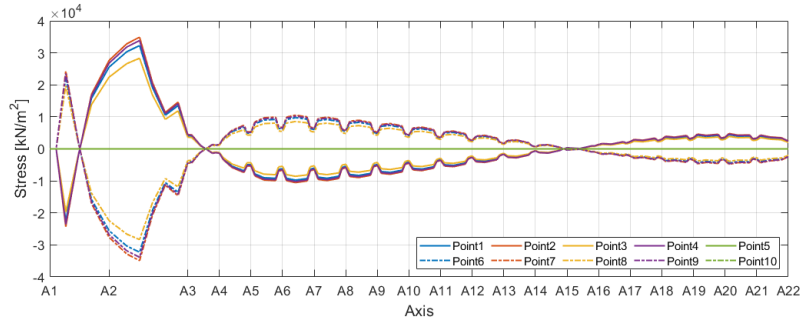

(c) Mean stress due to strong axis bending moment

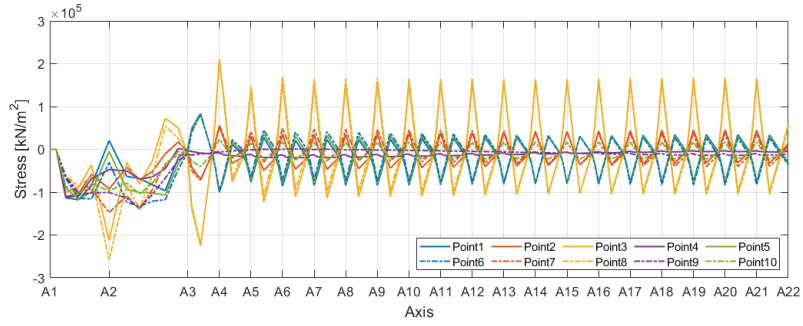

(d) Total mean stress

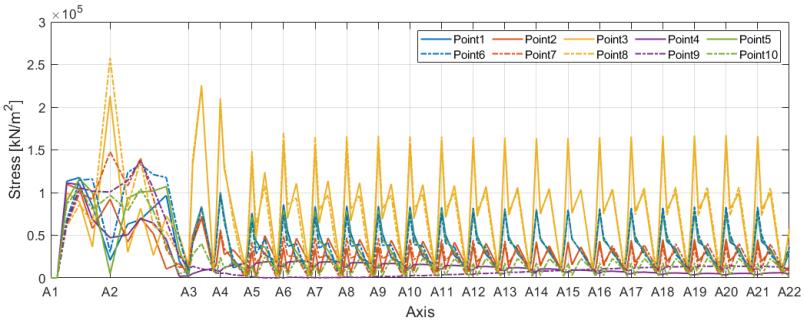

(e) Absolute total mean stress

Figure 3.41: The components and total of the bridge girder mean stress at different points under wave 1 with wind condition: (a) Mean stress due to axial force, (b) Mean stress due to weak axis bending moment, (c) Mean stress due to strong axis bending moment, (d) Total mean stress, and (e) Absolute total mean stress.

Standard Deviation of the Stress

The illustration of the standard deviation of the dynamic stress can be found in *Figure 3.42*. As can be observed in *Figure 3.42a* for the standard deviation of the stress due to axial force, relatively smaller variations are found at each pontoon location. The standard deviation of the axial force is similar along the bridge girder, as can be seen from *Figure 3.35e*, however since the section area at each pontoon location is larger than the area between the pontoons thus, the smaller standard deviations are found at each pontoon location.

The standard deviations of the stress components due to the weak axis bending moment and the strong axis bending moment are presented in *Figure 3.42b* and *3.42c*. These figures seem similar in general to the standard deviations of weak axis bending moment and the strong axis bending moment in *Figure 3.36e* and *3.37e*. However, depends on the stiffness of the cross-section peaks and humps can be found.

By looking at *Figure 3.42d*, the standard deviation of the total stress seems to be governed by the stress component due to the strong axis bending moment in dynamic condition.

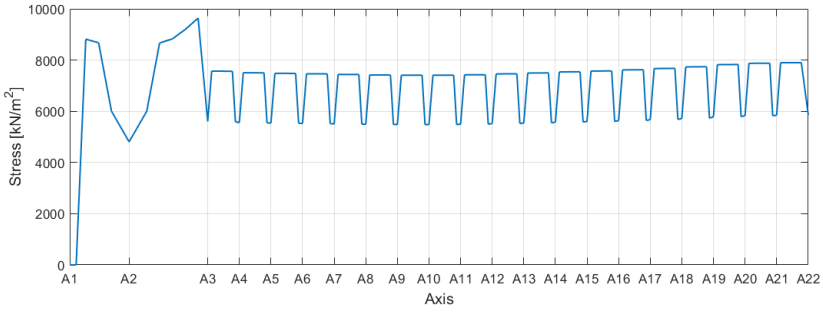

(a) Std of stress due to axial force

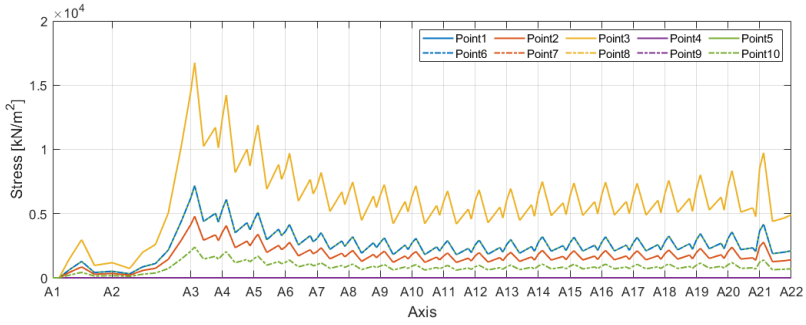

(b) Std of stress due to weak axis bending moment

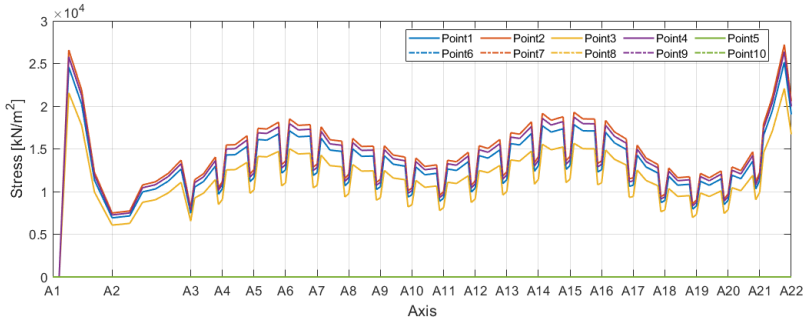

(c) Std of stress due to strong axis bending moment

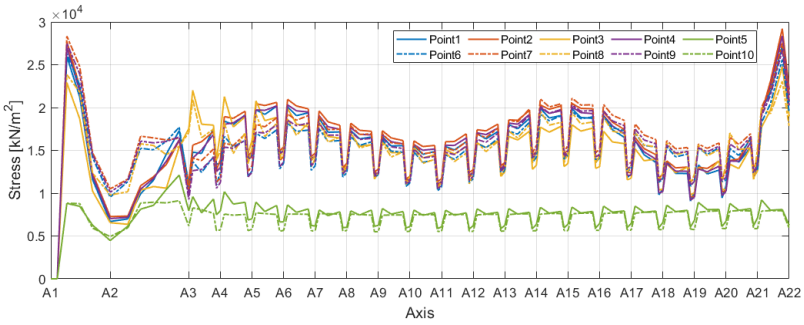

(d) Std of total stress

Figure 3.42: The standard deviation of the components and total bridge girder stress at different points under wave 1 with wind condition: (a) Std of stress due to axial force, (b) Std of stress due to weak axis bending moment, (c) Std of stress due to strong axis bending moment, and (d) Std of total stress.

3.8.4 Stress Comparison under Different Conditions

The bridge girder stresses under different environmental conditions are compared. Still water, wave 1, wind, and wave 1 and wind combined conditions are considered. *Figure 3.43* presents the comparisons of the mean stress, absolute mean stress and standard deviation for stress measured at point 3 under different conditions. Comparisons for other points can be found in *Appendix C*.

Mean Stress

As can be seen in *Figure 3.43a*, the mean stress is not much influenced by wave conditions and slightly changed in the wind-related conditions. Overall, the mean bridge girder stress is mainly governed by the static stress and dynamic effect is limited in the current bridge design.

Standard Deviation of the Stress

Comparing effects on the standard deviation of the stress due to the wave and the wind-related conditions, *Figure 3.43c* indicates that the wind-related conditions have a larger dynamic influence to the bridge girder stress than the wave condition. By comparing the mean stress and the standard deviation of the stress, the order of the standard deviation is 10 times smaller than the mean stress. Therefore, it can be confirmed that the dynamic variation of the stress is relatively smaller than the static effect.

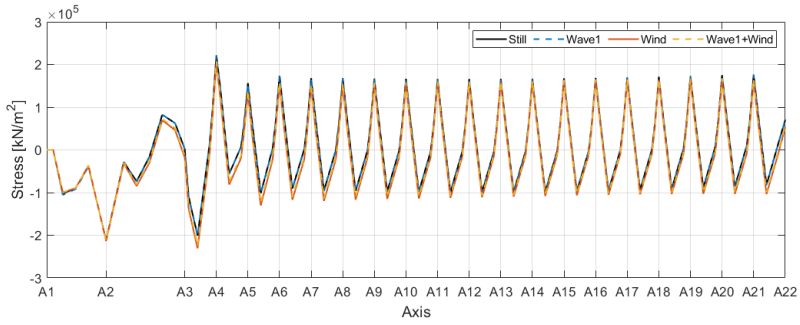

(a) Mean stress

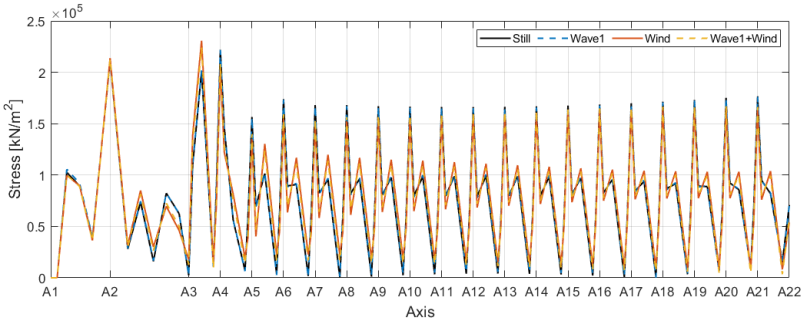

(b) Absolute mean stress

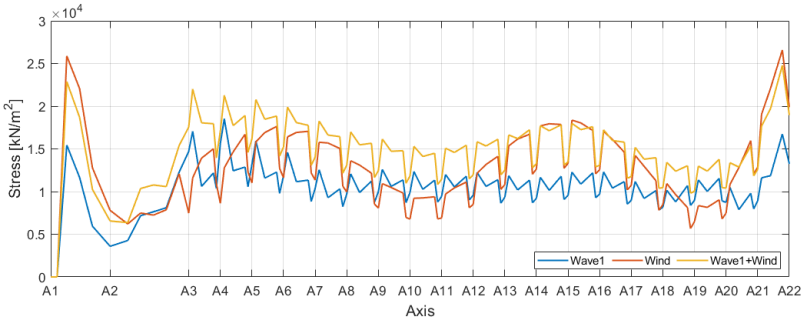

(c) Standard deviation

Figure 3.43: Comparisons of statistical properties of the total stress at point 3 under different conditions: (a) Mean stress, (b) Absolute mean stress, and (c) Standard deviation.

3.8.5 Stress Components Contributions

To understand the contribution of the stress components to the mean bridge girder stress and the standard deviation of the stress, the result at point 3 under the wave 1 and wind condition which with the largest stress is presented here. All results at 10 different points and under other environmental conditions can be found in *Appendix C*.

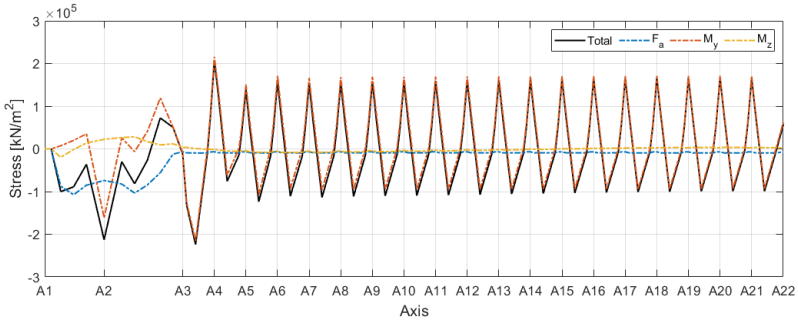

(a) Mean stress

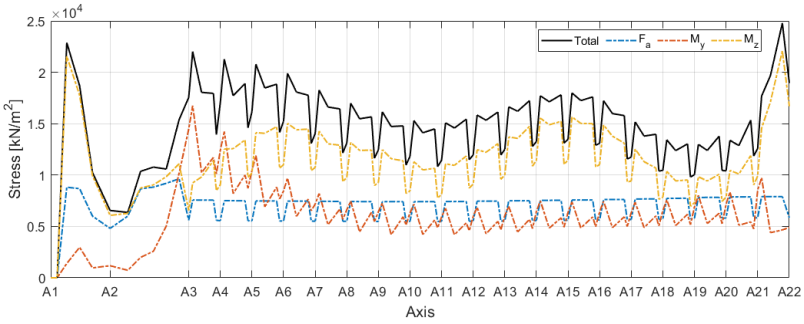

(b) Standard deviation

Figure 3.44: Contributions of (a) Mean stress and (b) Standard deviation at point 3 under wave 1 with wind condition.

Mean Stress

Since the shape of the total mean stress is similar to the mean stress induced by the bending moment about the weak axis, it is assumed that the stress due to the weak axis bending moment is the predominant factor. As can be seen from *Figure 3.44a*, it can be confirmed that the stress due to the weak bending moment is dominant in the total bridge girder mean stress. Compared to the stress induced by the weak axis bending moment, the contributions of the stress due to the axial force and the strong axis bending moment are unnoticeable.

Standard Deviation of the Stress

On the other hand, considering the standard deviation described in *Figure 3.44b*, the stress due to the strong axis bending moment makes the greatest contribution to the total stress variation. The contributions from the stresses due to the axial force and the weak axis bending moment are similar on low floating bridge part. However, the stress contribution due to the weak axis bending moment is large at A3 and A4 where the high and low bridge connected and the height of the bridge column changes.

3.8.6 Static and Dynamic Contributions to Stress

It was found that the dynamic effect on the bridge girder mean stress is small and the bridge girder mean stress is governed by the static mean stress, *Figure 3.43a*. Regarding the dynamic effect on the bridge girder stress with different environmental conditions, the wind-related condition seemed to be the largest influence to the bridge girder stress, *Figure 3.43c*. In this part, the contributions of the static and the dynamic effects on each stress component and the total stress under wave 1 and wind combined condition are discussed.

Stress due to Axial Force

Figure 3.45a shows the dynamic maximum, minimum and mean axial force stress with the static axial force stress. As summarized in *Table 3.12*, under the still water condition, the axial force on the high bridge part is around 95 MPa and the low bridge part is close to 1 MPa. As discussed previously, the mean and standard deviation of axial force is influenced by wind more than waves. Due to the mean wind load, the bridge experiences compression and the mean stress is increased in a negative direction around 7-12 MPa. Under the dynamic condition, especially with wave 1 and wind, the largest amplitude of the axial force stress on the high bridge part becomes around 140 MPa and low bridge part becomes around 25 MPa at pontoons and 35 MPa at middle girder parts between pontoons. The pure dynamic maximum effect is between 24-45 MPa.

Stress due to Weak Axis Bending Moment

As illustrated in *Figure 3.45b* and summarized in *Table 3.13*, the largest mean static stress due to the weak axis bending moment is around 160 MPa on the high bridge part, around 210 MPa near the high and low bridge connection between A3 and A4, 170 MPa at pontoons, and around 95 MPa at middle girder parts between pontoons. The dynamic mean stress is almost the same as the static mean stress. The largest stress in the dynamic condition is around 165 MPa at the high bridge, around 260 MPa near the connection, around 200 MPa at pontoons and around 110 MPa at middle girder parts. Overall, the pure dynamic maximum effect on the stress component due to the weak axis bending moment is around 5-50 MPa.

Stress due to Strong Axis Bending Moment

Table 3.14 summarized the static mean, dynamic mean, dynamic maximum and the pure dynamic maximum stress induced by the strong axis bending moment. The pure dynamic maximum effect on the stress due to the strong axis bending moment is of between 40-66 MPa and it is relatively large compared to the static mean stress of between 4-34 MPa. As described in *Figure 3.45c*, the static and the dynamic mean stress is very small at the low bridge part thus, the stress is governed by the dynamic contribution.

Total Stress

Finally, *Figure 3.45* presents the static and dynamic contribution to the total stress at point 3 under wave 1 and wind combined condition. As summarized in *Table 3.15*, the noticeable static mean stresses at different location are between 98-210 MPa and the dynamic mean stresses at different bridge parts are similar to the static stress. The maximum bridge girder stress can be found as around 290 MPa between A3 and A4 and the pure dynamic contribution is 90 MPa, 31 % of the total stress. Although the biggest dynamic contribution ratio is found at the middle girder parts between pontoons as 44 %, the value is 77 MPa out of the total stress of 175 MPa. Therefore, the maximum pure dynamic contribution on the bridge girder stress can be considered as 90 MPa while the static contribution is 200 MPA.

Overall, the dynamic contribution is not significant on the bridge girder stress even though the most probable and severe environmental conditions are applied. The static mean stress is the predominant factor with respect to the bridge girder stress. In order to reduce the bridge girder stress, reducing the static mean stress should be prioritized.

Table 3.12: Static and dynamic contributions on the bridge girder stress component induced by the axial force.

Stress $[MPa]$	High bridge	Connection	Pontoon	Middle Girder
Static mean	95	0.8	0.7	1
Dynamic mean	107	9.5	7	9
Dynamic max	140	35	25	35
Pure dynamic	45	34	24	34

Table 3.13: Static and dynamic contributions on the bridge girder stress component induced by the weak axis bending moment.

Stress $[MPa]$	High bridge	Connection	Pontoon	Middle Girder
Static mean	160	210	170	95
Dynamic mean	160	215	170	95
Dynamic max	165	260	200	110
Pure dynamic	5	50	30	15

Table 3.14: Static and dynamic contributions on the bridge girder stress component induced by the strong axis bending moment.

Stress $[MPa]$	High bridge	Connection	Pontoon	Middle Girder
Static mean	34	10	4	6
Dynamic mean	20	4	5	8.5
Dynamic max	100	50	50	65
Pure dynamic	66	40	46	59

Table 3.15: Static and dynamic contributions on the total bridge girder stress.

Stress $[MPa]$	High bridge	Connection	Pontoon	Middle Girder
Static mean	210	200	165	98
Dynamic mean	210	224	170	108
Dynamic max	240	290	215	175
Pure dynamic	30	90	50	77
Ratio	12.5%	31.0%	23.3%	44%

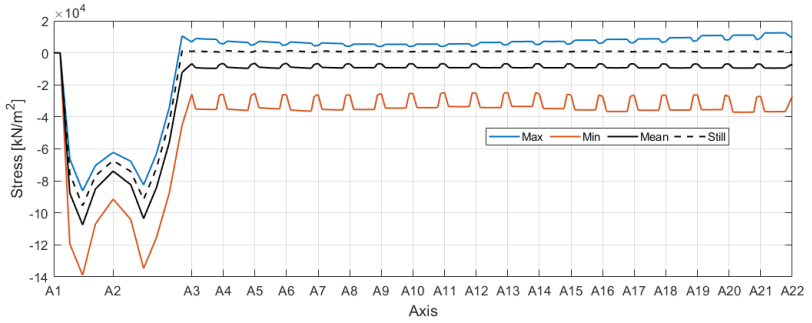

(a) Stress due to axial force

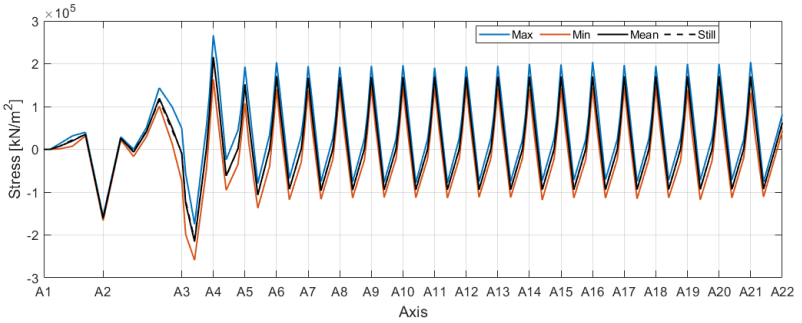

(b) Stress due to weak axis bending moment

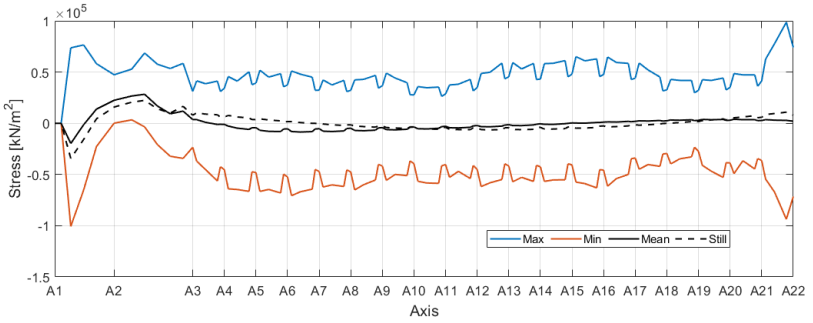

(c) Stress due to strong axis bending moment

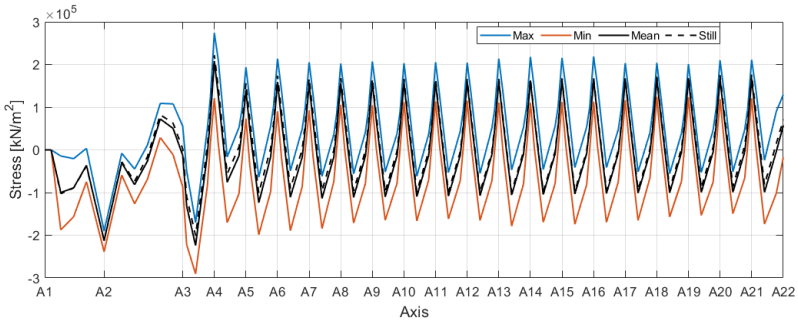

(d) Total stress

Figure 3.45: The static and dynamic contributions on components and total bridge girder stress at point 3 under wave 1 with wind condition: (a) Stress due to axial force, (b) Stress due to weak axis bending moment, (c) Stress due to strong axis bending moment, and (d) Total stress.

3.8.7 Spectral Analysis of Bridge Girder Stress

Spectral density of each stress component and the total stress were obtained to understand the frequencies and periods of the stress responses, *Figure 3.46*. In the spectra calculation, the stress responses of 5 simulations at point 3 on A15 under the wave 1 and wind condition were used.

As can be seen in *Figure 3.46a*, the stress due to the axial force responded by the mean wind force and the third eigen period of the sway motion of 22.76 s. The stress due to the weak axis bending moment described in *Figure 3.46b* responded mostly at the vertical eigen period of 7.95 s and 5.85 s, which is close to the given wave period of 6 s. Regarding the stress induced by the strong axis bending moment, the spectra of *Figure 3.46c* indicates that the response periods are mostly 63.02 s and 6.45 s. The main response period, 63.02 s, is close to the first horizontal eigen period, while the second-largest response period, 6.45 s, is one of the vertical resonance periods of the bridge.

In the spectral density for the total stress response, *Figure 3.46d*, all response periods captured in the stress components can be observed. Since the total stress is combined with the three different sources, the responding periods are complex. However, by considering the main responding periods for the total stress in the figure, the horizontal resonance periods of 63.02 s and 22.76 s are with the bigger area in the spectra than the vertical resonance periods of 7.73 s and 5.43 s. In other words, the response period of the total stress is highest from 63.02 s to 22.76 s, 7.73 s and 5.43 s. Since the horizontal response is mainly due to the wind conditions, it can be seen again that the wind condition is a key

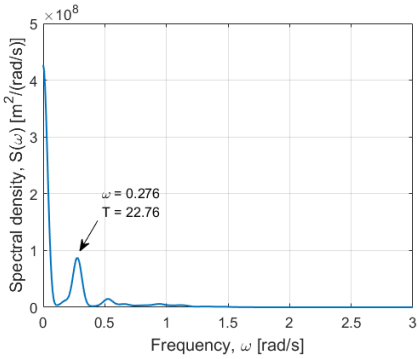

(a) Stress due to axial force

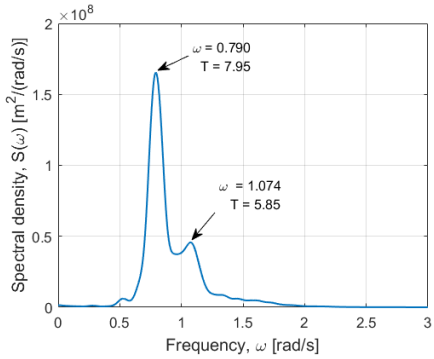

(b) Stress due to weak axis bending moment

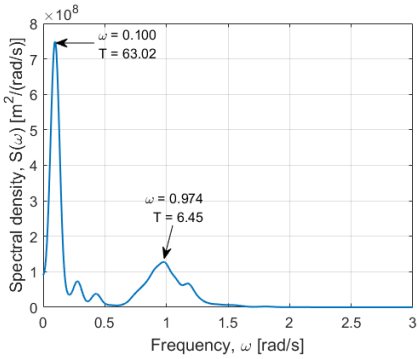

(c) Stress due to strong axis bending moment

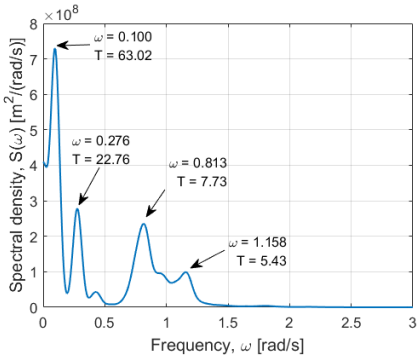

(d) Total stress

Figure 3.46: Spectra of the stress component and the total stress: (a) Stress due to axial force, (b) Stress due to weak axis bending moment, (c) Stress due to strong axis bending moment, and (d) Total stress.

factor that has a great dynamic influence on the bridge girder stress.

Chapter 4

Conclusion

The Norwegian Public Roads Administration (NPRA) is conducting the E39 Coastal Highway Route project to replace seven ferry connections with bridges and tunnels to reduce the 21 hour travel time between Trondheim and Kristiansand to 11 hours. The target site for this paper is Bjørnafjorden with a length of 5 km and a depth of 500 m. Due to this harsh geographical condition, it is difficult and expensive to build traditional bridges. As an alternative method, a cable-stayed curved floating bridge design has been proposed by COWI et al. and the numerical model of the bridge is prepared by Cheng et al. Because the given bridge is 5 km and is supported by 19 pontoons without side mooring, complex resonant responses are expected. The environmental conditions of the fjord differ from the oceans and are combined with local wind-generated waves, swell and winds. Thus, damping plays an important role in reducing the resonant responses of the bridge under harsh environmental conditions. In order to understand the various damping effects on the global dynamic responses of a given floating bridge, several steps of research have been carried out in this paper:

- Defining of the environmental conditions for simulations,
- Understanding vertical responses of the bridge without viscous effect,
- Wave condition sensitivity study on peak parameter,
- Establishing viscous damping of the floating bridge for heave motion,
- Understanding various damping contributions by decay tests,
- Investigating on the global dynamic responses of the bridge with viscous effect, and
- Analysis of the stress of the bridge girder.

Defining Environmental Condition

Based on the field measurement, numerical simulations and estimates on the environmental conditions, 100-year local wind-generated wave, 100-year swell and 100-year wind conditions were defined. It was found that the most probable and severe waves and wind comes from 270 °. *Table 4.1* summarized the defined environmental conditions for simulations. For simulations in harsh environmental conditions, wind wave and swell combination conditions and wave and wind combination conditions were used together.

Table 4.1: Environmental conditions for simulations.

	$H_s\ [m]$	$T_p\ [s]$	γ [-]	θ_p [°]	n [-]	$V_{mean}\ [m/s]$
Wave 1	3.0	6.0	2.3	270	4	
Wave 2	2.4	5.0	2.3	270	4	
Swell	0.4	14.0	5	270	15	
Wind						29.5

Vertical Responses without Viscous Effect

The first SIMO-RIFLEX simulations under wave conditions were performed to understand the dynamic response of the floating bridge without viscous effect. The heave response without the viscous effect is around 0.2 - 0.5 m. Comparing wind-generated wave conditions, as the significant wave height increases the heave response also increases. The response due to the swell condition was expected to be with the lowest heave response, however, the heave motion under the swell condition is the largest response among wave conditions. Compared to the wavelength of the wind-wave conditions, 56 m and 39 m, the wavelength of the swell condition is 225 m. Therefore, several pontoons can respond together in a similar phase angle under the swell condition and have a larger heave motion, while under the wind wave conditions, pontoons rather responded individually and have a smaller heave motion. It can be also confirmed by investigating the spectral density of the heave motions. The peaks of the heave motions for wind-generated waves are mostly the eigen period of the vertical motion of the bridge, however, the peaks of the swell responses are the same as the given swell period. Hence, under wind-generated wave conditions, pontoons respond individually in the vertical eigen period, while under swell condition, pontoons respond together in the swell period. Due to individually responding pontoons under the wind-generated wave conditions, a large variation of the weak axis bending moment is observed. Since pontoons responded together under the swell condition, a smaller weak axis bending moment is found. Under the wind wave conditions, the weak axis bending moment increases as the significant wave height increase. However, the dynamic effect on the weak axis bending moment is small since the static weak axis

bending moment is predominant in the current bridge design.

Wave Condition Sensitivity Study on Peak Parameter

In simulations, wave conditions are generated by using the JONSWAP spectrum and non-dimensional peak parameter, γ. The peak parameter for the simulations are given from NPRA, however during the thesis preparation work last semester, the wave conditions were modeled with the calculated parameter. In order to understand the influence of the peak parameter, wave condition sensitivity study was performed. The given peak parameters are 2.3 for wind-generated waves and 5 for swell, while the calculated parameters are 5 for wind-generated waves and 1 for swell. As can be observed *Figure 4.1*, since the given parameter for wind waves are smaller than the calculated one, the height of the wave spectra generated by the given parameter is reduced and the width is wider. On the other hand, the height of the swell spectra is increased and the width is narrower. As a consequence, the heave motion and the weak axis bending moment under the wind wave with the given parameter is larger than the responses obtained from the wave condition with the calculated parameter. Under the swell condition, the responses are slightly reduced with the given peak parameter compared to the responses obtained from the swell with the calculated parameter.

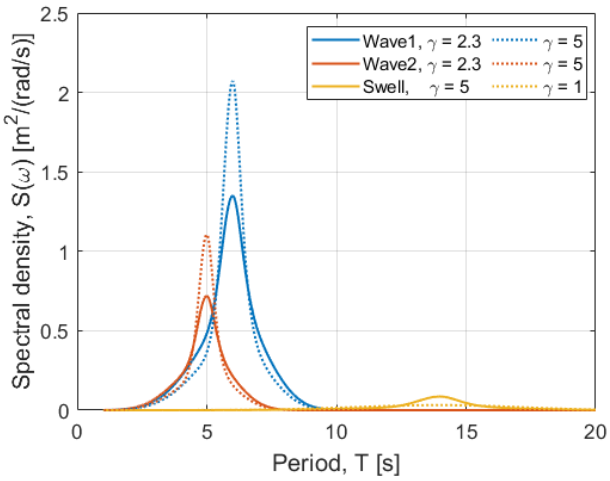

Figure 4.1: Comparison of wave spectra with different peak parameter.

Viscous Damping Modeling

The viscous damping for heave motion was modeled by using KC dependent drag coefficient. KC number is calculated with heave amplitude and flange width as a characteristic length. In drag force calculation, KC dependent drag coefficient is used with the flange area only, while the conventional drag coefficient is used with the entire projected area. Therefore, for convenience, the equivalent drag coefficient that can be used the projected area is also calculated. *Table 4.2* summarized the KC number, KC dependent drag coefficient and the adjusted conventional drag coefficient as a function of heave amplitude. In simulations, the drag coefficient of $C_{dz,kc} = 23.98$, $C_{dz} = 8.3$ is used for heave motion. Robert Read in DTU obtained the equivalent constant drag coefficient from the time series of KC number. The obtained equivalent constant drag coefficient for the wind-generated wave is between 23.55 - 26.17. Thus, the applied KC dependent drag coefficient of 23.98 can be considered as a reasonable value.

Table 4.2: KC dependant and equivalent drag coefficients in z-axis.

Heave amplitude, ζ $[m]$	0.2	0.3	0.5
KC number	0.2513	0.3770	0.6283
$C_{dz,kc}$	25.91	23.98	21.56
C_{dz}	8.96	8.30	7.46

Decay Tests

After modeling the drag coefficient, the viscous effect on vertical responses was observed. When the viscous damping is applied, the amplitudes of the responses were generally reduced however, the viscous effect is small. Free decay tests were performed to understand the contributions of various damping. Three vertical free decay and three horizontal free decay tests were conducted with different loading conditions. The loading conditions were chosen to generate the vertical and horizontal mode shapes. Since the bridge is flexible structure supported by 19 pontoons without mooring, generating the same targeting mode shapes is difficult. However, from the complex responses, the necessary information including eigen periods and damping ratio were captured.

The eigen period of the vertical motions is found between 7.55 - 10.93 s. The found results are very close to the eigen period of the vertical motion for the bridge of 7.5 - 10.95 s obtained from the numerical simulation. *Table 4.3* summarized the observed eigen period and damping contributions in heave and sway motions. The measured damping ratio for heave motion are 1.49 %, 2.19 %, 3.13 %, and 6.81 % linearized viscous damping, structural damping, potential damping, and total damping, respectively. Depends on the bridge

Table 4.3: Various damping contributions in different motions.

	Eigen period $[s]$	Damping ratio $[\%]$			
		Lin. Viscous	Structural	Potential	Total
Heave	10.91	1.49	2.19	3.13	6.81
Sway	62.16	0.47	0.50	0.00	0.97
	34.91	0.13	0.84	0.01	0.98

response, the structural damping and the linearized viscous damping can vary, however, the viscous effect, in general, is small due to the small heave response under the given environmental conditions.

Regarding the horizontal free decay tests, the noticeable eigen periods of 62.16, 34.91 and 20.31 were captured. The numerically estimated eigen periods for horizontal motions are 56.72, 31.69 and 22.68 for the first, second and third mode shapes; thus, the major horizontal mode shapes were observed during the free decay test. As can be seen in *Table 4.3*, the linearized viscous damping is 0.47 % and 0.13 % for the first and the second mode shapes, while the total damping is 0.97 % and 0.98 % respectively. Since the pontoons move horizontally in a similar phase angle and there is no side mooring of the bridge, the structural damping in the y-axis is much smaller than z-axis. Besides, the horizontal motion changes slowly compared to the vertical motion; therefore, the quadratic viscous effect is also small.

Global Dynamic Responses with Viscous Effect

The global dynamic responses of the floating bridge with the viscous effect under different environmental conditions were investigated. The applied environmental conditions are including 100-year wind-generated wave, 100-year swell, 100-year wind, and combined conditions.

Considering the heave and sway motions, it is found that the heave response is mainly affected by wave conditions, and the sway response is mainly affected by wind conditions. In sway motion, the pontoons at $1/3$ and $2/3$ of the bridge experience the largest displacement in the y-axis while the pontoons in the middle of the bridge move with the smallest distance. This phenomenon also can be found in the first mode shape of the sway motion presented in *Figure 1.13a*.

Regarding the axial force of the bridge girder, it is found that the dynamic contribution on the axial force is dominant especially on low floating bridge section. Under different environmental conditions, the axial force is not much affected by the wave conditions but

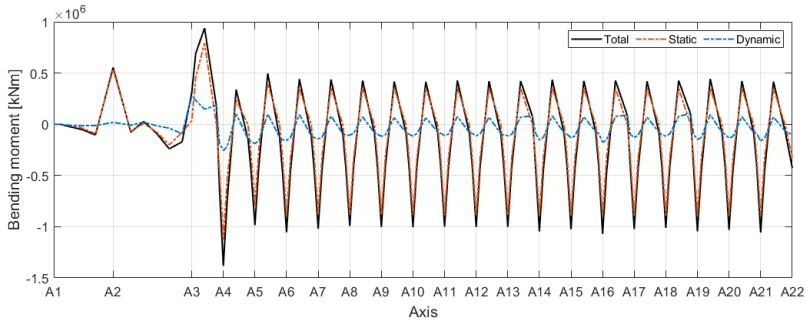

Figure 4.2: Static and dynamic contributions for weak axis bending moment.

mainly the wind condition.

With respect to the weak axis bending moment, wave conditions are more influential than wind conditions. However, although the most probable and severe wave and wind conditions were applied, the dynamic variation of the weak axis bending moment is relatively small due to the predominant static weak axis bending moment as illustrated in *Figure 4.2*. The static weak axis bending moment is induced by the bridge weight and the buoyancy at pontoons. Since the dynamic contribution on the weak axis bending moment is small, the viscous effect is also small.

On the other hand, the strong axis bending moment is governed by dynamic contribution. Compared to wave and wind conditions, wind and wind combined conditions are effective on the strong axis bending moment variation.

Stress of the Bridge Girder

The bridge girder stresses under different environmental conditions were analyzed. 10 different points in the cross-section of the bridge girder described in *Figure 3.39* were selected and 4 different environmental conditions including still water, wave 1, wind, and wave 1 with wind combined conditions were applied. The total bridge girder stress consists of stresses due to axial force, weak axis bending moment, and strong axis bending moment.

Among 10 observation points for stress analysis, point 3 and point 8 in the cross-section show the largest stress. Point 3 and point 8 are the furthest points from the origin on z-axis which have the largest stress induced by the weak axis bending moment.

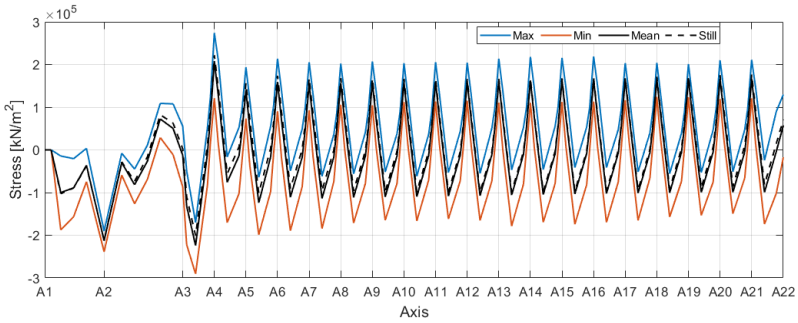

Figure 4.3: The static and dynamic contributions on the total bridge girder stress at point 3 under wave 1 with wind condition.

By comparing total stress under different environmental conditions, the largest stress variation is found under wave 1 and wind combined condition. However, the dynamic mean stresses under environmental conditions do not much differ from the static mean stress.

In the total mean stress, the stress due to the weak axis bending moment mostly contributes, while the stress contributions from the axial force and the strong axis bending moment are small. However, considering the standard deviation of the total stress, the largest stress contribution comes from the strong axis bending moment and the contributions from other sources are small.

Figure 4.3 presents the total bridge girder stress at point 3 under wave 1 with wind combined condition. Blue, red and bold black lines indicate the maximum, minimum, and mean stress under the dynamic condition, while the black dashed line indicates the mean static stress. Although the most severe environmental conditions are applied, the dynamic effect on the bridge girder stress is relatively smaller than the static effect. The static mean stress is the governing factor of the total stress and the weak axis bending moment is the main contributor to the static mean stress. Therefore, from the stress analysis, it can be concluded that the bridge girder stress is governed by the weak axis bending moment.

Summary

The given floating bridge is 5 km long and supported by 19 pontoons without side mooring provided by COWI et al. In order to understand various damping contributions against the resonant responses of the bridge, numerical simulations were performed in SIMO-RIFLEX with the given numerical model prepared by Cheng et al. Viscous damping for heave motion is modeled by using KC dependent drag coefficient and the various damping

effects were investigated. From the decay tests, it was found that the potential damping is dominant in the heave motion, while the structural damping is dominant in the sway motion. In both cases, viscous effects are with the smallest effect. The investigation on the global dynamic responses of the given bridge design was conducted. It was found that the heave motion and the weak axis bending moment are affected by wave condition, while the sway motion, the strong axis bending moment, and the axial force are affected by wind condition. Since the bridge girder is relatively stiff against the vertical motion under wave condition, heave response is small and the viscous effect is also small. With the given results, the analysis on the bridge girder stress was performed. The bridge girder stress consists of stress components due to axial forces, weak axial bending moments and strong axial bending moments. Comparing static and dynamic contributions, it is found that the bridge girder stress of the given bridge design is governed by the static mean stress and the dynamic effect is not noticeable even under the most probable and severe 100-year environmental conditions. The static mean stress is mainly induced by the stress component of the weak axis bending moment, where the weak axis bending moment is governed by the static sources including the bridge weight and buoyancy.

Suggestion and Future Work

In order to reduce the bridge girder stress of the given design, reducing the static weak axis bending moment must be prioritized. By increasing the number of pontoons to redistribute the bridge weight, this can be one way to reduce the static weak axis bending moment.

Since the dynamic effects on the heave motion and the weak axis bending moment are small, the viscous damping effect is also small. However, if the static contribution on the weak axis bending moment is reduced in new bridge design, the viscous effect can be more important. The dynamic contribution on the bridge girder stress is mainly due to the strong axis bending moment where the wind is the main contributor to the strong axis bending moment variation. Although the damping effects on the horizontal motion are very small, any damping can be important in the resonance responses. Therefore, a slowly drifting damping for the horizontal motion can be investigated in the future researches.

When the heave response increases after reducing the static effect on the bridge girder, adjusting the eigen period of the vertical response of the bridge should be considered. Since the heave motion is mainly responded around eigen period of the bridge, optimization on the pontoon design to adjust the eigen period of the bridge away from the wave periods can be the next tasks.

Bibliography

[1] Lothe A. E39 Bjørnafjord Crossing, Design Wave Data. Technical Report; Norconsult AS, 2016.

[2] Jonkman BJ. TurbSim User's Guide v2.00.00. Technical report, 2014.

[3] Cheng Z, Gao Z, Moan T. Hydrodynamic load modeling and analysis of a floating bridge in homogeneous wave conditions. *Marine Structure*, 59:122–141, 2018.

[4] Cheng Z, Gao Z, Moan T. Numerical modeling and dynamic analysis of a floating bridge subjected to wind, wave, and current loads. *Journal of Offshore Mechanics and Arctic Engineering*, 141, 2019.

[5] Cheng Z, Svangstu E, Gao Z, Moan T. Field measurements of inhomogeneous wave conditions in bjørnafjorden. *Waterway, Port, Coastal, and Ocean Engineering*, 145, 2019.

[6] COWI. NOT-KTEKA-021 Curved bridge - navigation channel in south. Technical report, 2016.

[7] DNV. Environmental conditions and environmental loads, DNV-RP-C205. Recommended practice, 2014.

[8] Agustsson H Harstveit K, Bredesen RE. Bjørnafjorden, Hordaland, Kartlegging av vindforhold; Kjeller vindteknikk, 2016.

[9] MARINTEK. RIFLEX theory manual, Version 4.0, 2012.

[10] MARINTEK. SIMO theory manual, Version 4.0, 2012.

[11] Newmark, NM. A method of computation for structural dynamics. *Journal of the Engineering Mechanics Division. Proceedings of the ASCE*, 85, EM3, 1959.

[12] Norwegian Ministry of Transport and Communications. National Transport Plan 2018-2029, Meld. St. 33 (2016-2017). Report to the Storting, White paper, 2017.

[13] Faltinsen OM. *Sea loads on ships and offshore structures*. Cambridge University Press, 1990.

[14] Shao Y, Xiang X, Liu J. Numerical investigation of wave-frequency pontoon responses of a floating bridge based on model test results. *38th International Conference on Ocean, Offshore and Arctic Engineering.*, 2019.

[15] SMJ. Design basis Bjørnafjorden, Side- and end anchored floating bridge. Technical report; Statens vegvesen, 2016.

[16] Statens vegvesen. Bruprosjektering, håndbok n400, 2015.

[17] Statens vegvesen. An update from the Fjord Crossing Project. Presentation, 2016.

[18] Statens vegvesen. The Coastal Highway Route E39: Overview summary, 2018.

[19] Cummins WE. *The impulse response function and ship motions*. Universitat Hamburg, 1962.

[20] Alexandra Wynne. Floating solutions: Norway's extraordinary bridges plan.

Appendix A

Dynamic Horizontal Responses

A.1 Peak Parameter Comparison

A.1.1 Sway Motion

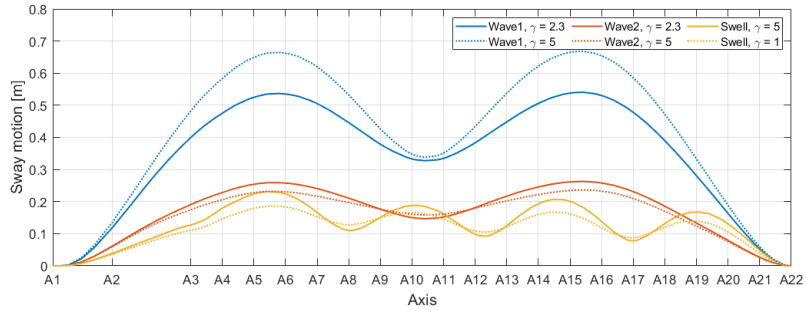

(a) Standard deviation

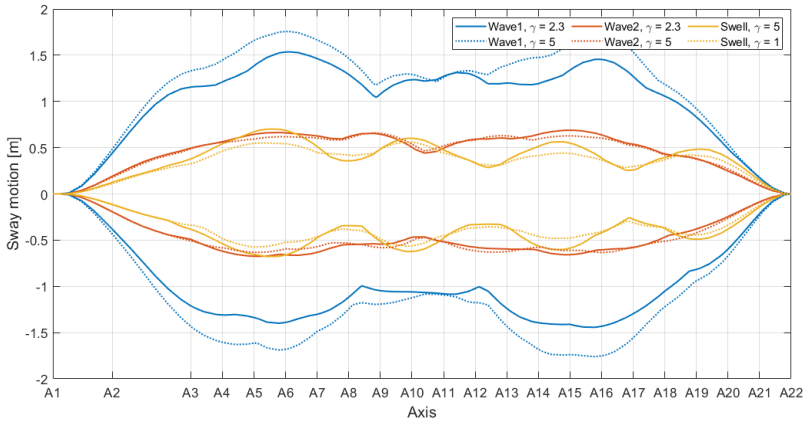

(b) Maximum and minimum

Figure A.1: Statistical properties of sway motion: (a) Standard deviation and (b) Maximum and minimum under waves with different peak parameters.

A.1.2 Strong Axis Bending Moment

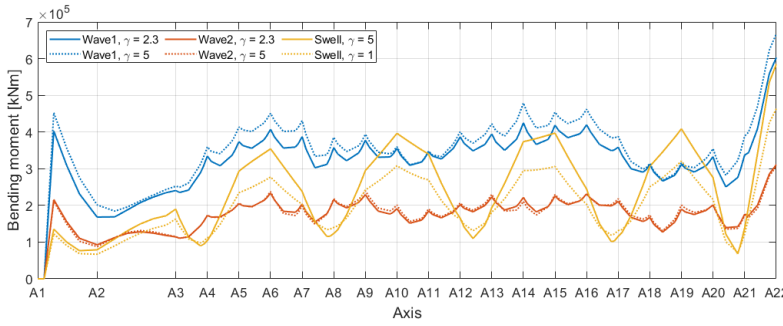

(a) Standard deviation

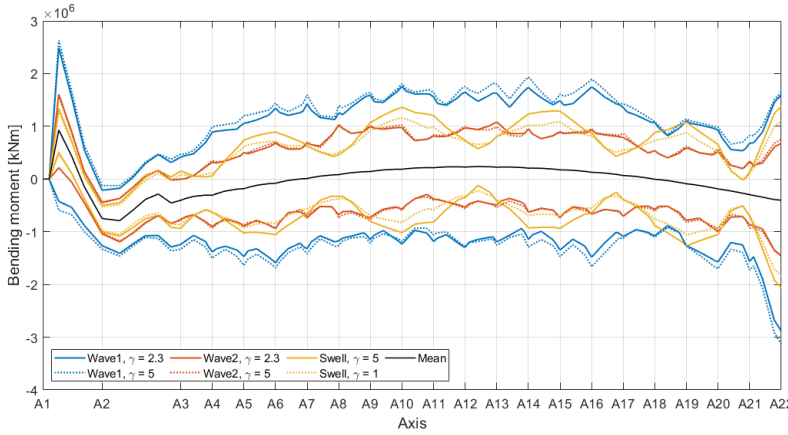

(b) Maximum, minimum and mean

Figure A.2: Statistical properties of strong axis bending moment: (a) Standard deviation and (b) Maximum, minimum and mean under waves with different peak parameters.

A.2 Wave Condition Comparison

A.2.1 Sway Motion

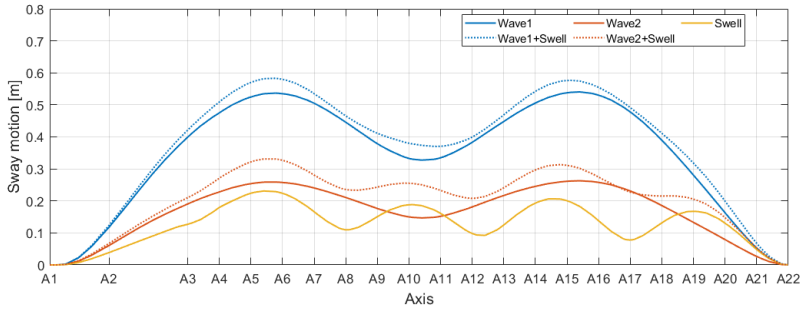

(a) Standard deviation

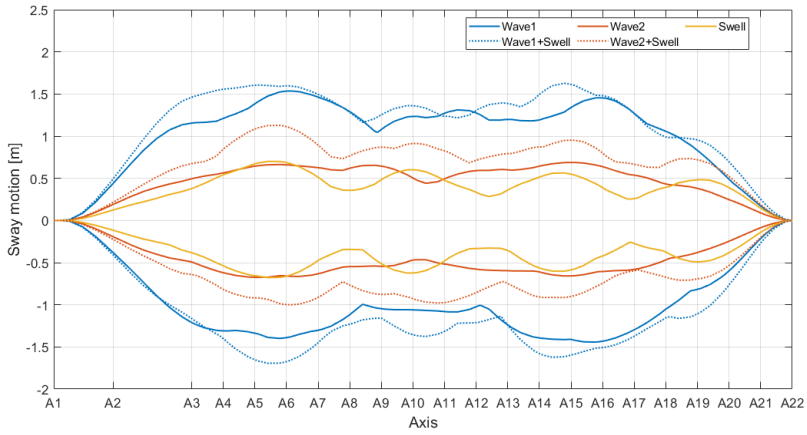

(b) Maximum and minimum

Figure A.3: Statistical properties of sway motion: (a) Standard deviation and (b) Maximum and minimum under different wave conditions.

A.2.2 Strong Axis Bending Moment

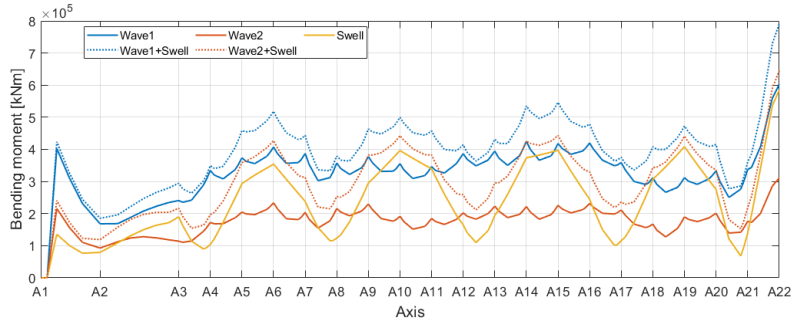

(a) Standard deviation

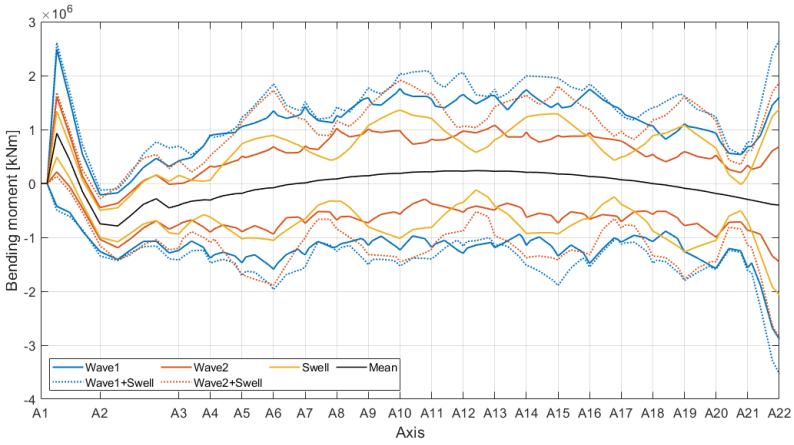

(b) Maximum, minimum and mean

Figure A.4: Statistical properties of strong axis bending moment: (a) Standard deviation and (b) Maximum, minimum and mean under different wave conditions.

A.3 Viscous Effect

A.3.1 Sway Motion

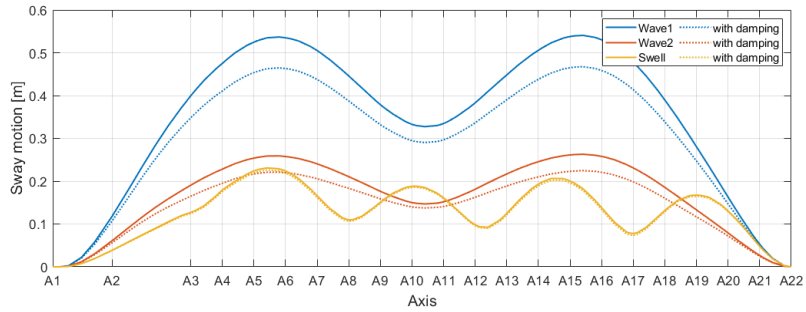

(a) Standard deviation

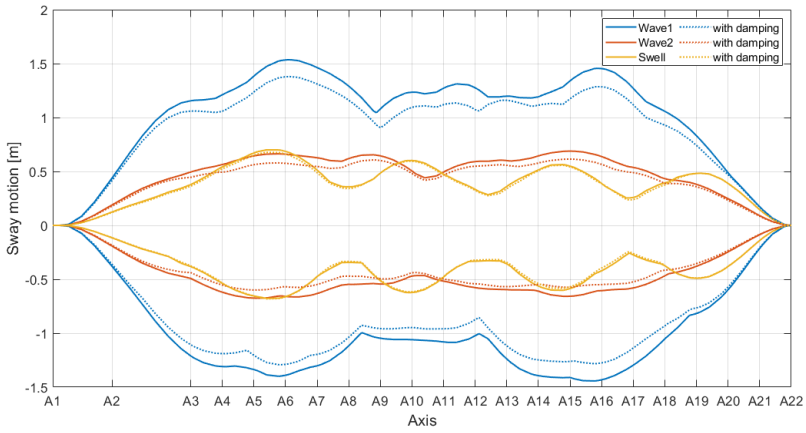

(b) Maximum and minimum

Figure A.5: Statistical properties of sway motion: (a) Standard deviation and (b) Maximum and minimum under different wave conditions.

A.3.2 Strong Axis Bending Moment

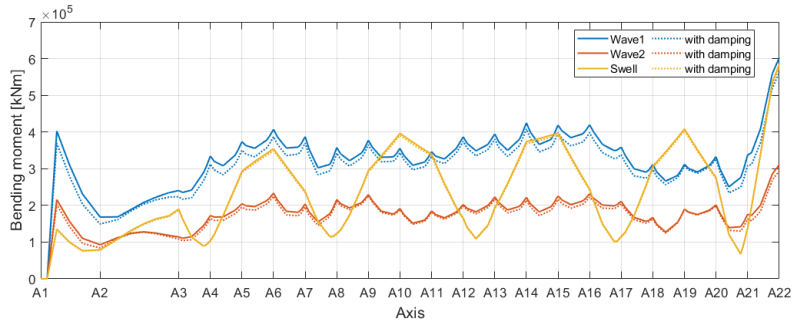

(a) Standard deviation

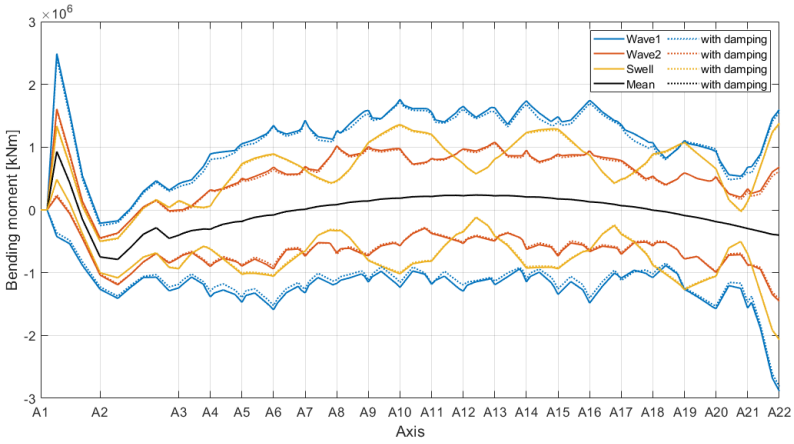

(b) Maximum, minimum and mean

Figure A.6: Statistical properties of strong axis bending moment: (a) Standard deviation and (b) Maximum, minimum and mean under different wave conditions.

Appendix B

Global Dynamic Responses

B.1 Torsional Moment

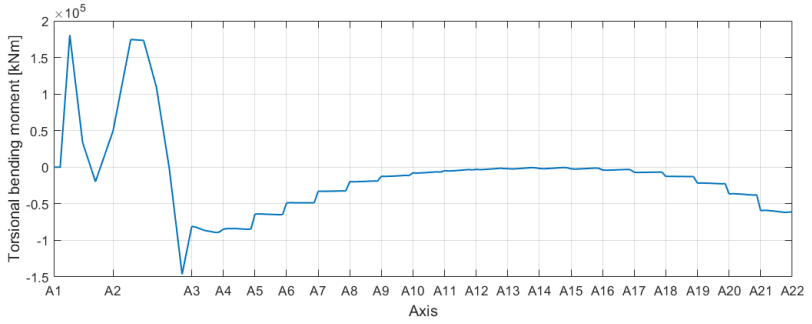

(a) Static mean

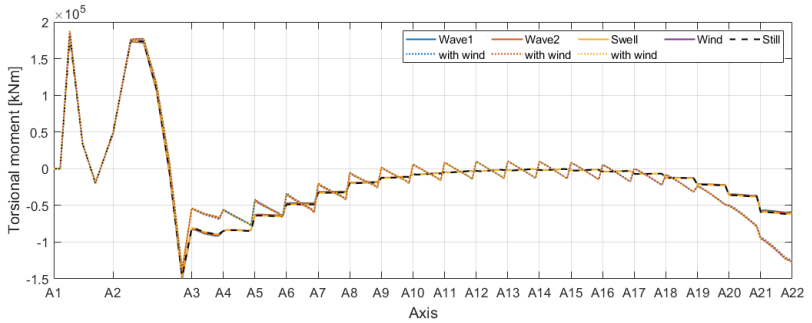

(b) Dynamic mean

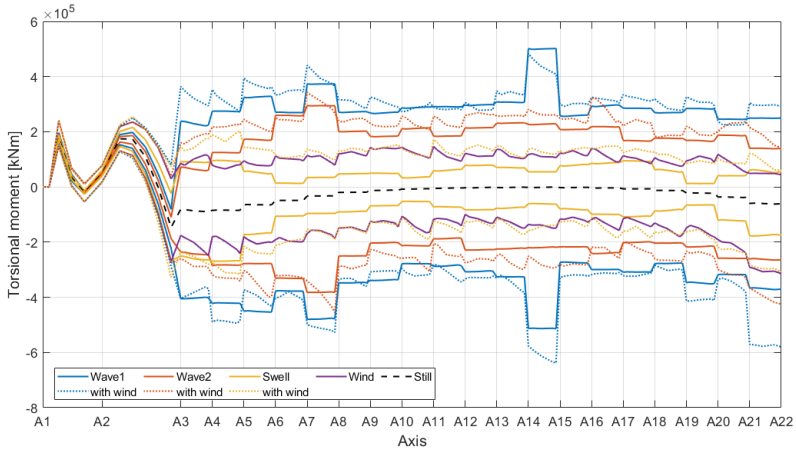

(c) Maximum and minimum

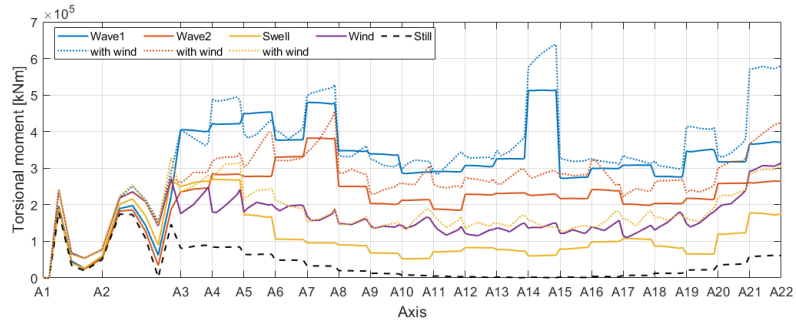

(d) Absolute maximum magnitude

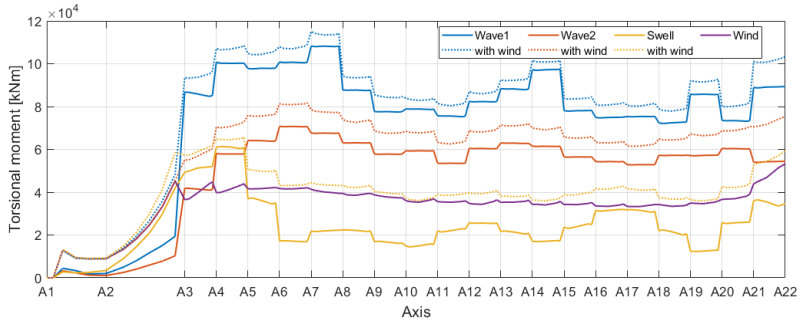

(e) Standard deviation

Figure B.1: Statistical properties of torsional moment: (a) Static mean, (b) Dynamic mean, (c) Maximum and minimum, (d) Absolute maximum magnitude, and (e) Standard deviation under different conditions.

B.2 Shear Force in the Local Y-direction

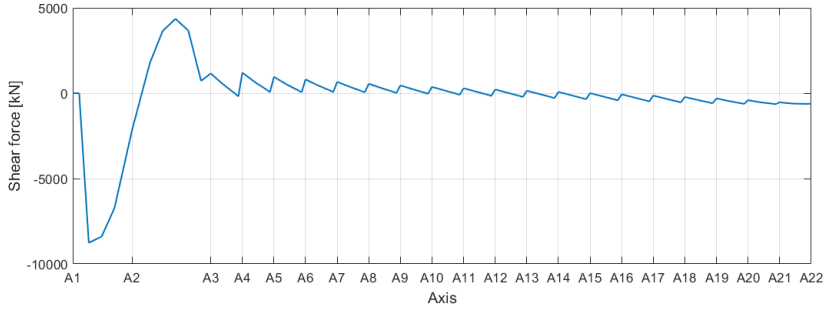

(a) Static mean

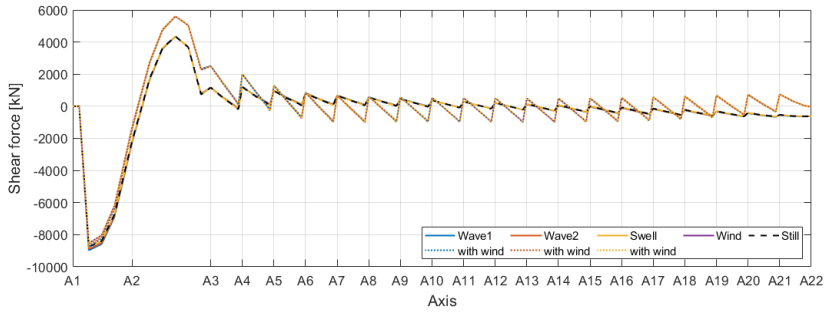

(b) Dynamic mean

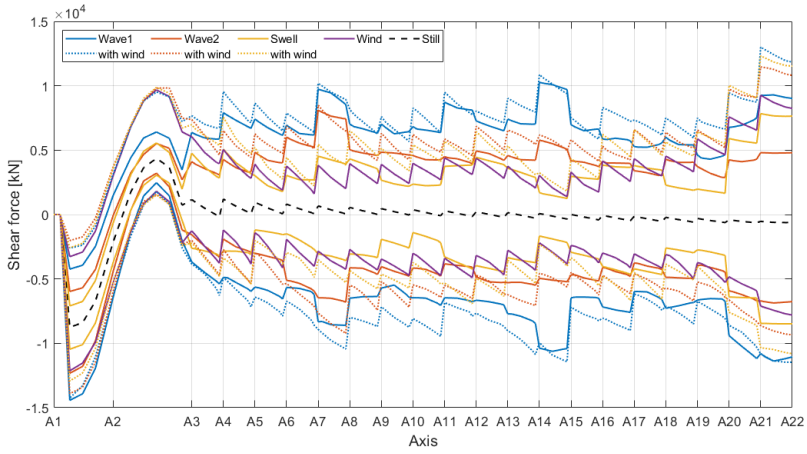

(c) Maximum and minimum

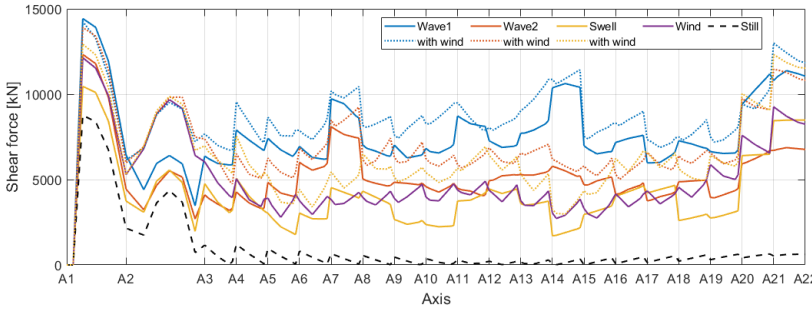

(d) Absolute maximum magnitude

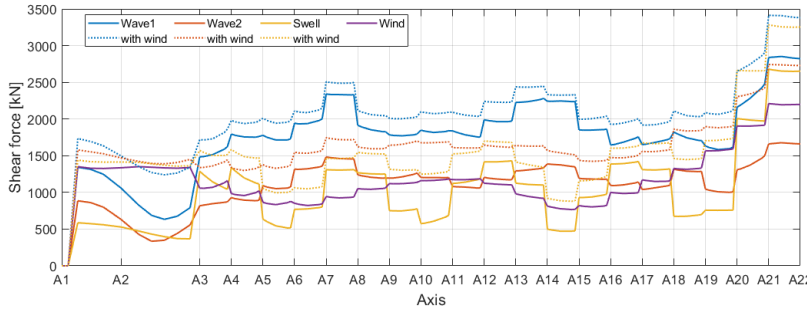

(e) Standard deviation

Figure B.2: Statistical properties of shear force in the local y-direction: (a) Static mean, (b) Dynamic mean, (c) Maximum and minimum, (d) Absolute maximum magnitude, and (e) Standard deviation under different conditions.

B.3 Shear Force in the Local Z-direction

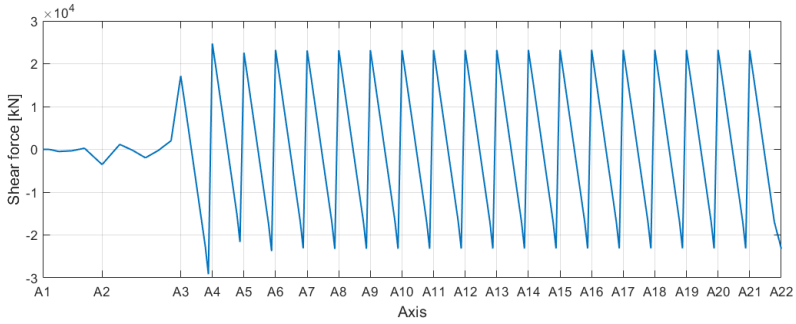

(a) Static mean

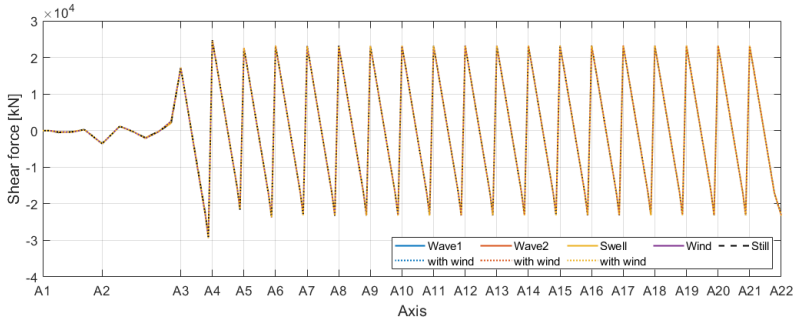

(b) Dynamic mean

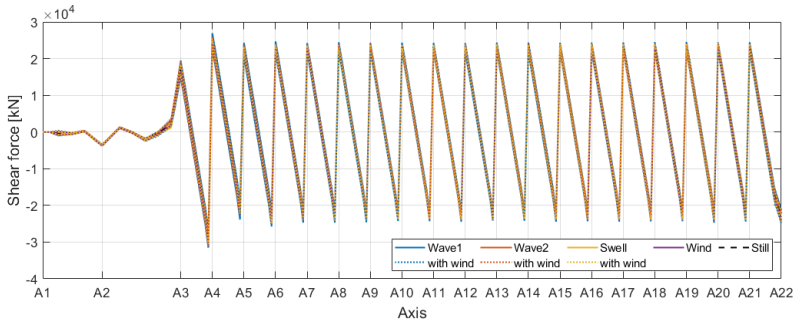

(c) Maximum and minimum

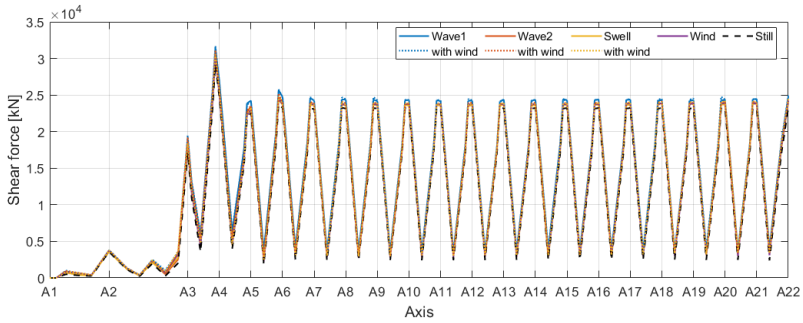

(d) Absolute maximum magnitude

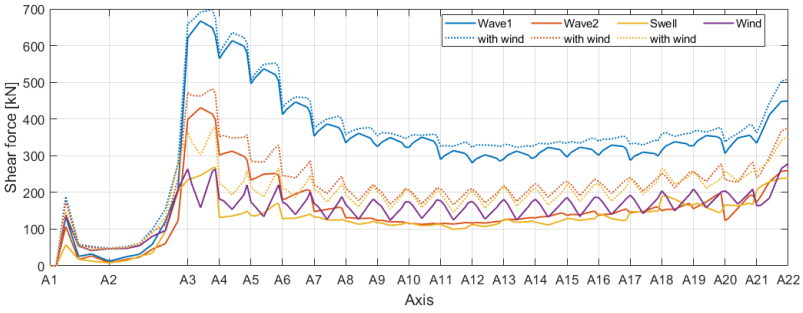

(e) Standard deviation

Figure B.3: Statistical properties of shear force in the local z-direction: (a) Static mean, (b) Dynamic mean, (c) Maximum and minimum, (d) Absolute maximum magnitude, and (e) Standard deviation under different conditions.

B.4 Static and Dynamic Contributions

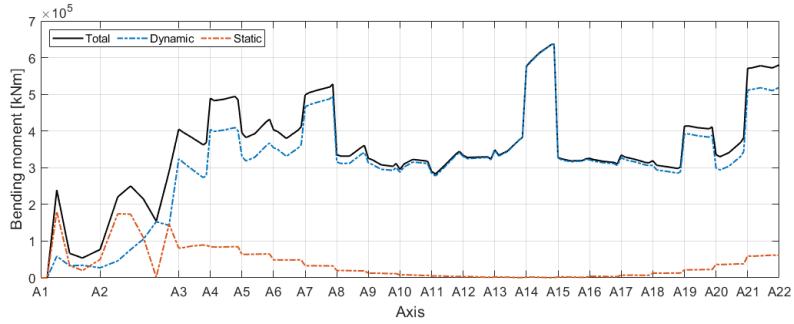

(a) Torsional bending moment

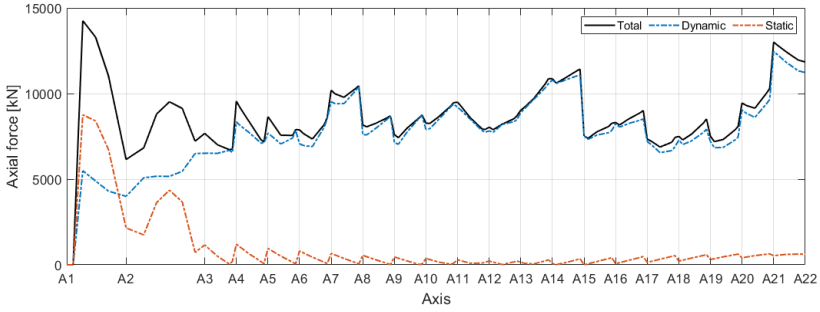

(b) Shear force in the local y-axis

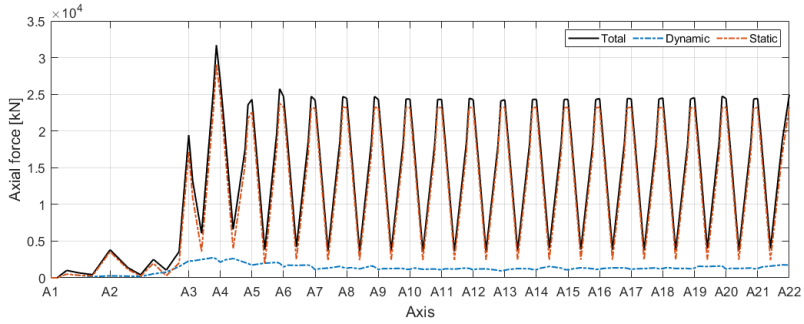

(c) Shear force in the local z-axis

Figure B.4: Static and dynamic contributions for structural responses: (a) Torsional moment, (b) Shear force in the local y-direction, and (c) Shear force in the local z-direction.

Appendix C

Stress Analysis Results

C.1 Stress Observation Points

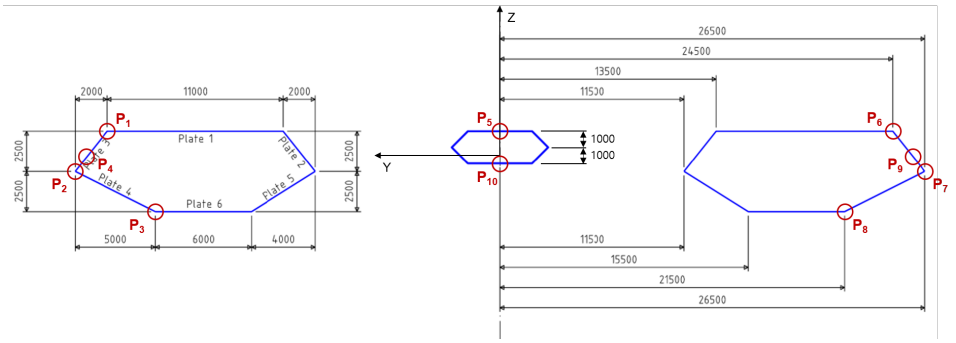

Figure C.1: Stress points in the section of the high bridge girder.

- $P_1\,(y\ ,\ z) = (24.5\ ,\ 1.5)$
- $P_2\,(y\ ,\ z) = (26.5\ ,\ -1.0)$
- $P_3\,(y\ ,\ z) = (21.5\ ,\ -3.5)$
- $P_4\,(y\ ,\ z) = (25.7\ ,\ 0)$
- $P_5\,(y\ ,\ z) = (0\ ,\ 1.5)$
- $P_6\,(y\ ,\ z) = (-24.5\ ,\ 1.5)$
- $P_7\,(y\ ,\ z) = (-26.5\ ,\ -1.0)$
- $P_8\,(y\ ,\ z) = (-21.5\ ,\ -3.5)$
- $P_9\,(y\ ,\ z) = (-25.7\ ,\ 0)$
- $P_{10}\,(y\ ,\ z) = (0\ ,\ -0.5)$

C.2 Static Bridge Girder Stress

C.2.1 Still Water Condition

Mean Stress

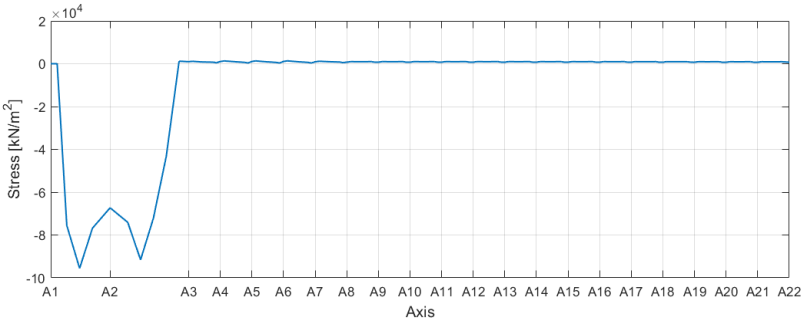

(a) Mean stress due to axial force

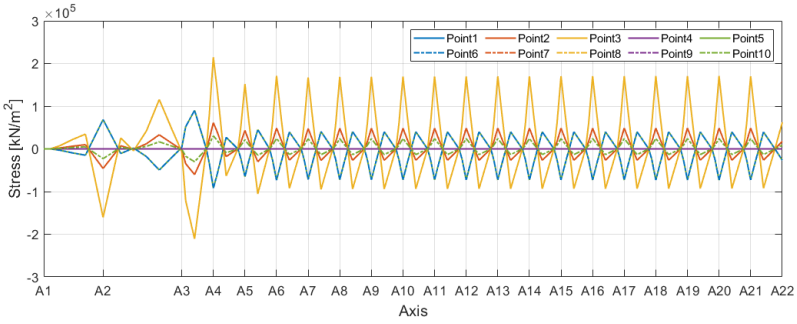

(b) Mean stress due to weak axis bending moment

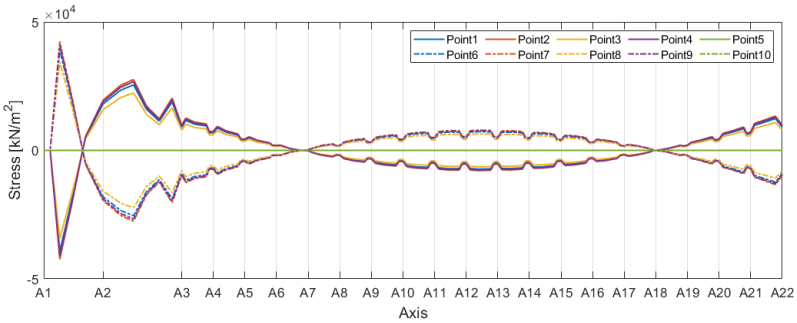

(c) Mean stress due to strong axis bending moment

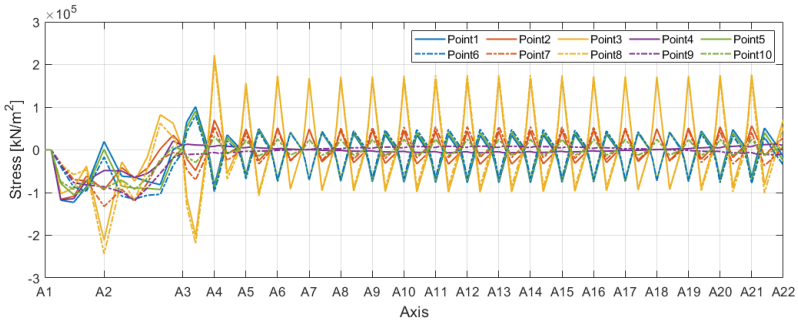

(d) Total mean stress

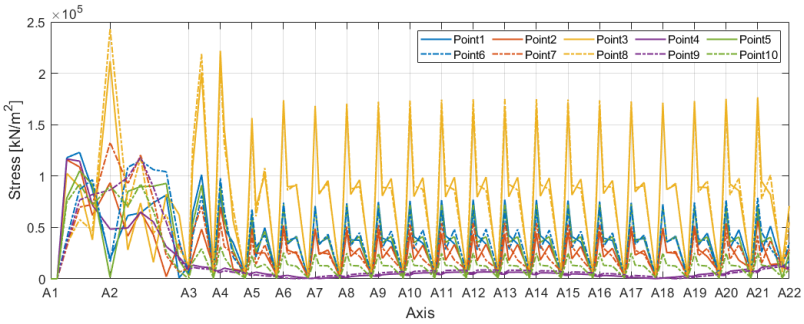

(e) Absolute total mean stress

Figure C.2: The components and total of the bridge girder mean stress at different points under the still water condition: (a) Mean stress due to axial force, (b) Mean stress due to weak axis bending moment, (c) Mean stress due to strong axis bending moment, (d) Total mean stress, and (e) Absolute total mean stress.

Mean Stress Contributions at Different Points

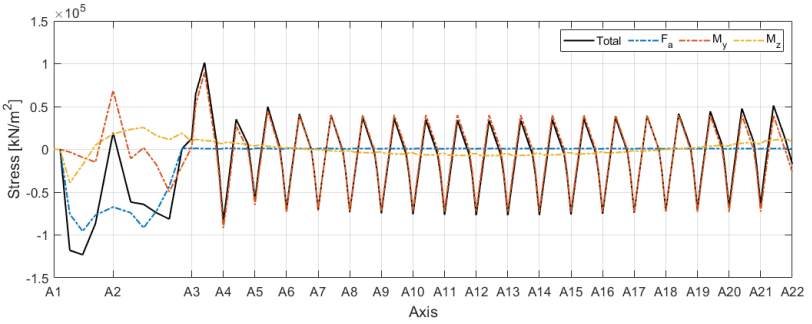

(a) Point 1

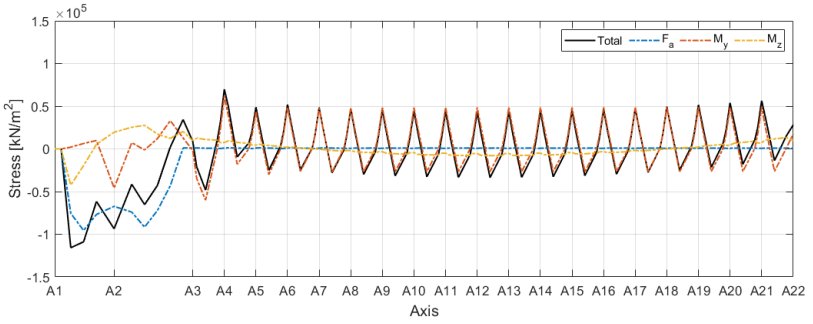

(b) Point 2

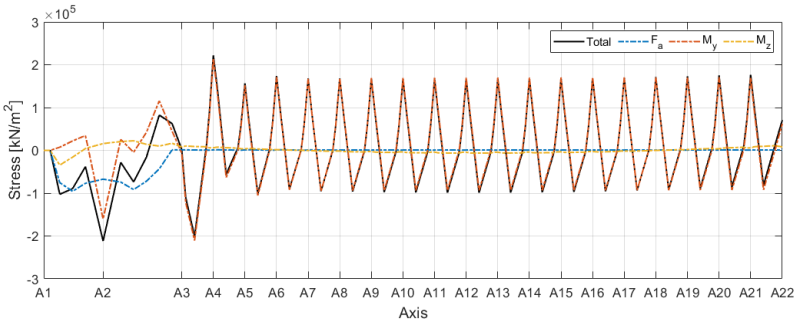

(c) Point 3

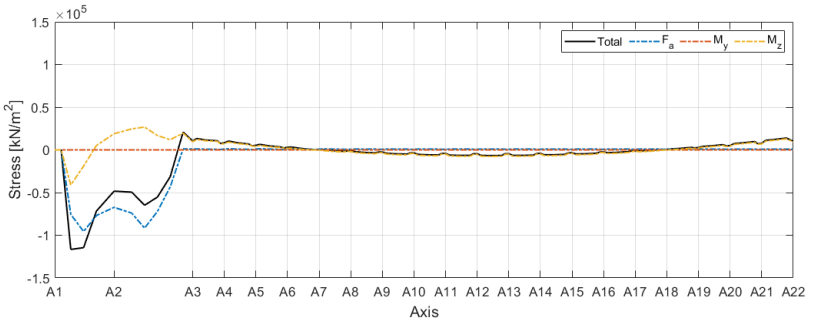

(d) Point 4

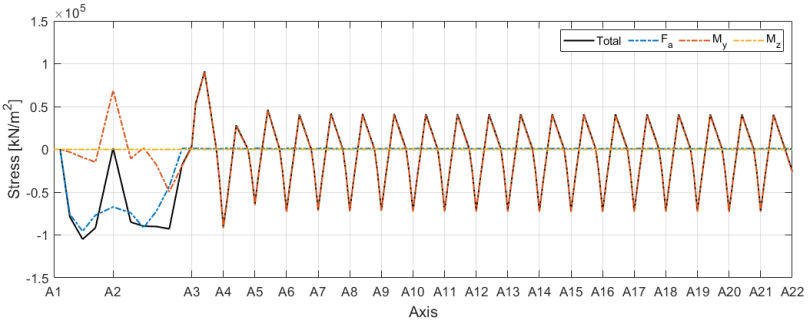

(e) Point 5

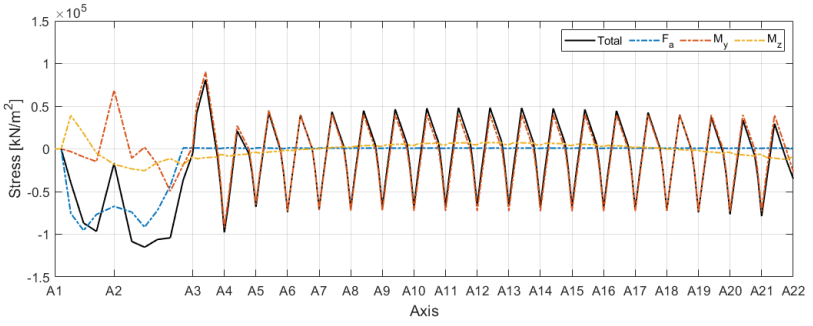

(f) Point 6

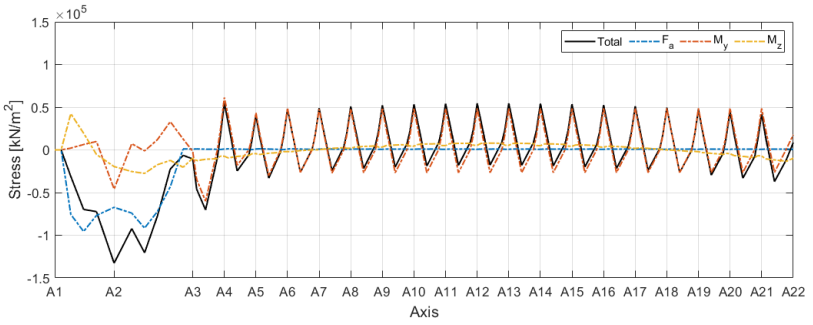

(g) Point 7

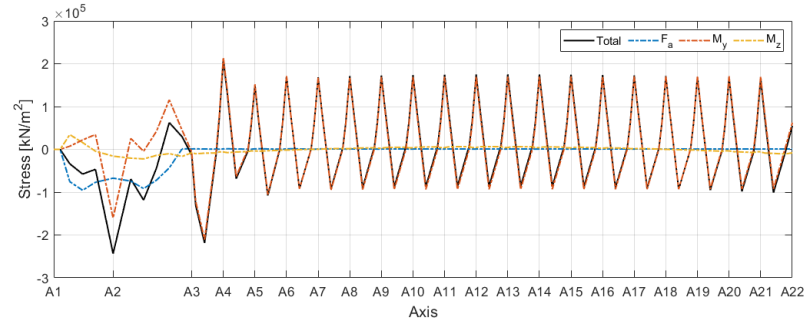

(h) Point 8

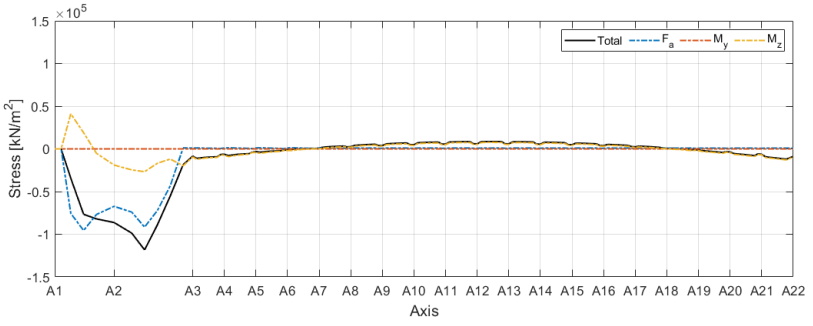

(i) Point 9

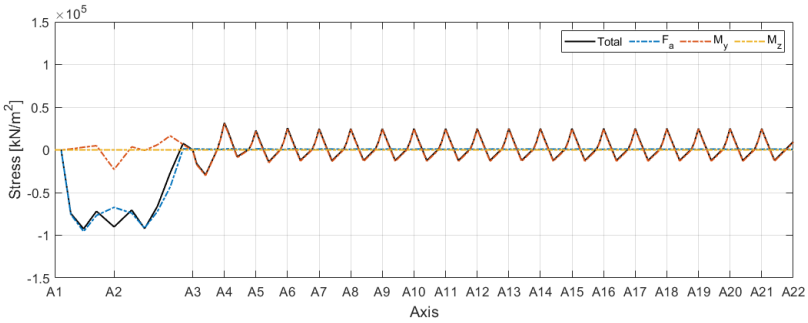

(j) Point 10

Figure C.3: The contributions of the bridge girder mean stress under still water condition at different points: (a) Point 1, (b) Point 2, (c) Point 3, (d) Point 4, (e) Point 5, (f) Point 6, (g) Point 7, (h) Point 8, (i) Point 9, and (j) Point 10.

C.3 Dynamic Bridge Girder Stress

C.3.1 Wave 1 Condition

Mean Stress

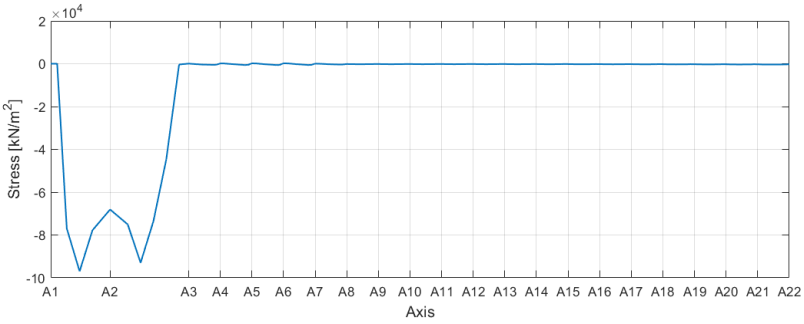

(a) Mean stress due to axial force

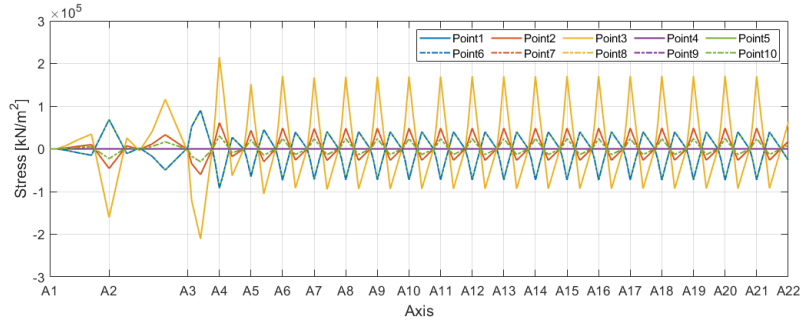

(b) Mean stress due to weak axis bending moment

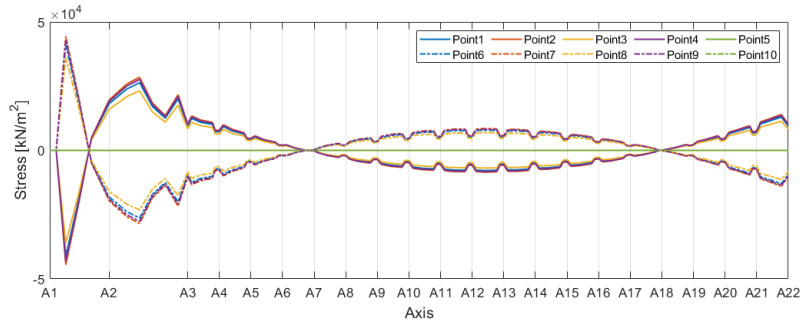

(c) Mean stress due to strong axis bending moment

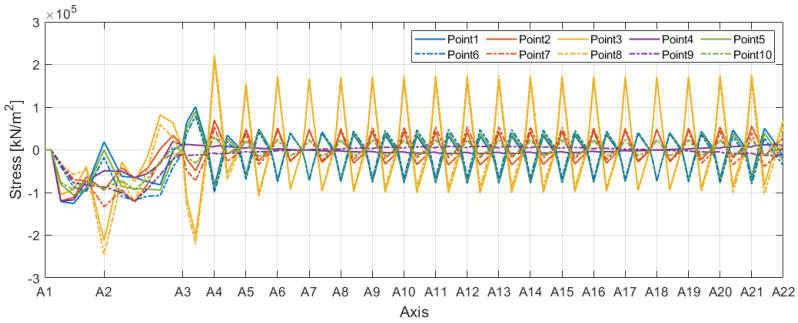

(d) Total mean stress

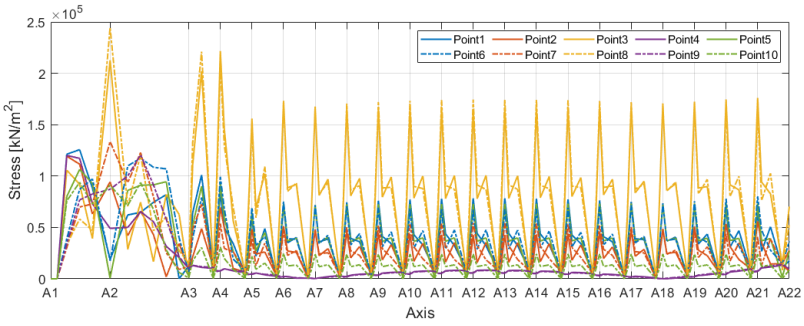

(e) Absolute total mean stress

Figure C.4: The components and total of the bridge girder mean stress at different points under the wave 1 condition: (a) Mean stress due to axial force, (b) Mean stress due to weak axis bending moment, (c) Mean stress due to strong axis bending moment, (d) Total mean stress, and (e) Absolute total mean stress.

Mean Stress Contributions at Different Points

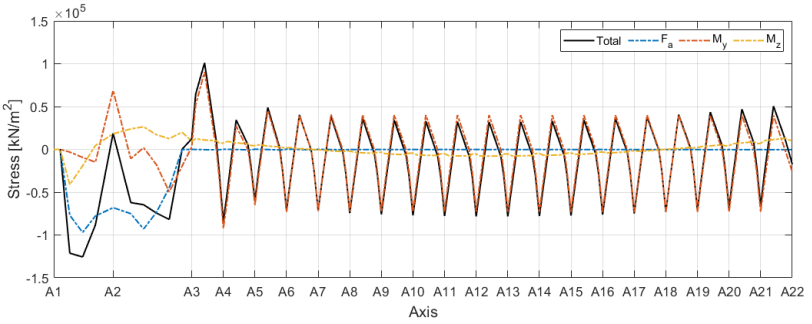

(a) Point 1

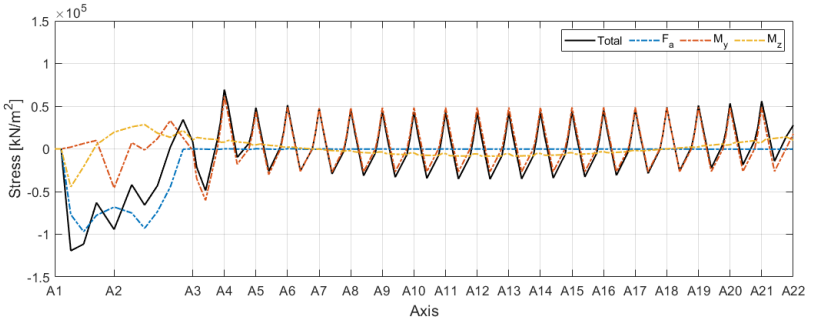

(b) Point 2

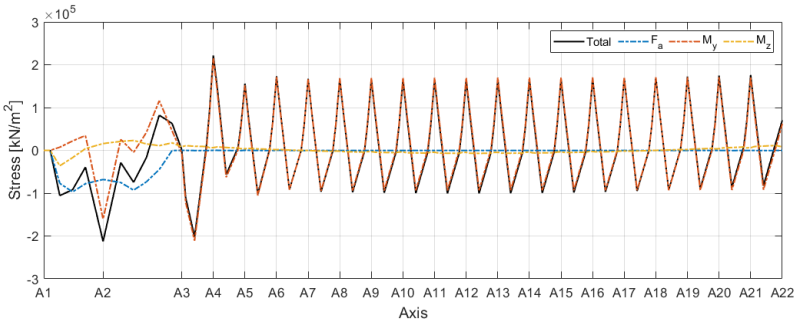

(c) Point 3

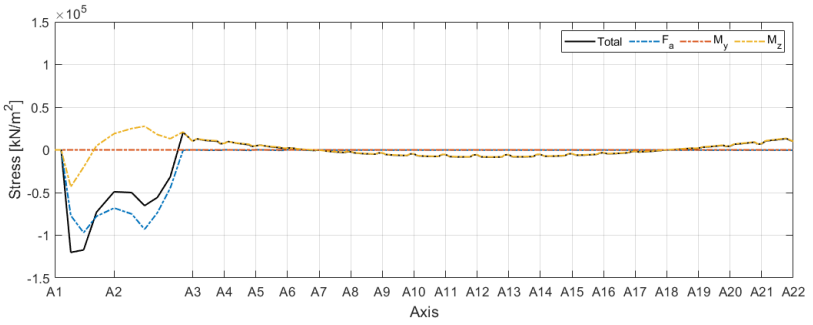

(d) Point 4

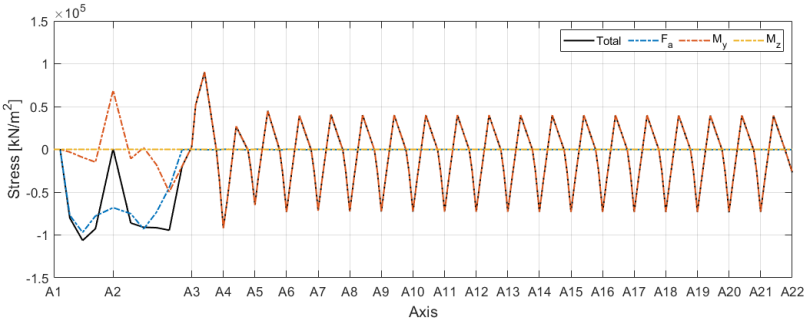

(e) Point 5

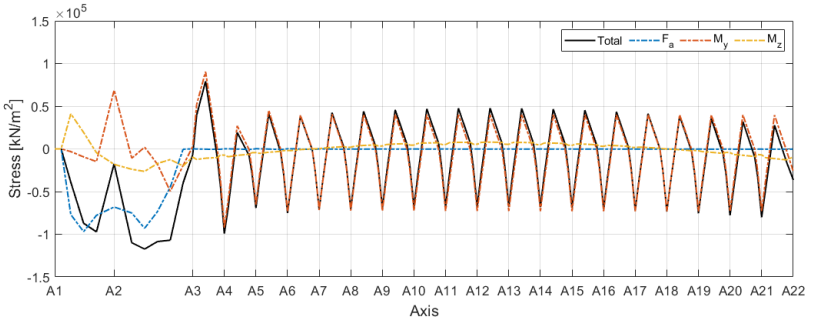

(f) Point 6

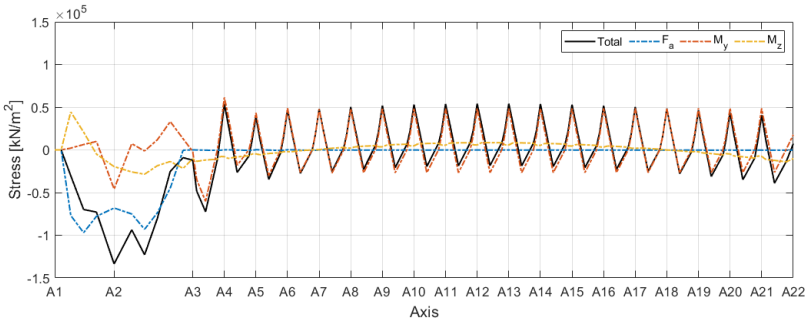

(g) Point 7

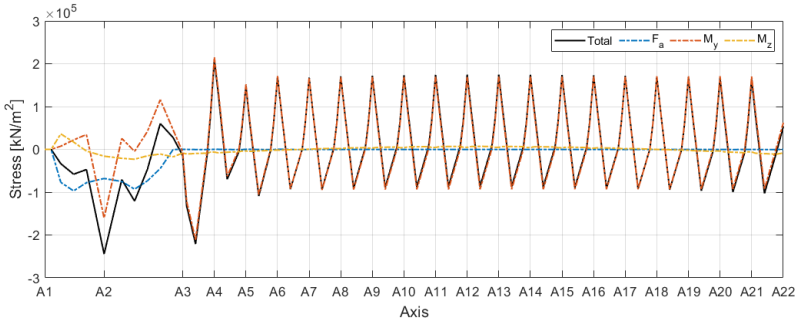

(h) Point 8

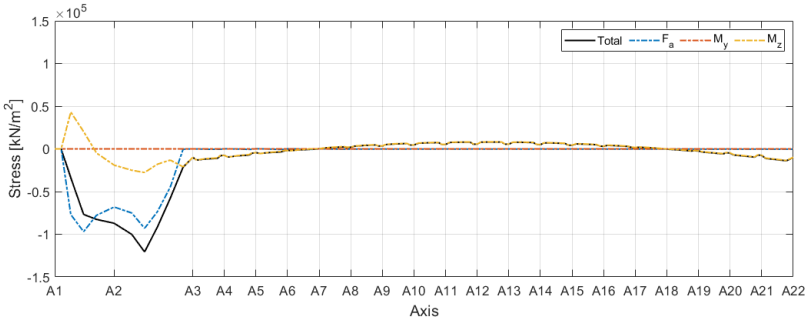

(i) Point 9

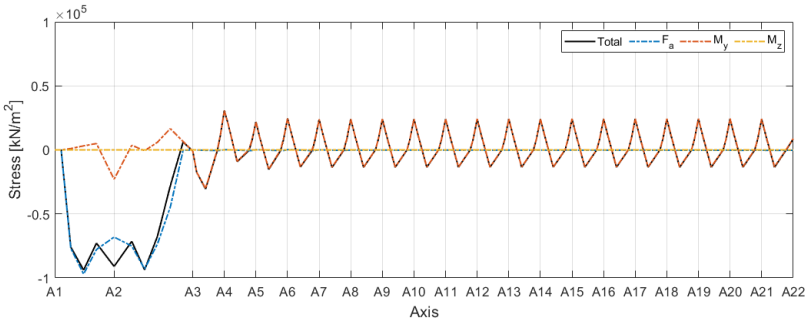

(j) Point 10

Figure C.5: The contributions of the bridge girder mean stress under wave 1 condition at different points: (a) Point 1, (b) Point 2, (c) Point 3, (d) Point 4, (e) Point 5, (f) Point 6, (g) Point 7, (h) Point 8, (i) Point 9, and (j) Point 10.

Standard Deviation

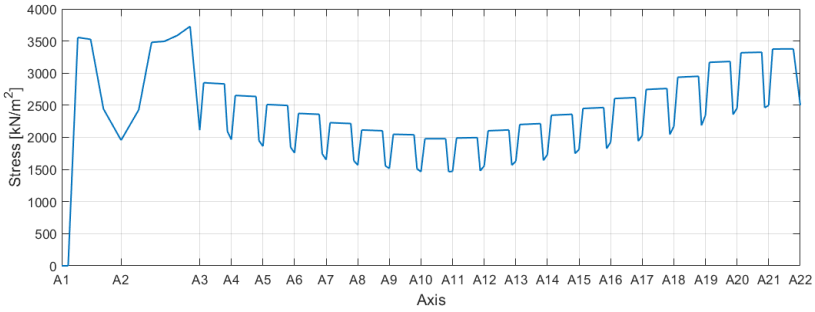

(a) Std of stress due to axial force

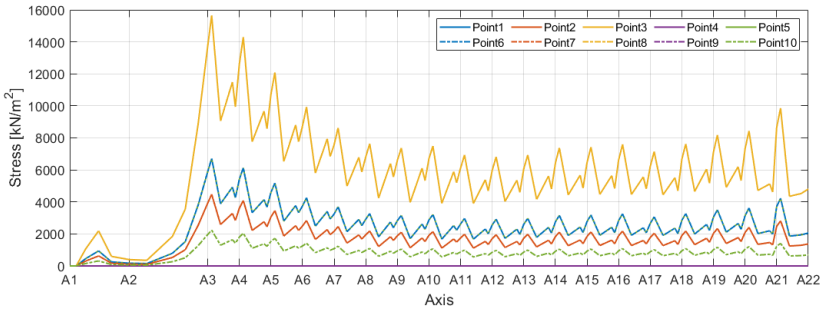

(b) Std of stress due to weak axis bending moment

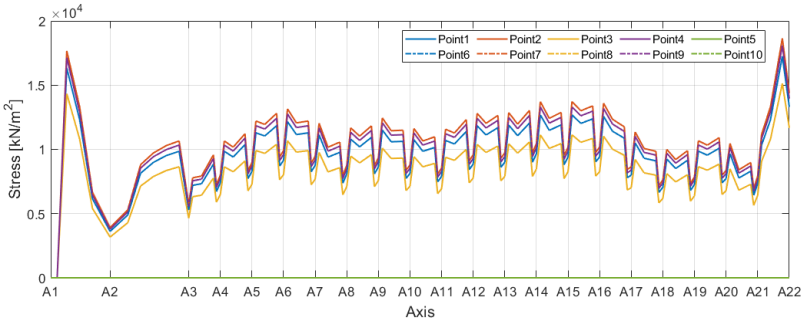

(c) Std of stress due to strong axis bending moment

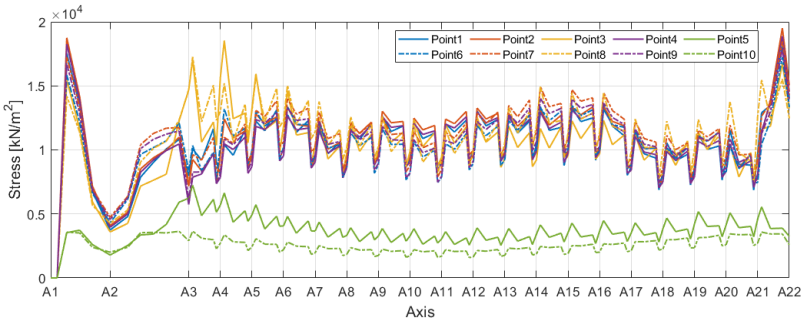

(d) Std of total stress

Figure C.6: The standard deviation of the components and total bridge girder stress at different points under the wave 1 condition: (a) Std of stress due to axial force, (b) Std of stress due to weak axis bending moment, (c) Std of stress due to strong axis bending moment, and (d) Std of total stress.

Standard Deviation Contributions at Different Points

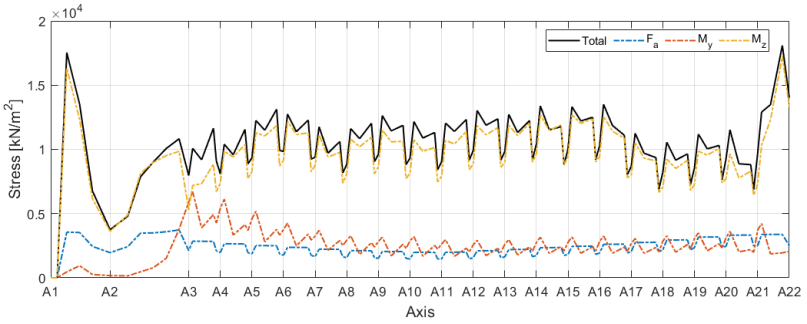

(a) Point 1

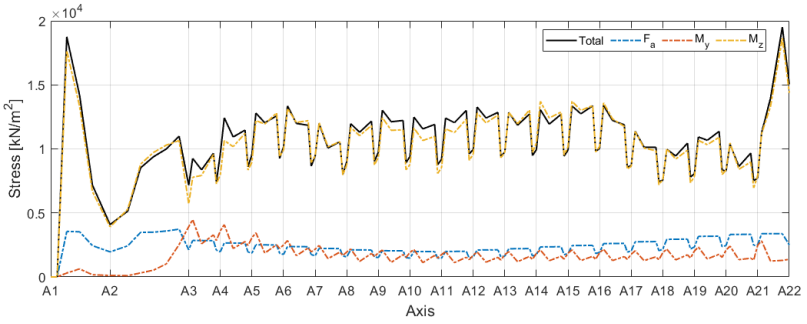

(b) Point 2

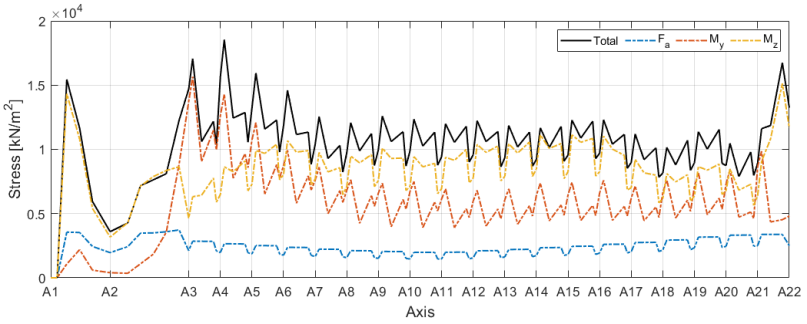

(c) Point 3

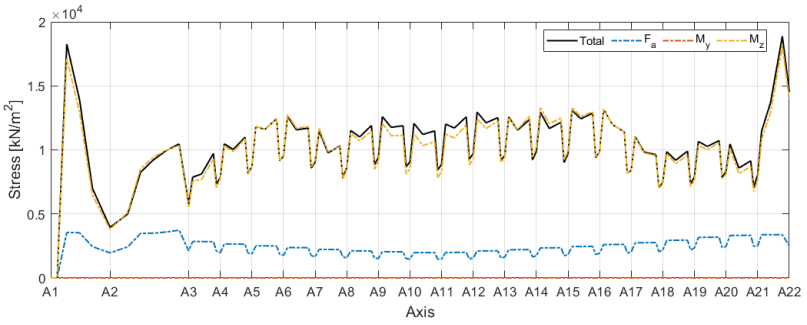

(d) Point 4

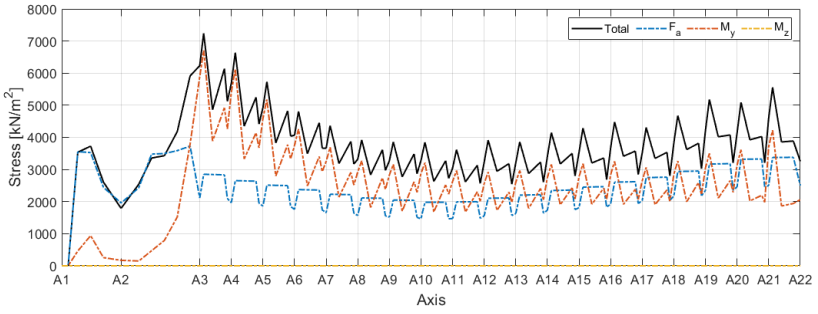

(e) Point 5

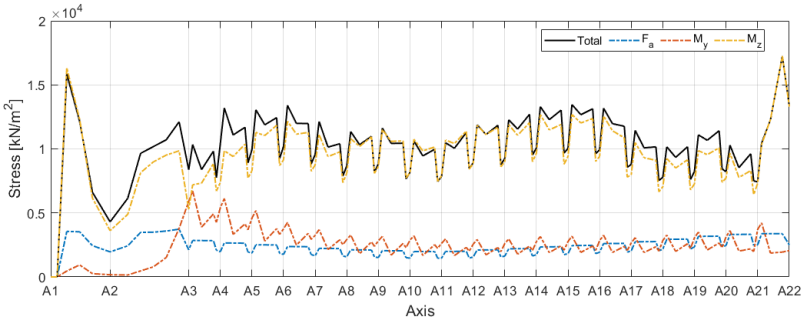

(f) Point 6

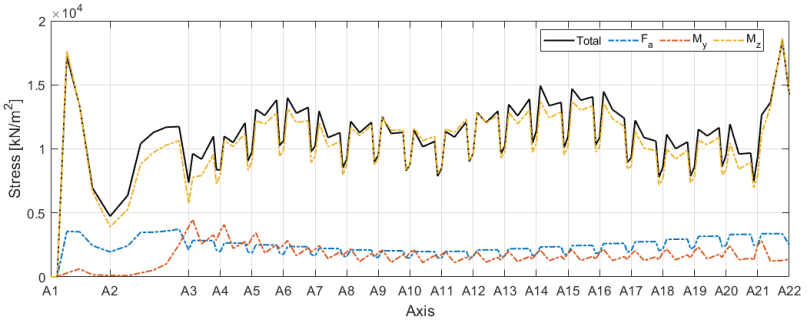

(g) Point 7

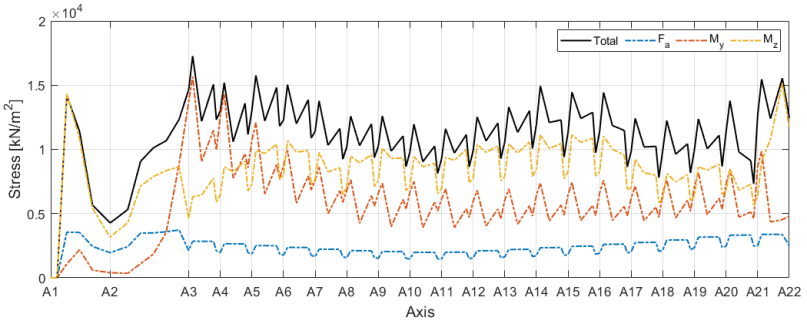

(h) Point 8

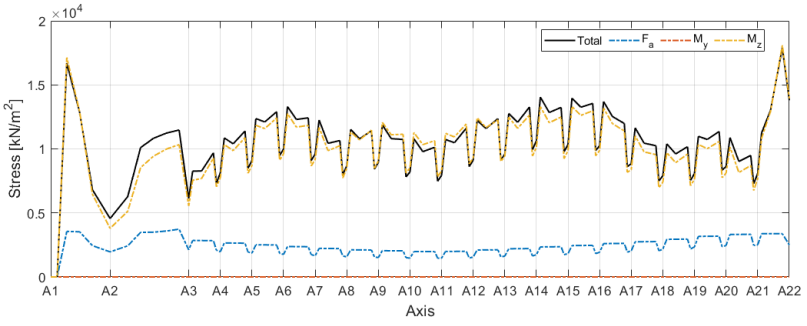

(i) Point 9

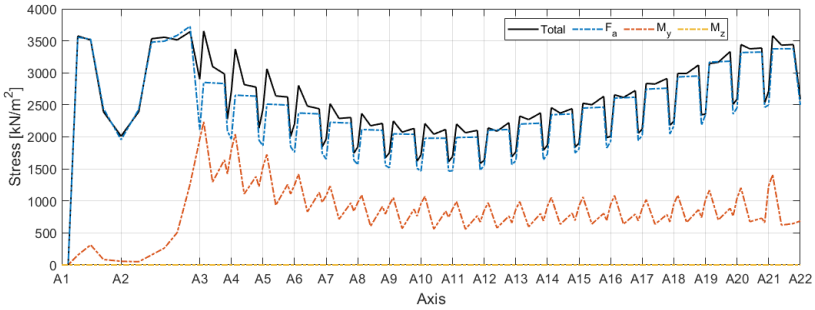

(j) Point 10

Figure C.7: The contributions of the standard deviation of the bridge girder stress under wave 1 condition at different points: (a) Point 1, (b) Point 2, (c) Point 3, (d) Point 4, (e) Point 5, (f) Point 6, (g) Point 7, (h) Point 8, (i) Point 9, and (j) Point 10.

C.3.2 Wind Condition

Mean Stress

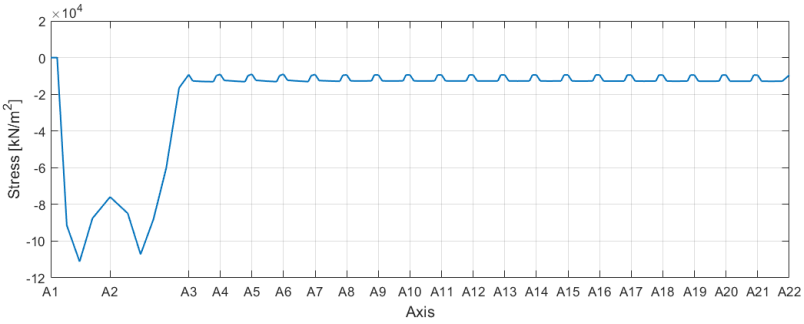

(a) Mean stress due to axial force

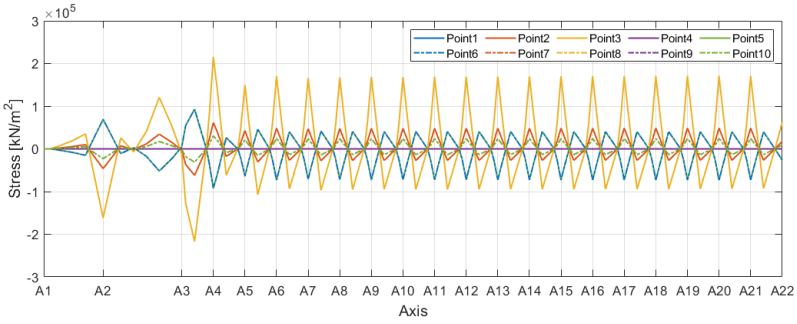

(b) Mean stress due to weak axis bending moment

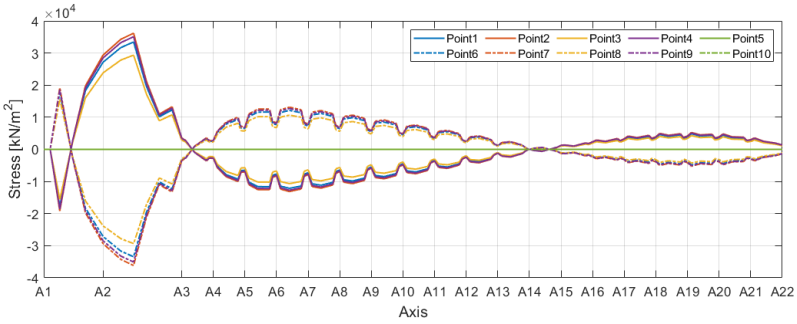

(c) Mean stress due to strong axis bending moment

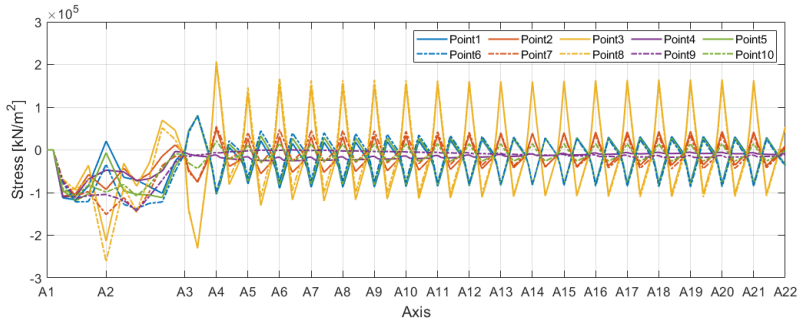

(d) Total mean stress

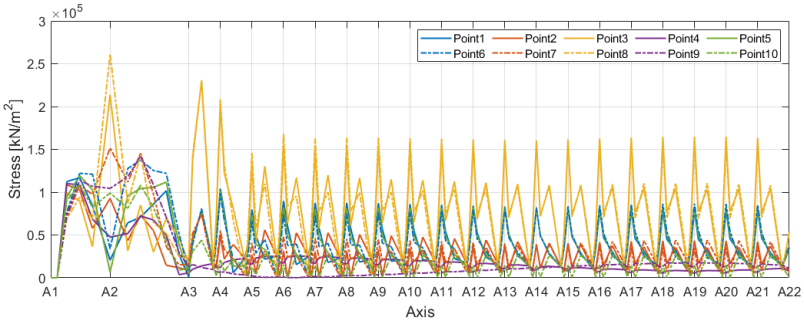

(e) Absolute total mean stress

Figure C.8: The components and total of the bridge girder mean stress at different points under wind condition: (a) Mean stress due to axial force, (b) Mean stress due to weak axis bending moment, (c) Mean stress due to strong axis bending moment, (d) Total mean stress, and (e) Absolute total mean stress.

Mean Stress Contributions at Different Points

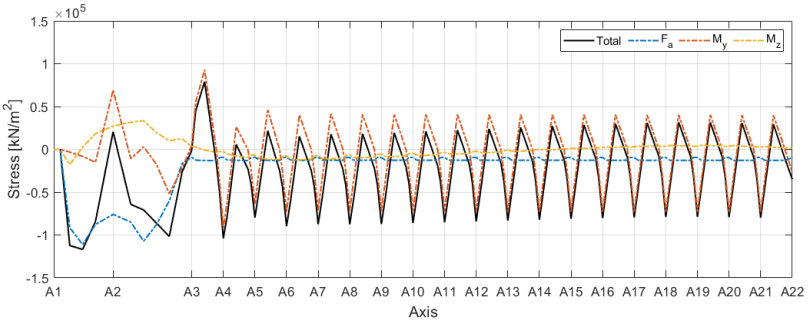

(a) Point 1

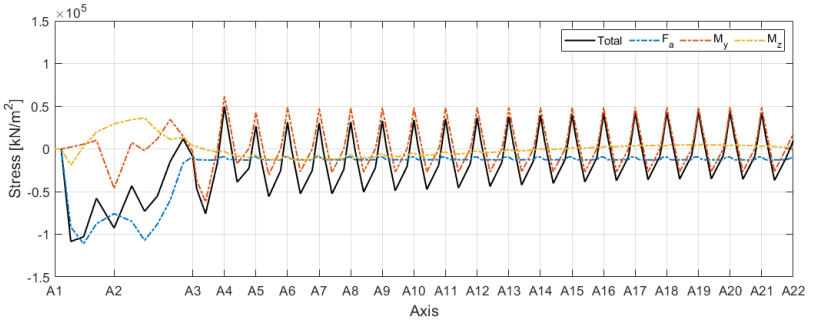

(b) Point 2

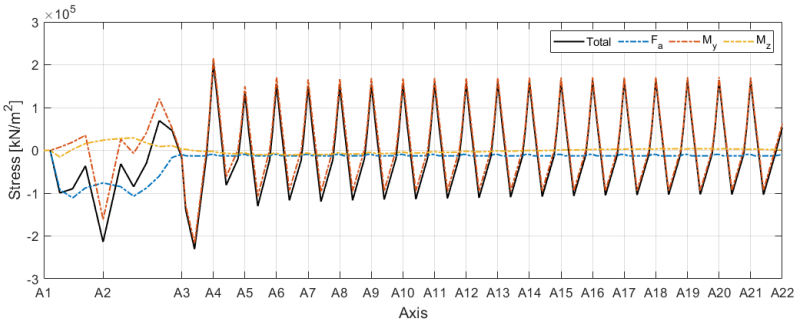

(c) Point 3

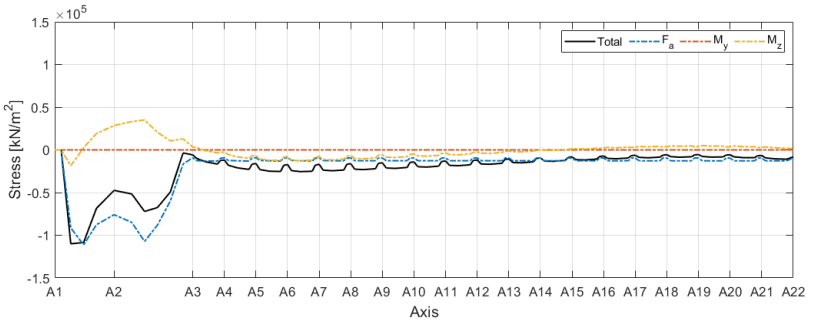

(d) Point 4

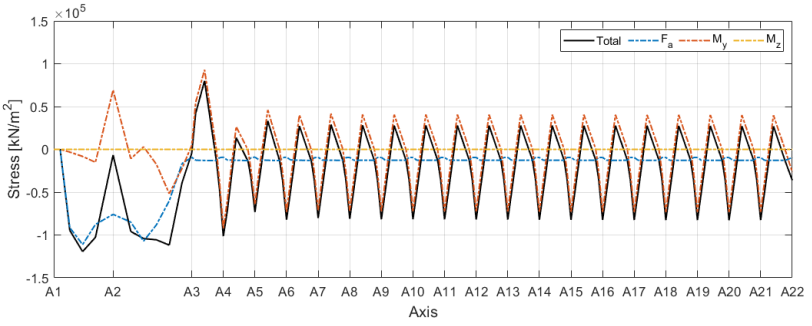

(e) Point 5

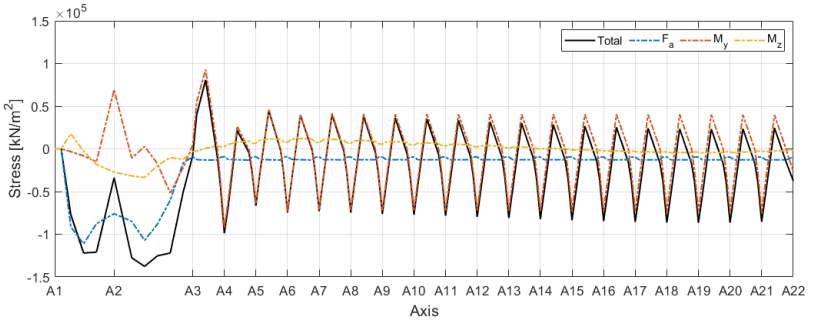

(f) Point 6

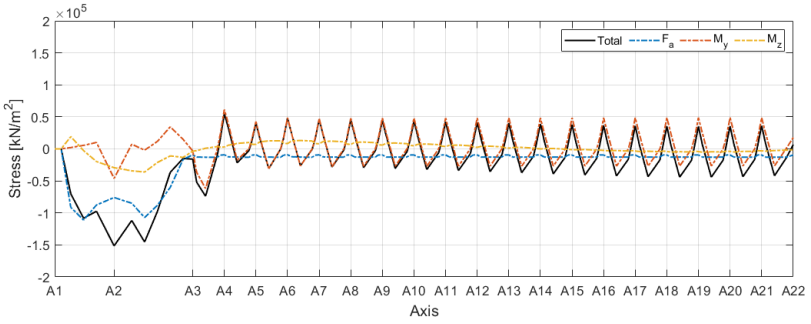

(g) Point 7

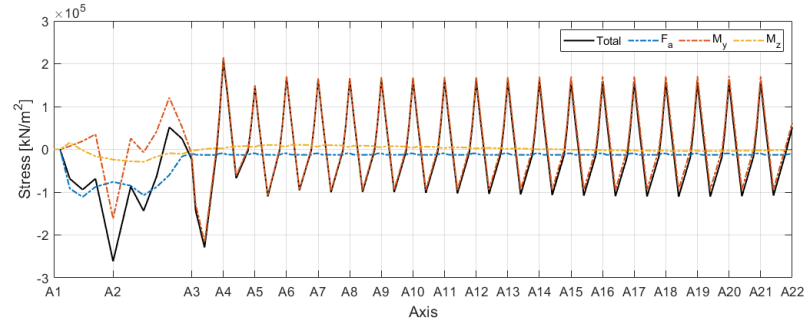

(h) Point 8

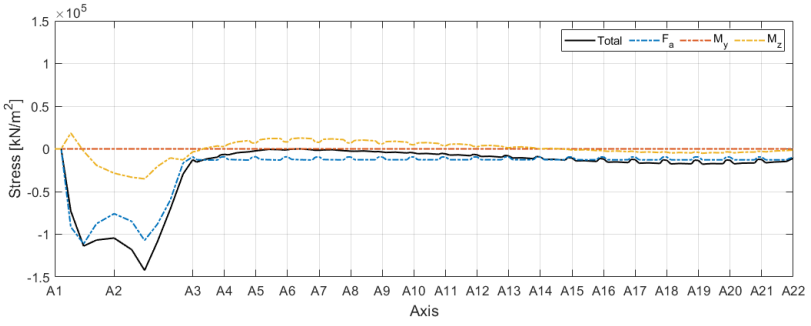

(i) Point 9

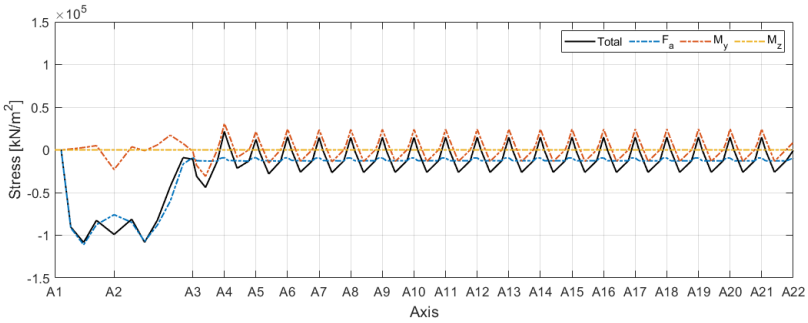

(j) Point 10

Figure C.9: The contributions of the bridge girder mean stress under wind condition at different points: (a) Point 1, (b) Point 2, (c) Point 3, (d) Point 4, (e) Point 5, (f) Point 6, (g) Point 7, (h) Point 8, (i) Point 9, and (j) Point 10.

Standard Deviation

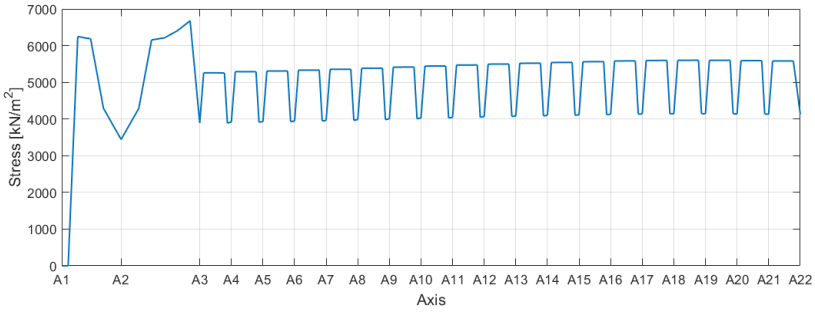

(a) Std of stress due to axial force

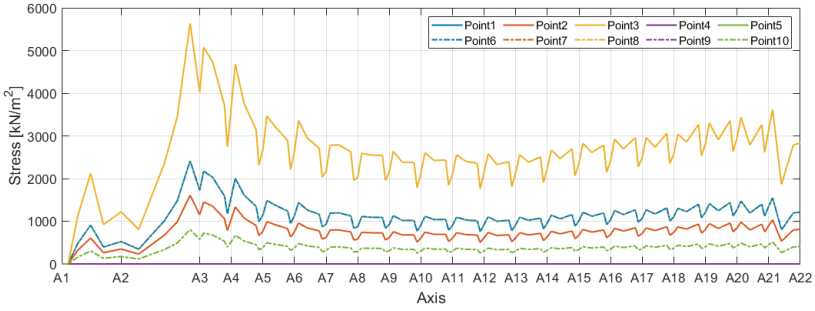

(b) Std of stress due to weak axis bending moment

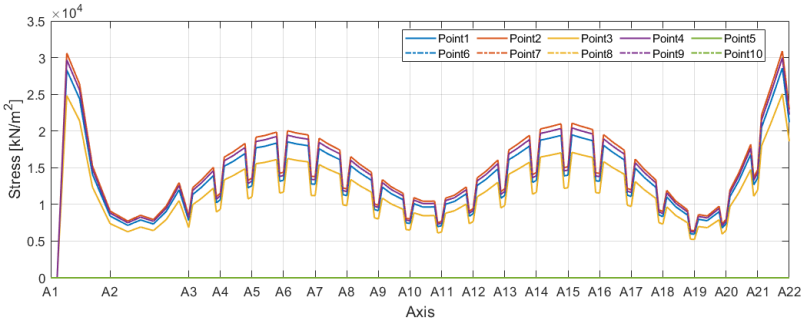

(c) Std of stress due to strong axis bending moment

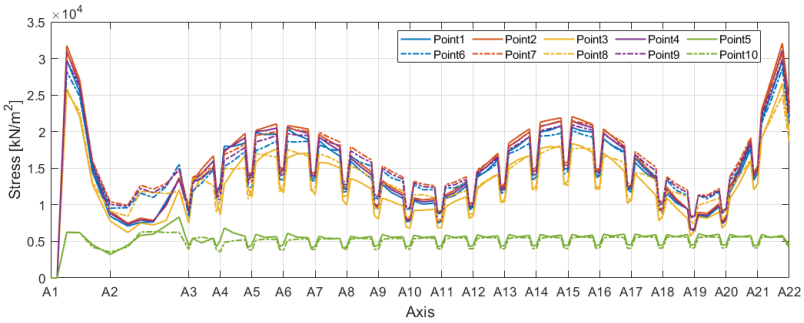

(d) Std of total stress

Figure C.10: The standard deviation of the components and total bridge girder stress at different points under wind condition: (a) Std of stress due to axial force, (b) Std of stress due to weak axis bending moment, (c) Std of stress due to strong axis bending moment, and (d) Std of total stress.

Standard Deviation Contributions at Different Points

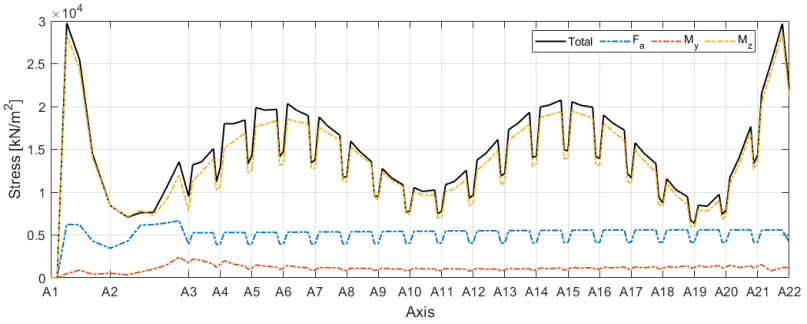

(a) Point 1

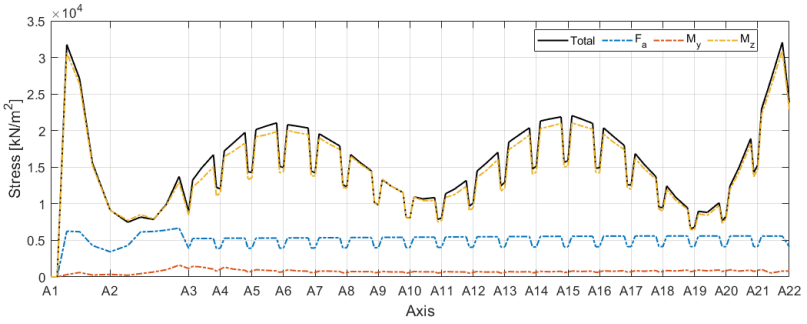

(b) Point 2

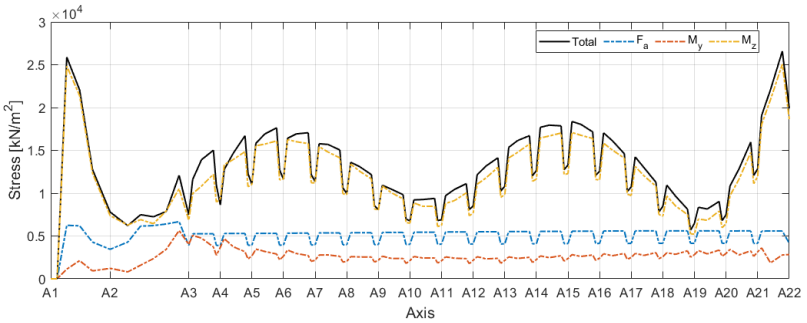

(c) Point 3

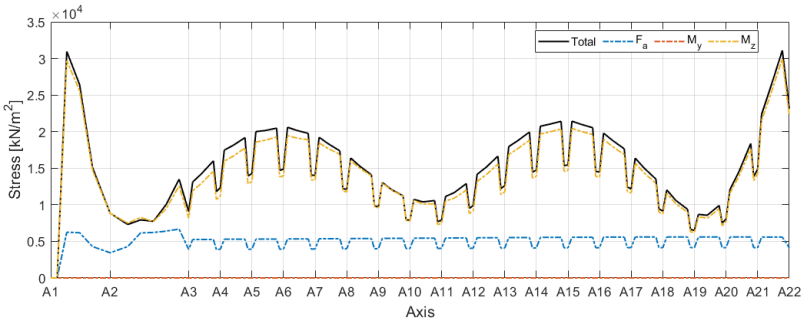

(d) Point 4

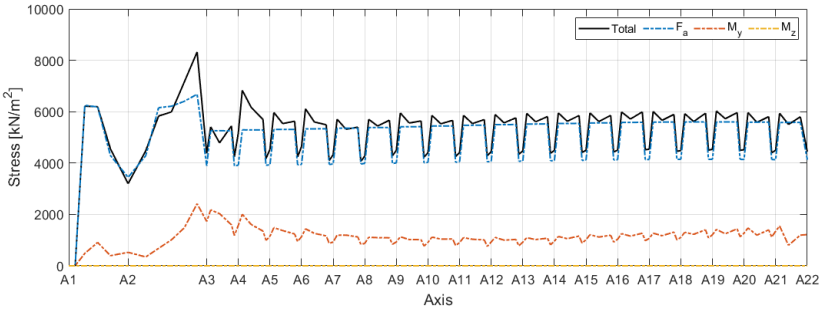

(e) Point 5

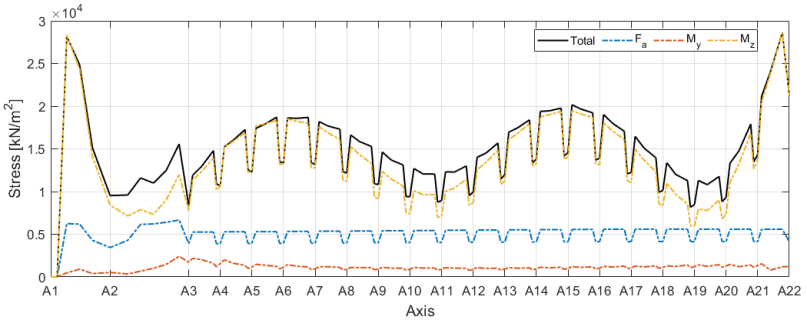

(f) Point 6

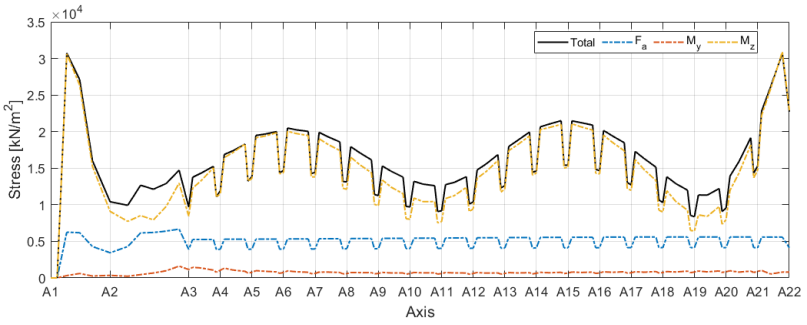

(g) Point 7

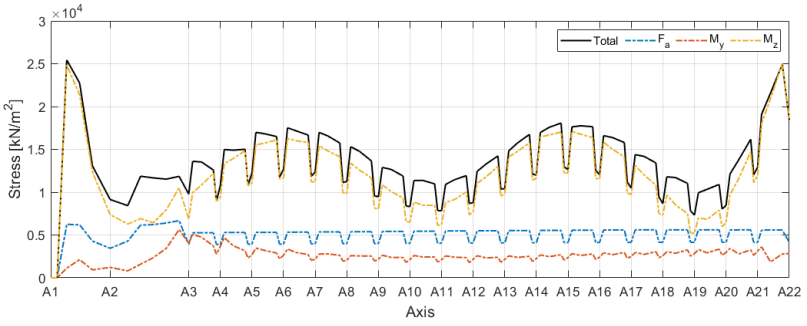

(h) Point 8

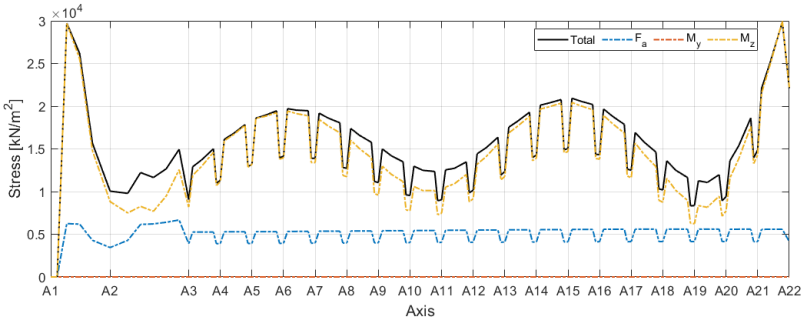

(i) Point 9

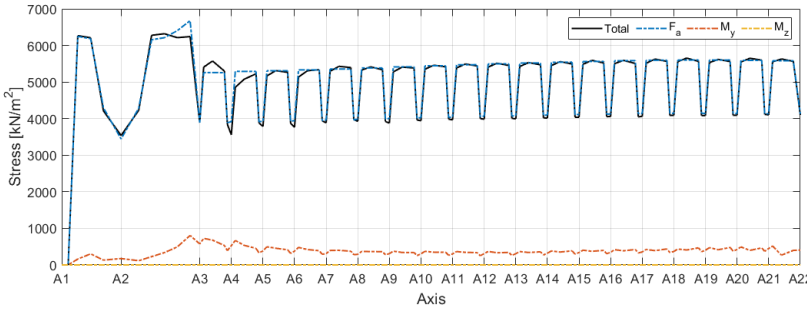

(j) Point 10

Figure C.11: The contributions of the standard deviation of the bridge girder stress under wind condition at different points: (a) Point 1, (b) Point 2, (c) Point 3, (d) Point 4, (e) Point 5, (f) Point 6, (g) Point 7, (h) Point 8, (i) Point 9, and (j) Point 10.

C.3.3 Wave 1 with Wind Condition

Mean Stress

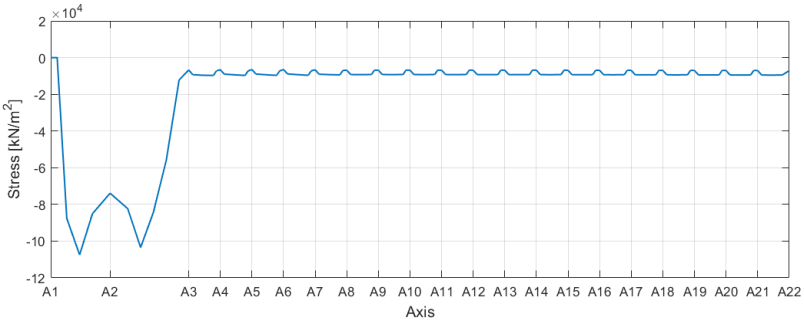

(a) Mean stress due to axial force

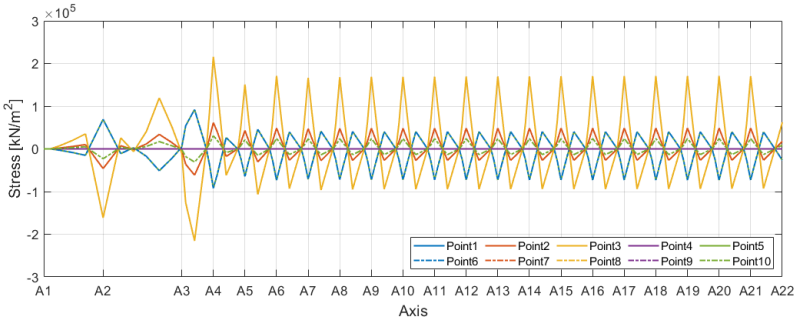

(b) Mean stress due to weak axis bending moment

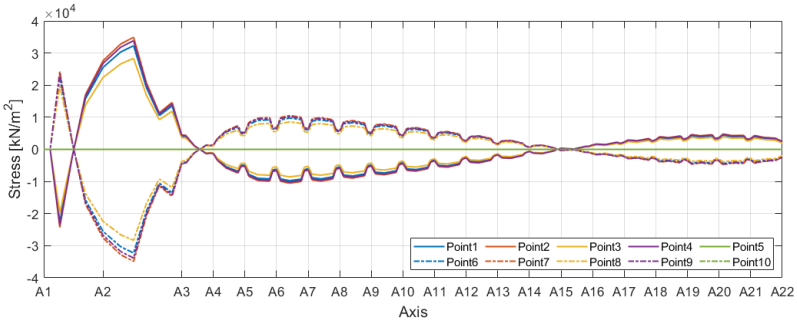

(c) Mean stress due to strong axis bending moment

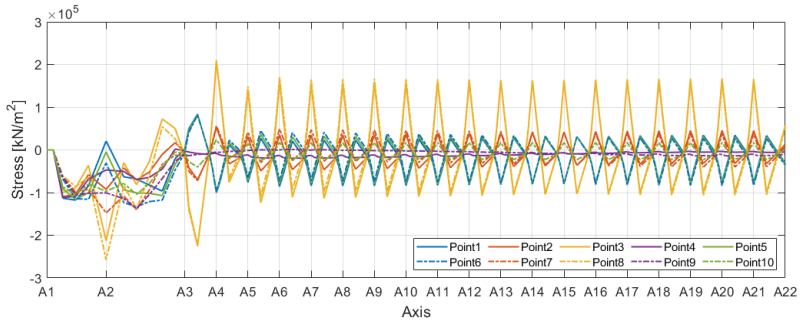

(d) Total mean stress

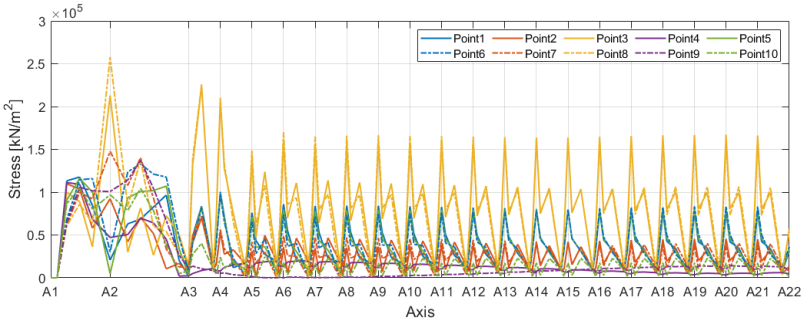

(e) Absolute total mean stress

Figure C.12: The components and total of the bridge girder mean stress at different points under wave 1 with wind condition: (a) Mean stress due to axial force, (b) Mean stress due to weak axis bending moment, (c) Mean stress due to strong axis bending moment, (d) Total mean stress, and (e) Absolute total mean stress.

Mean Stress Contributions at Different Points

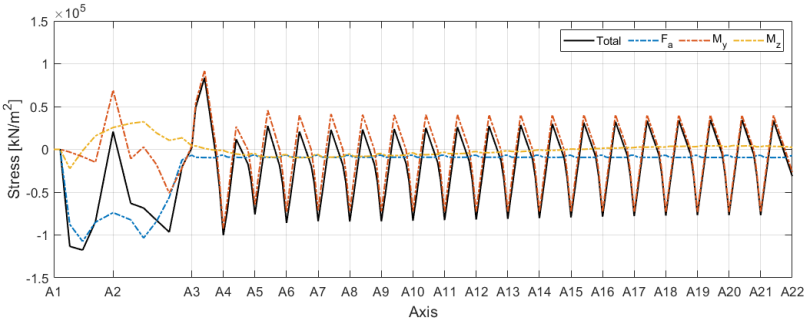

(a) Point 1

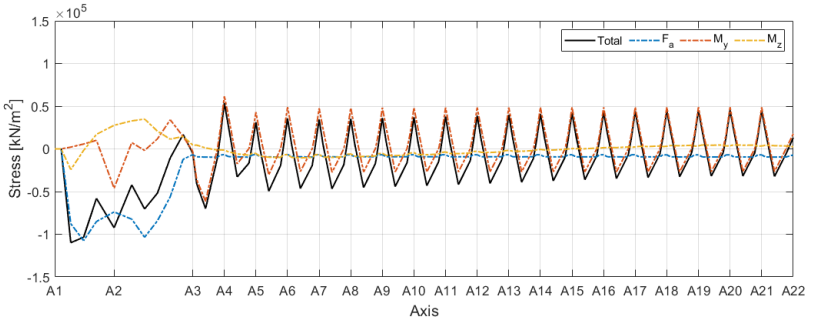

(b) Point 2

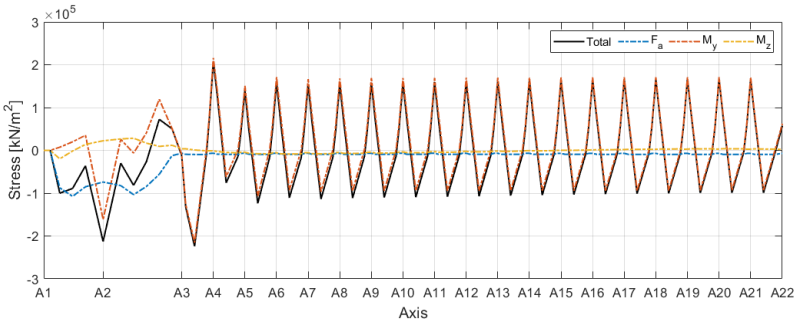

(c) Point 3

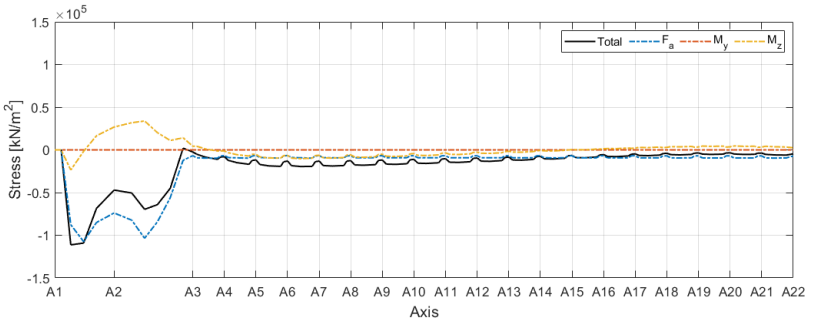

(d) Point 4

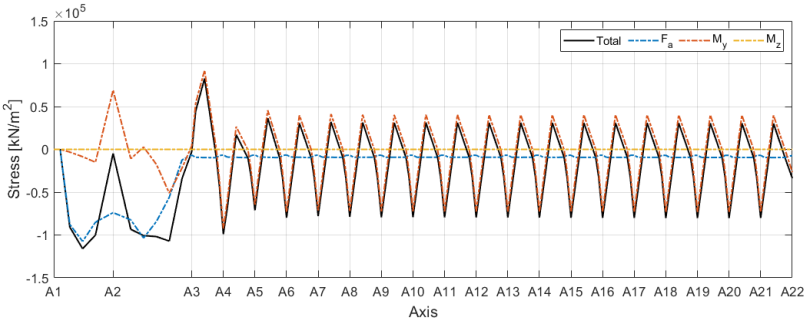

(e) Point 5

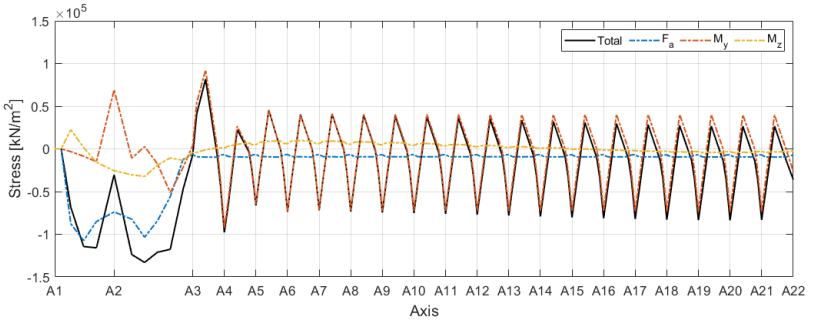

(f) Point 6

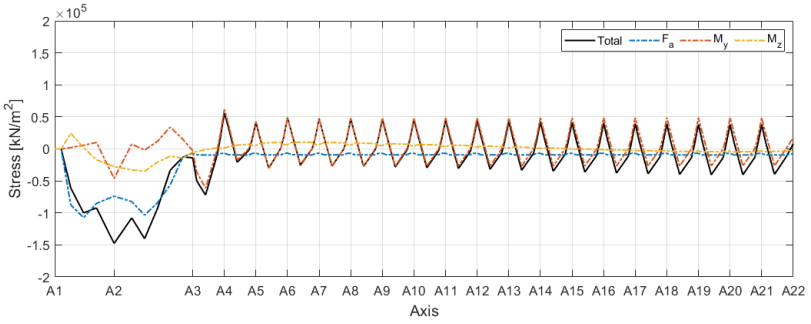

(g) Point 7

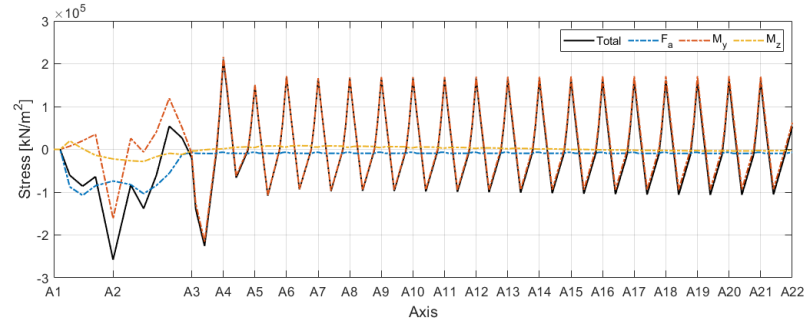

(h) Point 8

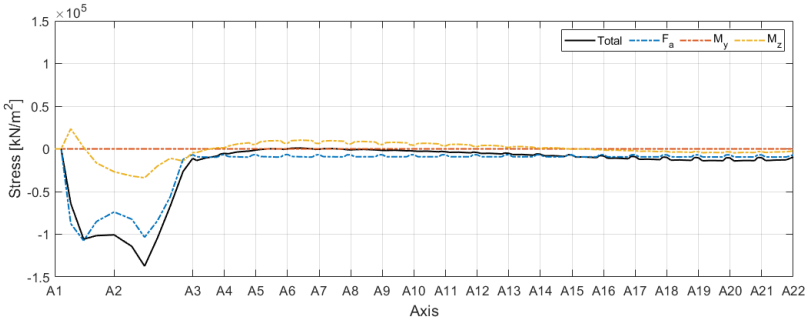

(i) Point 9

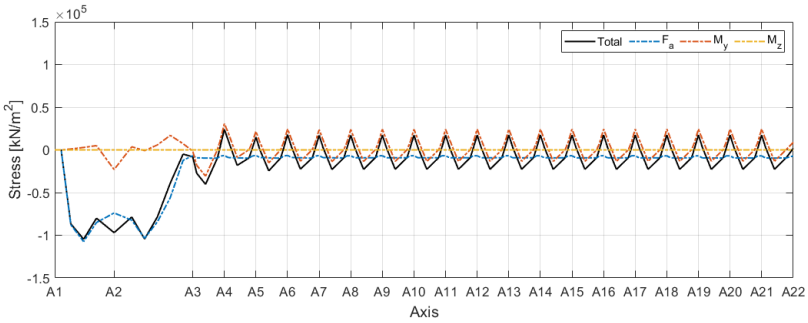

(j) Point 10

Figure C.13: The contributions of the bridge girder mean stress under wave 1 with wind condition at different points: (a) Point 1, (b) Point 2, (c) Point 3, (d) Point 4, (e) Point 5, (f) Point 6, (g) Point 7, (h) Point 8, (i) Point 9, and (j) Point 10.

Standard Deviation

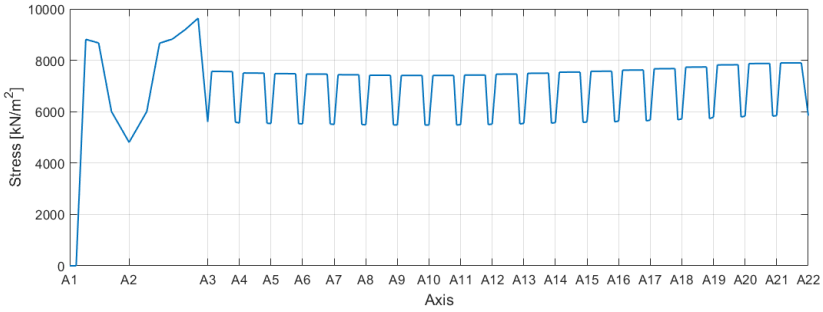

(a) Std of stress due to axial force

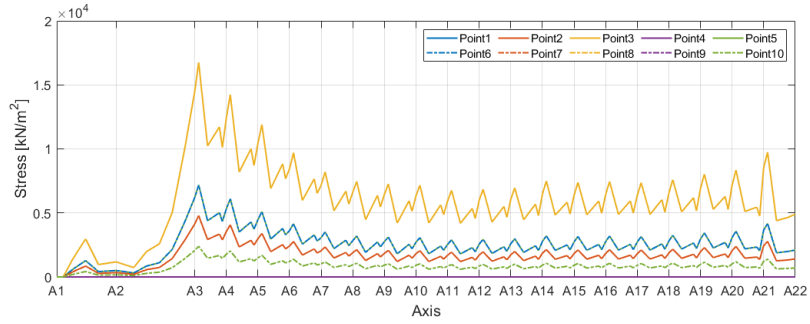

(b) Std of stress due to weak axis bending moment

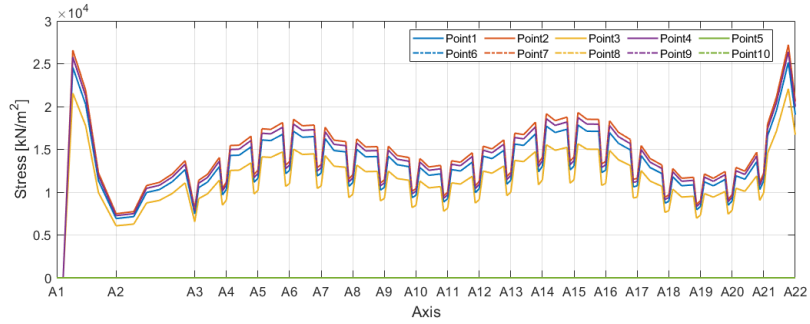

(c) Std of stress due to strong axis bending moment

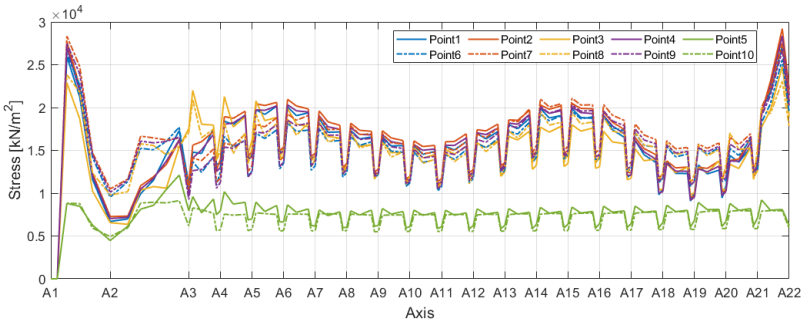

(d) Std of total stress

Figure C.14: The standard deviation of the components and total bridge girder stress at different points under wave 1 with wind condition: (a) Std of stress due to axial force, (b) Std of stress due to weak axis bending moment, (c) Std of stress due to strong axis bending moment, and (d) Std of total stress.

Standard Deviation Contributions at Different Points

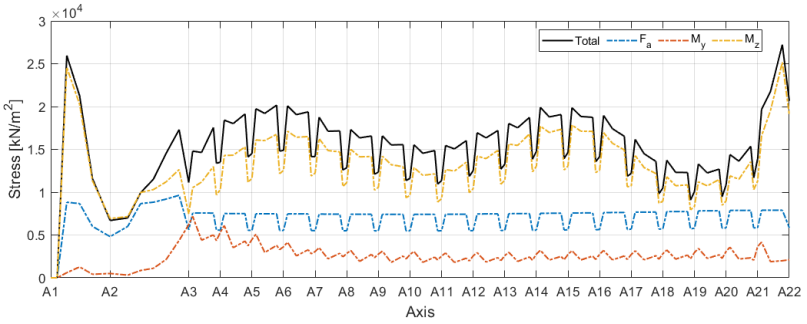

(a) Point 1

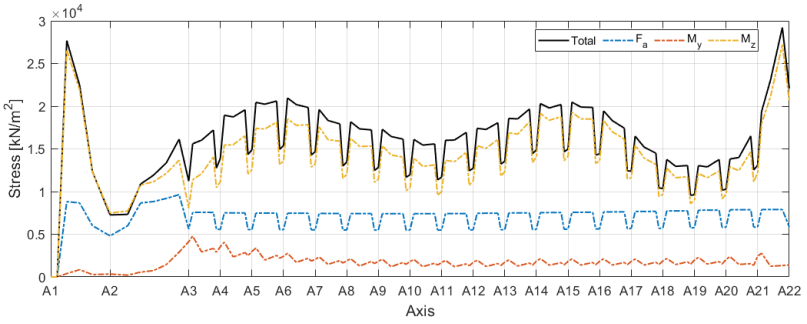

(b) Point 2

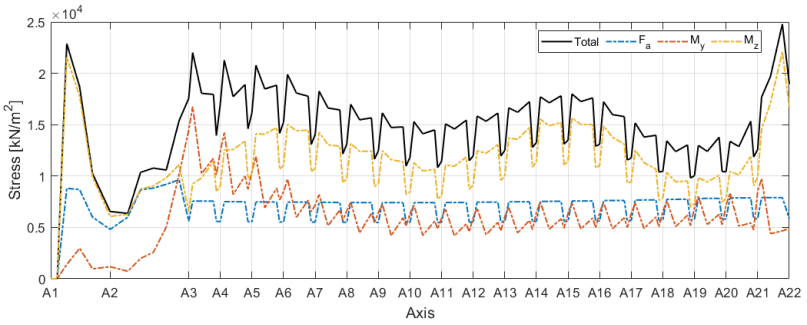

(c) Point 3

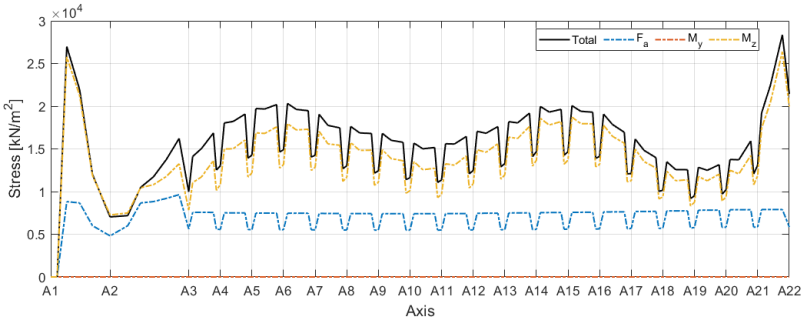

(d) Point 4

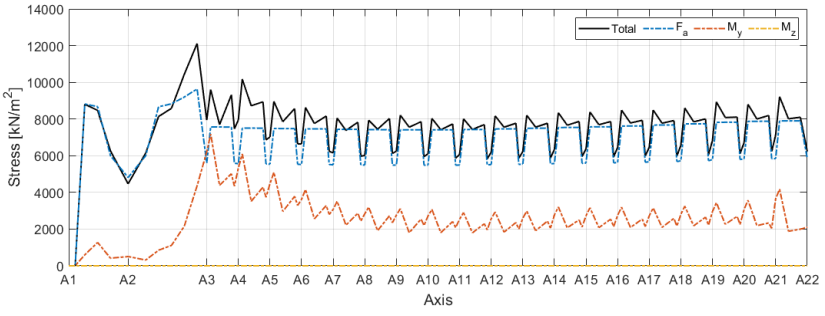

(e) Point 5

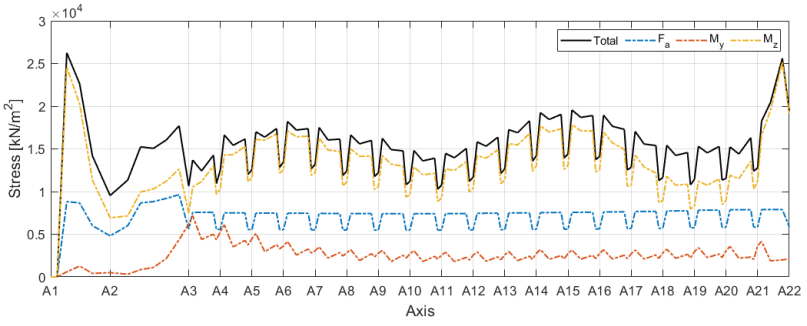

(f) Point 6

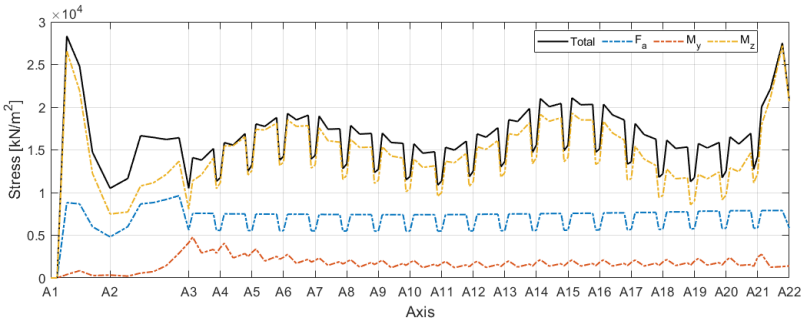

(g) Point 7

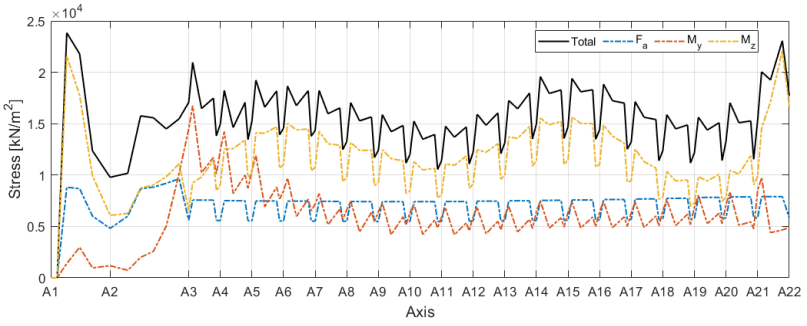

(h) Point 8

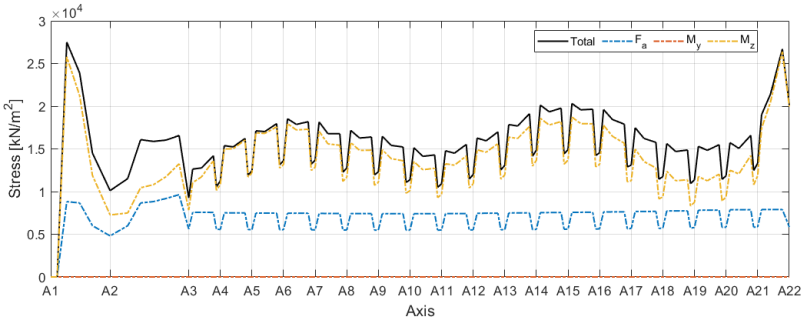

(i) Point 9

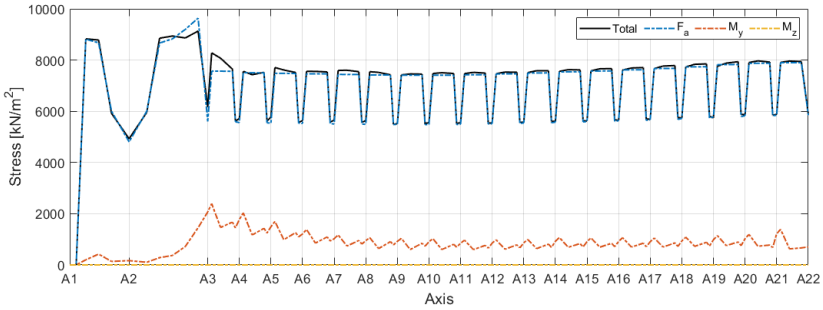

(j) Point 10

Figure C.15: The contributions of the standard deviation of the bridge girder stress under wave 1 with wind condition at different points: (a) Point 1, (b) Point 2, (c) Point 3, (d) Point 4, (e) Point 5, (f) Point 6, (g) Point 7, (h) Point 8, (i) Point 9, and (j) Point 10.

C.4 Comparison of Bridge Girder Statistical Properties

C.4.1 Mean Stress

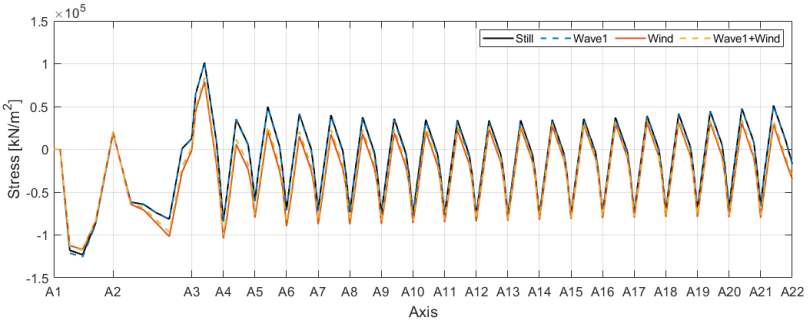

(a) Point 1

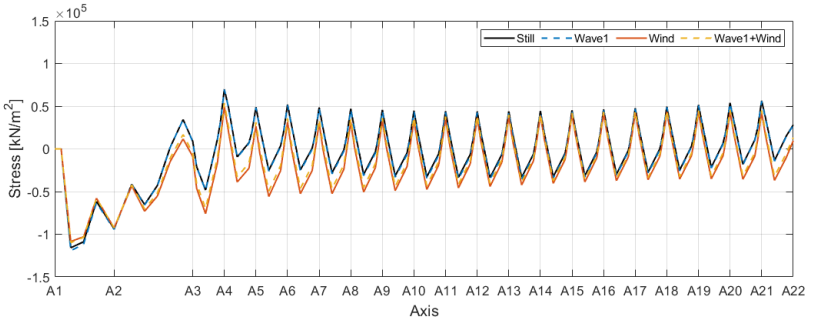

(b) Point 2

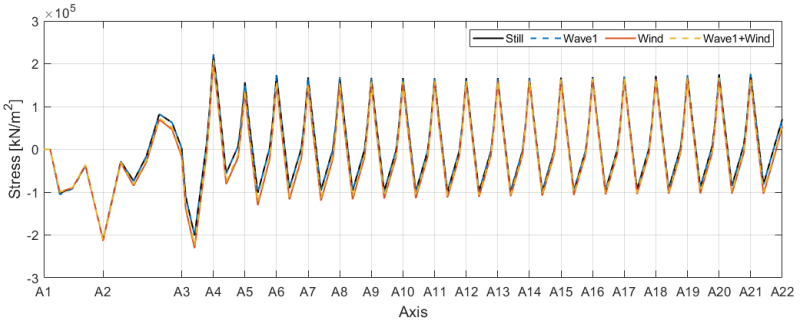

(c) Point 3

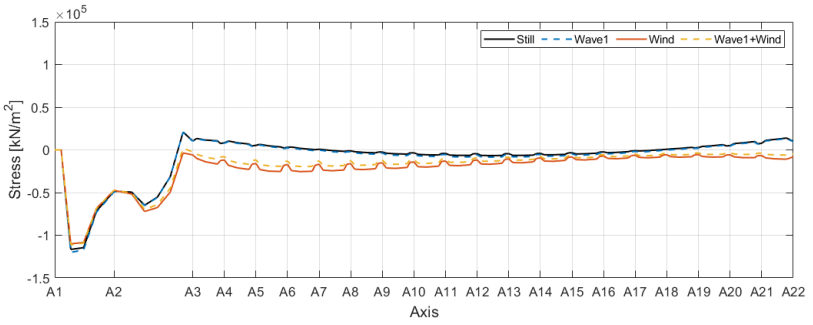

(d) Point 4

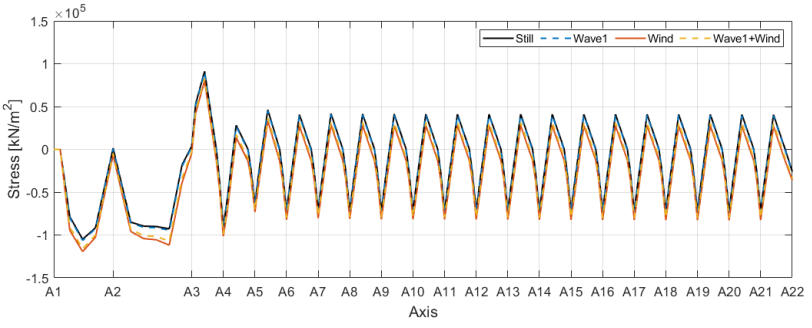

(e) Point 5

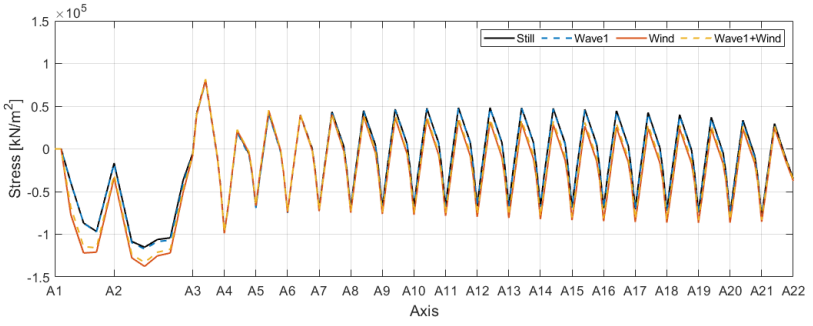

(f) Point 6

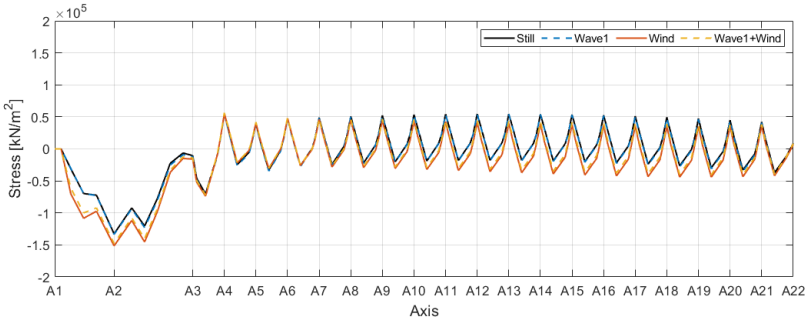

(g) Point 7

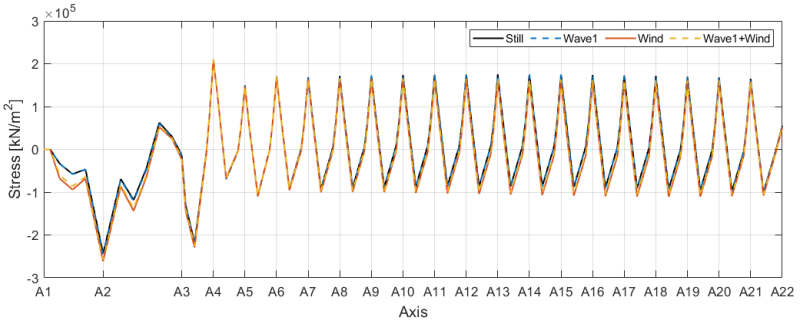

(h) Point 8

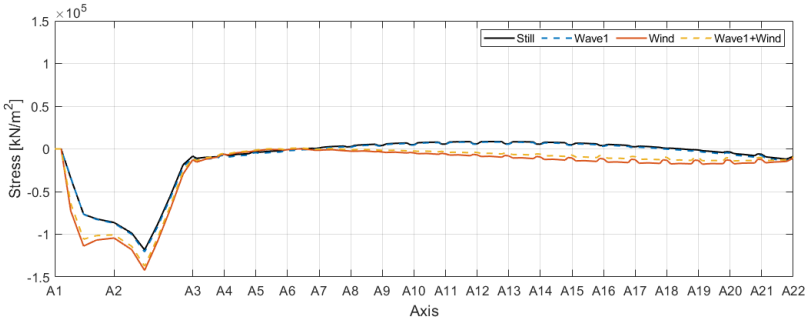

(i) Point 9

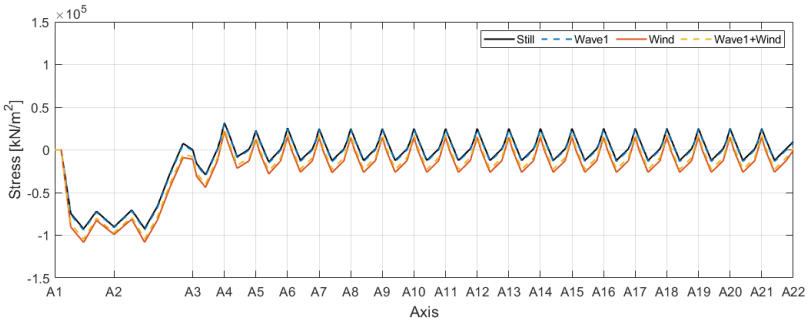

(j) Point 10

Figure C.16: The bridge girder mean stress at different points under the conditions of still water, wave1, wind, and wave1 with wind: (a) Point 1, (b) Point 2, (c) Point 3, (d) Point 4, (e) Point 5, (f) Point 6, (g) Point 7, (h) Point 8, (i) Point 9, and (j) Point 10.

C.4.2 Absolute Mean Stress

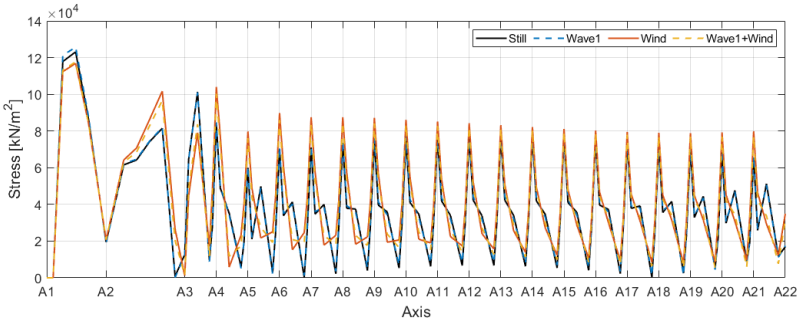

(a) Point 1

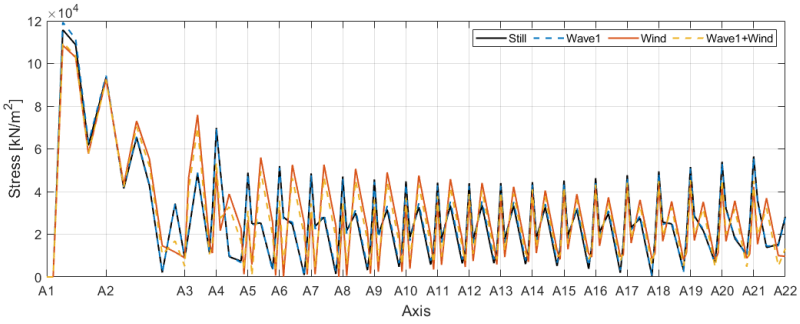

(b) Point 2

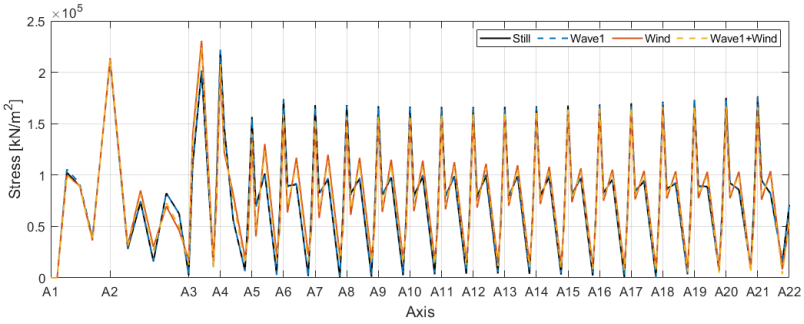

(c) Point 3

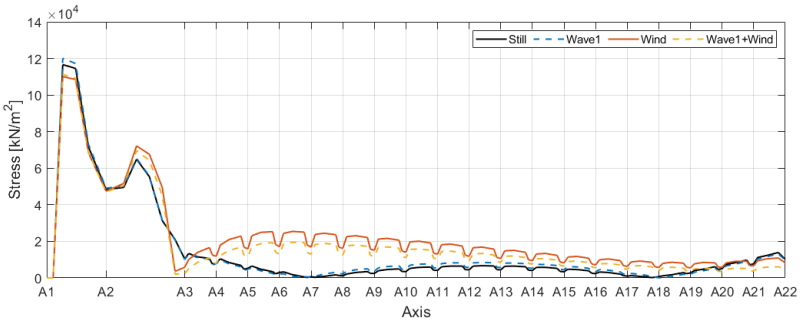

(d) Point 4

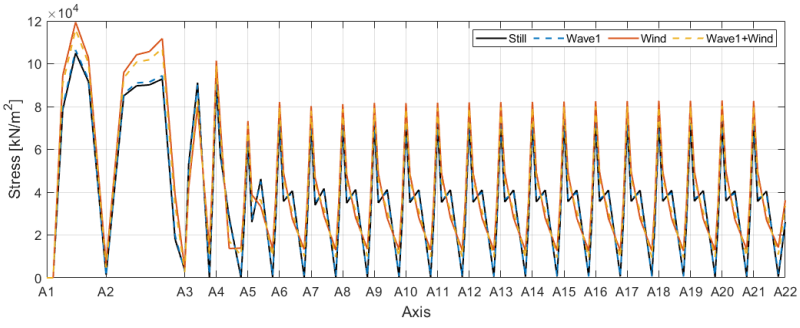

(e) Point 5

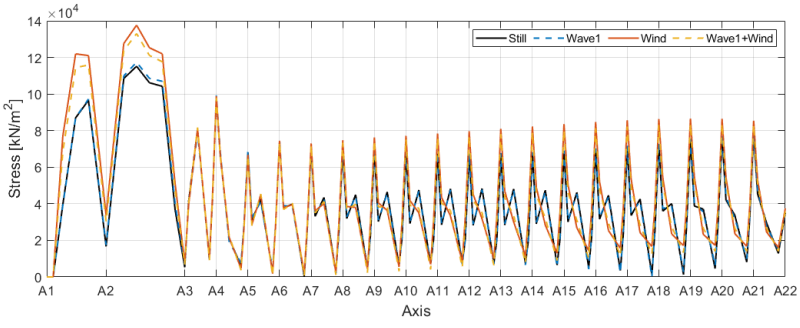

(f) Point 6

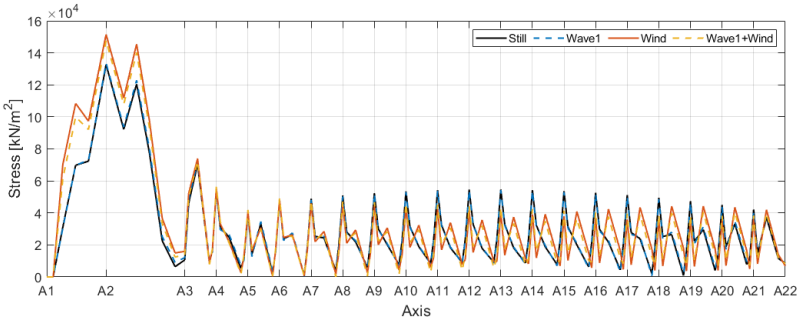

(g) Point 7

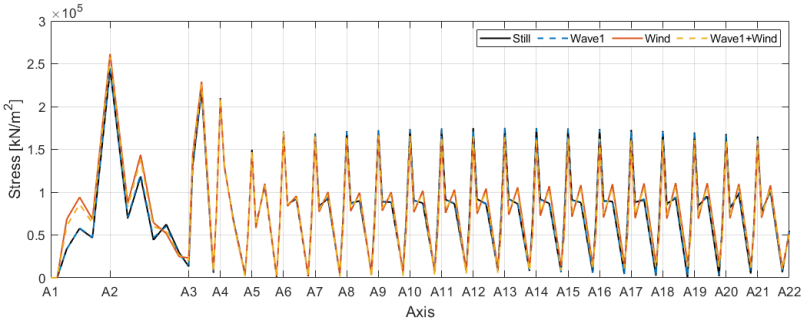

(h) Point 8

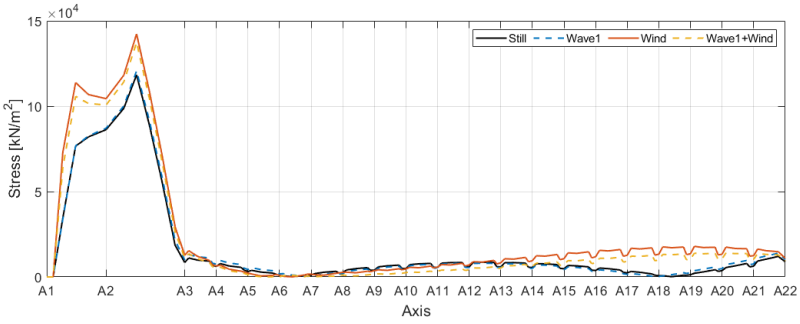

(i) Point 9

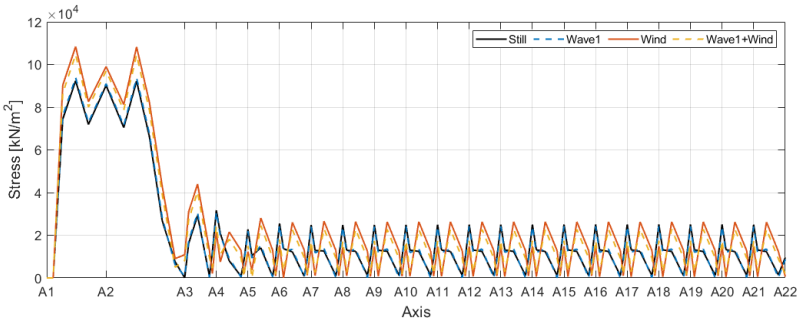

(j) Point 10

Figure C.17: The absolute bridge girder mean stress at different points under the conditions of still water, wave1, wind, and wave1 with wind: (a) Point 1, (b) Point 2, (c) Point 3, (d) Point 4, (e) Point 5, (f) Point 6, (g) Point 7, (h) Point 8, (i) Point 9, and (j) Point 10.

C.4.3 Standard Deviation

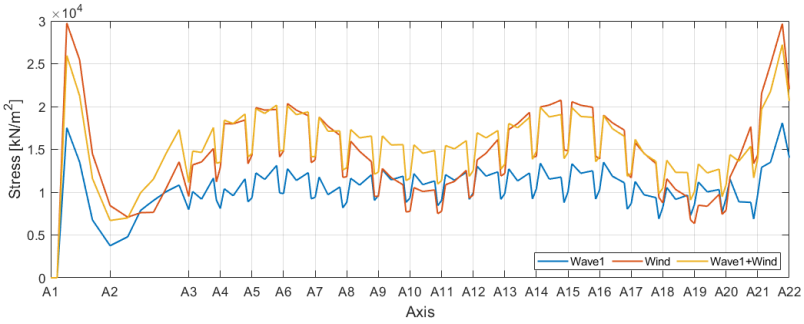

(a) Point 1

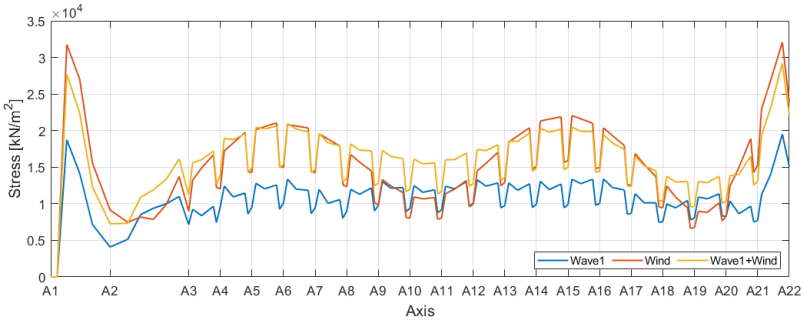

(b) Point 2

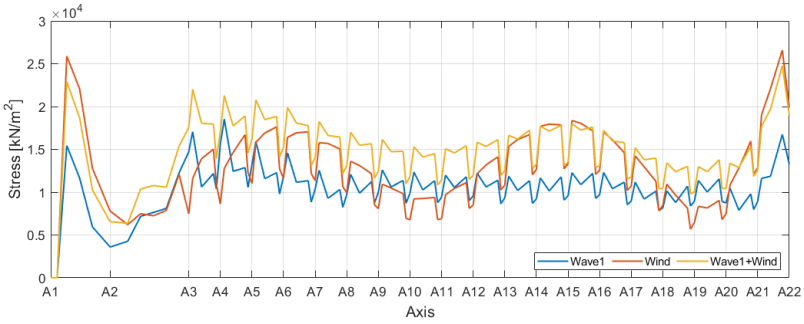

(c) Point 3

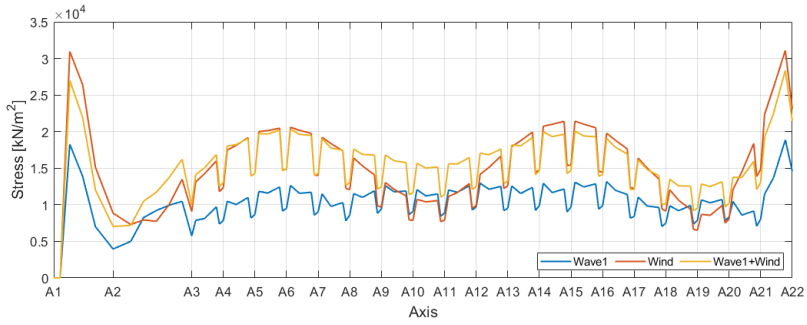

(d) Point 4

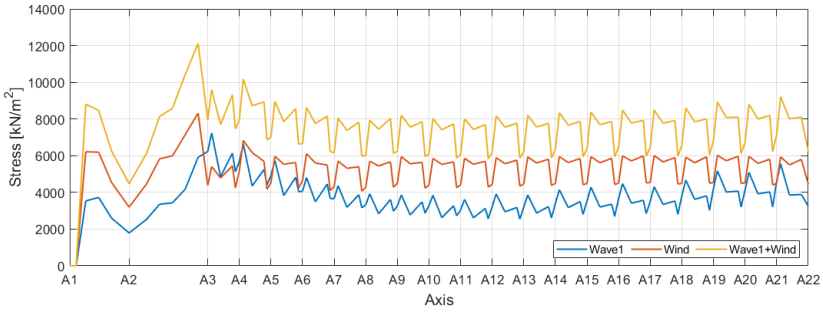

(e) Point 5

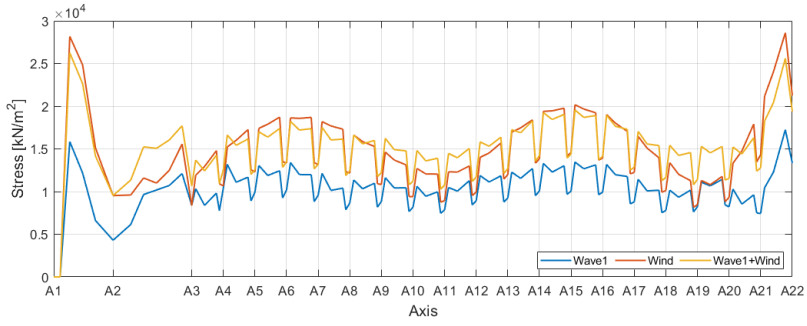

(f) Point 6

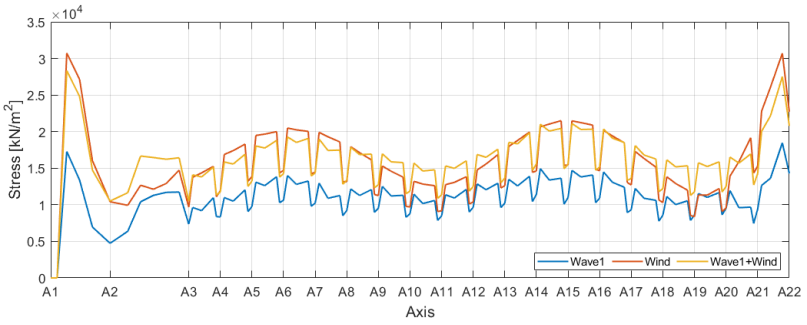

(g) Point 7

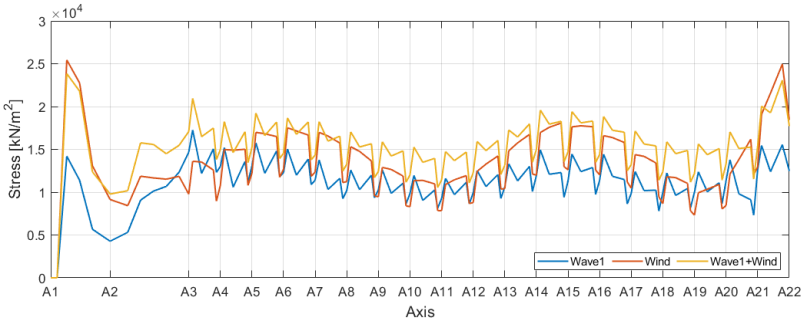

(h) Point 8

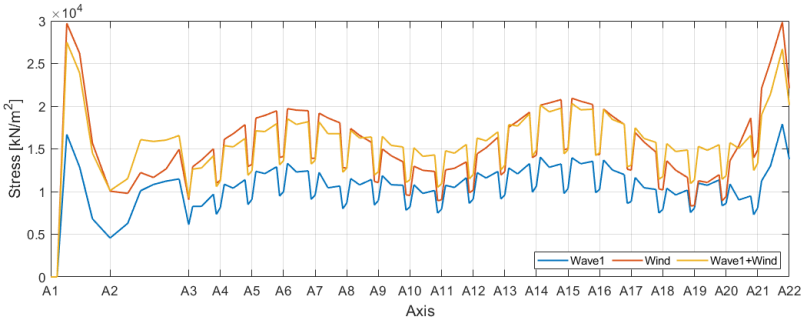

(i) Point 9

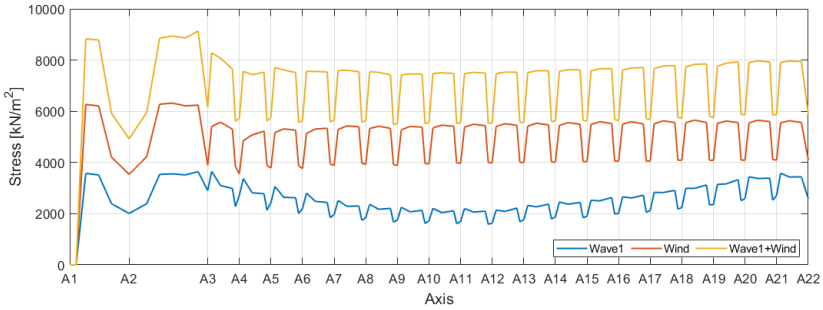

(j) Point 10

Figure C.18: The standard deviation of the bridge girder stress at different points under the conditions of still water, wave1, wind, and wave1 with wind: (a) Point 1, (b) Point 2, (c) Point 3, (d) Point 4, (e) Point 5, (f) Point 6, (g) Point 7, (h) Point 8, (i) Point 9, and (j) Point 10.

Sunghun Hong

Master's thesis

NTNU
Norwegian University of
Science and Technology

DTU